Engineering Ceramics and Thermal Stresses

Erik Teeuw

RIJKSUNIVERSITEIT GRONINGEN

ENGINEERING CERAMICS AND THERMAL STRESSES

Proefschrift

ter verkrijging van het doctoraat in de
Wiskunde en Natuurwetenschappen
aan de Rijksuniversiteit Groningen
op gezag van de
Rector Magnificus, dr. F. van der Woude,
in het openbaar te verdedigen op
maandag 22 december 1997
des namiddags te 2.45 uur

door

Dirk Herbert Johan Teeuw

geboren op 26 maart 1968
te Roden

Promotor: Prof.dr. J.Th.M. De Hosson

ISBN: 90 367 0829 x

The work described in this thesis has been made possible by financial support from Hoogovens Groep B.V., IJmuiden.

1 INTRODUCTION

Ceramic materials are widely used for their superb performance in applications where other types of material may fail. Possible applications are circumstances where materials have to withstand high temperatures, corroding environments and severe wear. However, metals instead of ceramics may possess mechanical properties, which better meet demands upon mechanical loading. In our current research programme, a substantial amount of effort is put in the development and design of combining specific properties of metals and ceramics [1]. Complementary, the processing of ceramic materials, bulk material as well as thin layers, is studied. The focal point of interest in the research on the ceramic materials is on the evolution of residual stresses and the morphology of these materials.

This thesis deals with fundamental problems that may arise in the production process of ceramic materials. The classical procedure of processing ceramics exists of moulding the ceramic powder into the form desired. Subsequently, the powder compact is densified in a firing process to end products that exhibit low porosity [2]. This procedure yields ceramic products with high mechanical strengths in compression. However, the tensile strength is typically much lower due to the fact that the fracture stress in tension of ceramic materials lies below the stress level to produce dislocations, i.e. below the level where considerable plastic deformation occurs [3].

The tensile strength may be increased by, e.g. the addition of a second phase, or by making a layered compound [4,5]. Cracks propagating through the material will branch or deflect in either system which lead to larger values for the critical stress intensity factor, the factor governing the fracture strength of a material.

Inhomogeneties present in the powder compact lead to deviations of local densification rates of the material during the firing process [6]. Furthermore, the presence of dissimilar materials will lead to differences in expansion and shrinkage upon heating or cooling of the material. Both effects may be a source for internal stresses in the material that may persist after the

production process of the ceramic materials and they may alter the mechanical performance of the ceramic product in a negative sense.

This thesis primary aims at studying the residual stress states which evolved during the production stages of ceramic products. Several techniques will be explored to investigate the stresses present in the products. In chapter 2 the production process of the ceramic materials is briefly discussed. The powder compacts as well as nanostructured thin ceramic layers are treated [7]. In addition, some basic techniques are discussed. The method to derive information on the residual stress state present in the specimen, namely x-ray residual stress measurements, is discussed in more detail.

The evolution of residual stresses in the composite ceramic materials is studied in chapter 3. The influence of a second phase, -zirconia-, on a ceramic matrix, -alumina-, is discussed. The addition of a second phase will result in material properties which are dissimilar from the properties of a heterogeneous matrix. Analytical as well as finite element calculations are applied to calculate the residual stress state throughout the ceramic product.

Morphologies of the materials are studied using a dedicated low voltage scanning electron microscopy. The advantage of this low voltage microscope over conventional microscopes is that non-conducting specimen may be studied directly, since charging effects are suppressed by balancing the amount of inserted and emitted electrons at low accelerating voltages. Features in the densification process of the two-phase ceramic materials which manifest in the production process are studied using SEM techniques in chapter 4. Changes in morphology in the nanostructured ceramic films during the processing of these films are studied as well.

Chapter 5 evaluates the residual stresses in the composite ceramic materials. Precise determination of residual stresses using x-ray stress analysis require accurate information of material properties, like the Young's modulus and Poisson's ratio. Since these constants are unknown for the two-phase materials, a method is devised to measure them experimentally. They are measured in situ using a specifically designed device for the determination of material constants of brittle materials, like ceramics. With these material constants, the residual stress state of the ceramic products are determined experimentally. The nanoceramic layers, being cured by various heat treatments, are investigated using x-ray analysis. Changes in microstructure as well as the evolution of residual stresses in the layers will be studied.

Since scanning electron microscopy proved that the processing conditions of the thin ceramic layers affect the eventual quality of the layers to a large extent, the mechanical behaviour of the layers are studied quantitatively in chapter 6. A model is proposed that describes the thickness of the layer in terms of a crack driving force for the nanostructured ceramics. With the model it is possible to predict a critical thickness for the ceramic layers, based on the elastic properties of the layer and the substrate.

References

1 J.Th.M. De Hosson, W.P Vellinga, X.B. Zhou and V. Vitek, Stability of Materials, Plenum Press, New York, (1996), 581-614.

2 E. Dörre and H. Hübner, Alumina, Springer-Verlag, Berlin, (1984), 52.

3 Anon., Engineered Materials Handbook, vol. 4; Ceramics and Glasses, ASM international, (1991), 585.

4 Y. Matsumoto, K. Hirota and O. Yamaguchi, J. Am. Ceram. Soc., **76**, (1993), 2677.

5 T. Chartier, D. Merle and J.L Besson, J. Eur. Ceram. Soc., **15**, (1995), 101.

6 R.M. German, Acta. Metall. Mater., **40**, (1992), 2085.

7 C.J. Brinker and G.W. Scherrer, Sol-Gel Science, Academic Press, San Diego, (1990).

2 BASIC CONCEPTS

Introduction

Mechanical behaviour and material properties of engineering ceramic materials are affected by the morphologies, microstructures and the state of the residual stress. To understand the properties of these materials, several tools are used in this thesis to study these aspects. In this chapter, processes of forming, consolidating and densifying the materials will be discussed. Further, the various experimental methods which are used to study the materials, together with their theoretical backgrounds will be considered. This provides a way to evaluate their advantages and to determine the experimental constraints.

2.1 Composite ceramics

The manufacturing process of bulk ceramic products starts with precursor powders. These powders may exist of agglomerates of grains which are shaped and compacted into the form desired. In a firing process, during which the green products are subjected to elevated temperatures, i.e. at about 67% of the melting temperature of the material, the compacted powders are densified and toughened. During the firing process, bonds are formed between mutual particles. Because of the reduction in pore volume between the particles, global shrinkage of the specimen will occur.

The material of interest in this thesis is a composite ceramic. This class of ceramic materials consists of a ceramic matrix, in which a second phase is dispersed. The system of interest here is an alumina (Al_2O_3) matrix in which a second phase zirconia (ZrO_2) is present. The presence of ZrO_2 in the matrix may influence the material properties of the alumina matrix, e.g. the toughness of the alumina matrix increases and an increase in wear resistance is observed [1].

The addition of a second phase may have several impacts on the densification behaviour of the green product during the sintering process. The second phase may influence the densification of the matrix in a positive or in a negative sense. Furthermore, a second phase is known to control the grain growth of matrix particles again both in a positive or in a negative manner [2-4].

The second phase is added in the early stage of agglomerate formation. The starting powders of both matrix and second phase are mixed. From this mix, together with a binder, a slurry is made, that is further mixed in a ball milling device. After milling for a distinct time, the slurry is dried using a rotavapor technique. In order to eliminate very large agglomerates, the powder is sieved. To further dry the powder, a hot air furnace is used. A micrograph of the resulting two-phase powder is displayed in figure 2.1.

In the micrograph, the homogeneous mixing of both powders is evident. From the powder the products are formed using a uniaxially pressing device. This results in circular pellets. The specimens have an aspect ratio, that is the ratio of the diameter to the height, of ~8. This aspect ratio is of course a function of the amount of powder pressed in the device, having specific dimensions. During the compaction step, the green products are densified to ~65-70% of their theoretical density. The theoretical density is the density of a product with zero pore volume.

Further densification takes place in a furnace. The green products are subjected to ~67% of their melt temperature. The temperature is raised from room temperature to the sintering temperature using a low heating rate. This

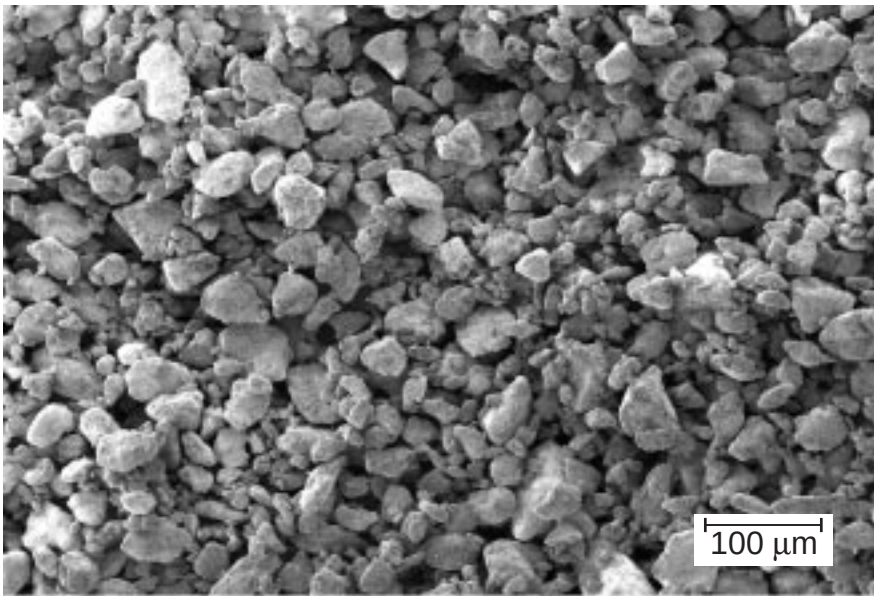

figure 2.1: *Scanning electron microscope micrograph of the two-phase precursor. The average particle size as determined from the micrograph is ~10µm.*

low heating rate is used in order to prevent temperature gradients in the specimen due to the finite thermal conduction coefficients of the specimen. At the sintering temperature, the temperature is kept constant for a given period of time. During this period, all kinds of diffusion processes take place, by which densification occurs. After the sintering process, the specimen is cooled down, again using a small temperature gradient.

In fact, the two-layer ceramic materials, as schematically depicted in figure 2.2, can be produced following two alternative routes. The first method is to compact and pre-sinter the separate layers. In the pre-sintering process, only a limited amount of densification is achieved. Subsequently, the layers are placed on top of each other, and sintered to full density. Bonding of the separate layers over the interface is achieved by diffusion processes between the layers.

An alternative route to achieve two-layer ceramic materials exists of processing the layers simultaneously. The lower layer is formed by compacting the powder in a uniaxially pressing device. Subsequently, the upper layer powder is placed on top of the compacted lower layer and both layers are pressed simultaneously. The green product formed is then sintered to full density in the firing process. Forming two-layer ceramic using simultaneous processing is however limited to products of relatively small dimensions. Increasing the radial size of the specimen will result in increased stress values over the interface, due to differences in shrinkage in both layers.

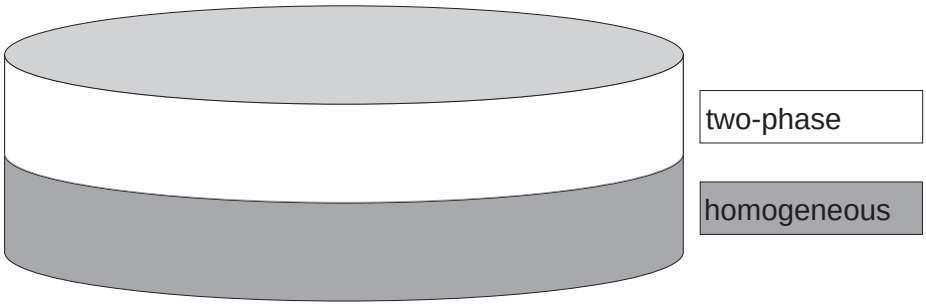

figure 2.2: *Schematic picture of a pellet. The top layer consists of the two phase material as derived from the precursor depicted in figure 2.1. The lower layer is made from the homogeneous α-alumina material.*

2.2 Sol-gel processing

2.2.1 Chemistry of sol-gel processing

Sol-gel processing may be defined as the preparation of ceramic materials by preparation of a sol, gelation of the sol, and removal of the solvent [5]. Here, the sols are produced starting from alkoxides as the precursor. A sol is a colloid of solid particles in a liquid. Colloids are very small (~1-1000 nm) particles, experiencing no other forces than Van der Waals attraction and surface charges forces. Clustering of individual colloids is called aggregation. A gel is an interconnected rigid network with pores of nanometer dimensions and polymeric chains whose average length is greater than a micrometer. At the time of gelation, the structure of the gel is established and can adopt several forms, like well-ordered lamellar structures, as is the case for silica gels, or a disordered polymer network, like the gelation of organometallic precursors.

To derive a sol from a precursor, the precursor is hydrolysed. This will result in the formation of a monomer. As an example, the hydrolysis of tetraethylorthosilicate is given

$$Si(OC_2H_5)_4 + 4\ H_2O \rightarrow Si(OH)_4 + 4\ C_2H_5OH$$

The -OH groups form the reactive species. In the next step, the monomer is condensed by reacting with other monomers.

$$2\ Si(OH)_4 \rightarrow (OH)_3Si - O - Si(OH)_3 + H_2O$$

The silica network evolves from the polymerisation of the $Si(OH)_4$ monomers. When sufficient Si - O - Si bonds are formed, they respond collectively as colloidal particles, i.e. a gel is formed. Both hydrolysis and condensation reactions are pH-controlled, as schematically depicted in figure 2.3. At low pH-values the condensation reactions are slow compared to the hydrolysis reactions, whereas at *pH*>5 the condensation reactions are dominant.

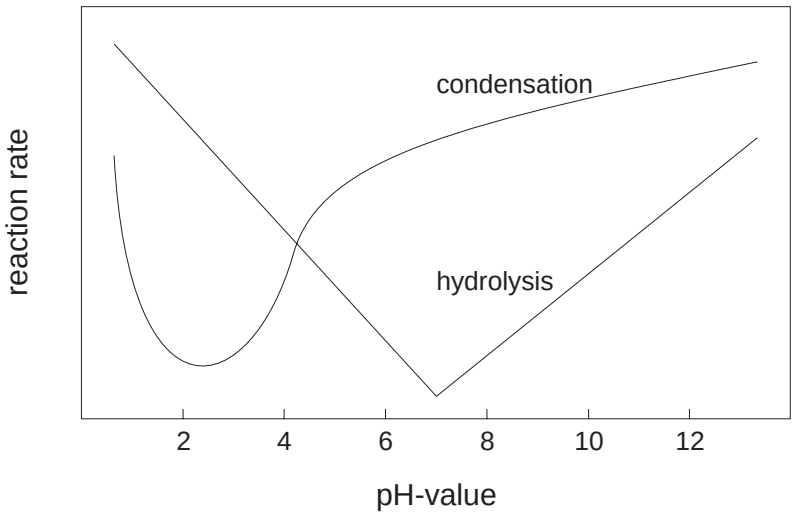

figure 2.3: *The reaction rate for the hydrolysis and condensation reactions in the sol-gel process as a function of the pH-value of the solution. At low pH-values the condensation reactions are slow, whereas at intermediate pH-values, pH>5, the condensation reactions are predominant. Upon spinning the layers, condensation is promoted by an increase of the concentration of hydrolyzed species by means of evaporation of the solvent.*

2.2.2 Processing of sol-gel layers

The coatings are deposited on the substrate, which may exist for example of monocrystalline silicon, polycrystalline alumina or quartz. Deposition may take place by means of spin or dip coating [6]. In the latter, the substrate is immersed in the liquid as depicted in figure 2.4.*a*. After immersion, the coated specimen is taken out of the fluid and, due to the evaporation of volatiles, gelation starts in the coating. Dip coating is especially of interest when a continuous coating process is required.

Spin coating is a batch process, schematically depicted in figure 2.4.*b*. Since all coatings studied in this thesis are produced using the spin coating technique, this process will be discussed in more detail. Spin coating is a technique where in the first stage of the process, an excess of liquid is dispensed on the substrate.

The next stage is the spin-up stage, in which the centrifugal force drives the liquid radially outward. During the formation of the layer, condensation is stimulated by an increase of the concentration of hydrolysed species by means of evaporation of the solvent. The final thickness of the film is

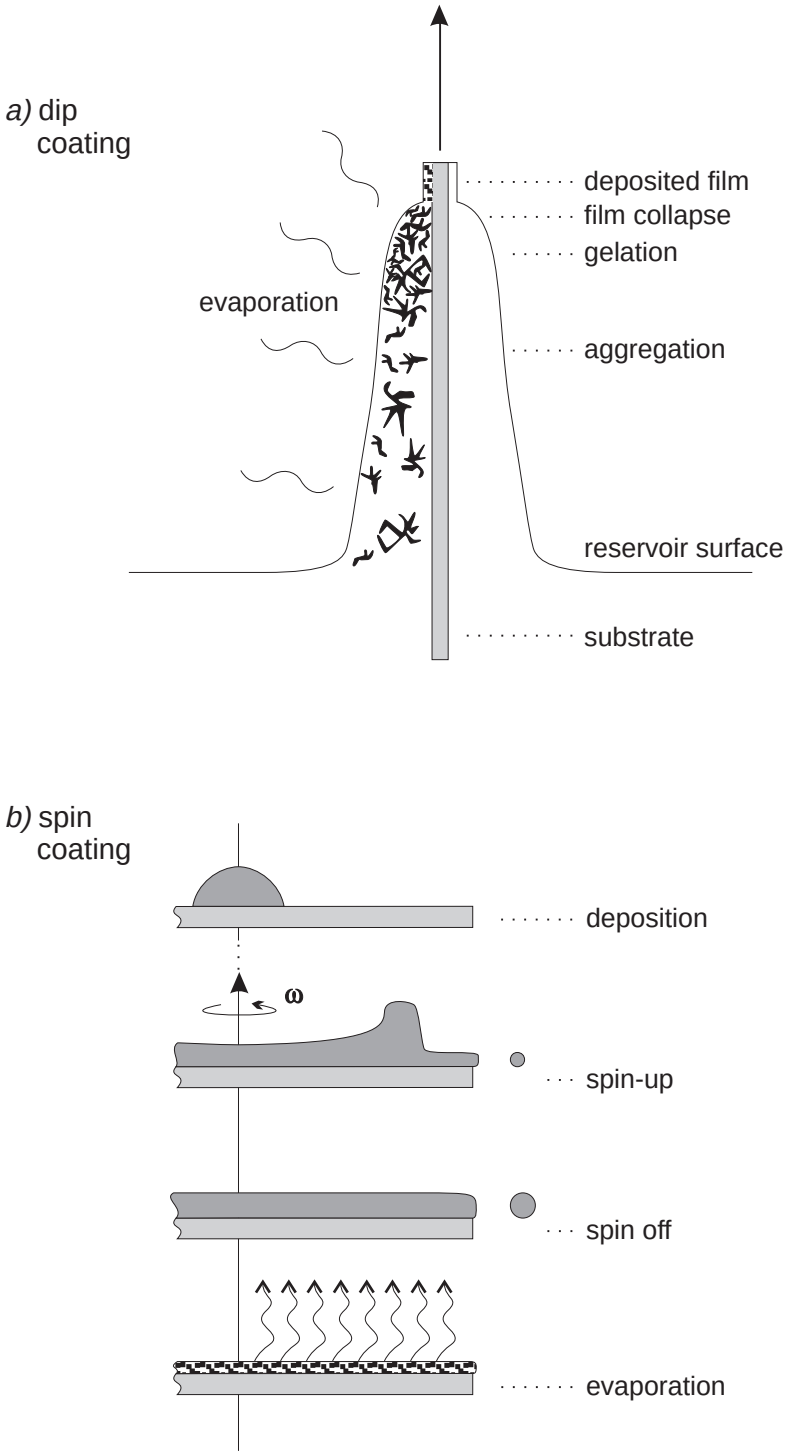

figure 2.4: *Various stages in the deposition of the thin ceramic layers for the different deposition techniques.*
a) Dip coating process.
b) Spin coating process.

controlled by flow processes in the final stage, the spin-off stage. The flow of the liquid is governed by two processes: the centrifugal force that drives the liquid outward and the viscous force acting radially inward. Balancing these forces results in [7]

$$h(t) = \frac{h_0}{\left(1 + \frac{4\rho\omega^2 h_0^2 t}{3\eta}\right)^{\frac{1}{2}}} \tag{2.1}$$

with $h(t)$ the time dependent film thickness, ω the angular velocity during spinning, ρ the density of the liquid, η the viscosity of the liquid and h_0 the initial thickness of the film. The thickness of the films is governed by evaporation processes. Non-volatiles can only leave by flow and when this becomes impossible, they constitute the final film after the volatiles have evaporated. This means that at high spin speeds the initial thickness h_0 is irrelevant for the final thickness h_f . On the other hand, for low h_0 and at low spin speed, evaporation is the only thinning mechanism.

After spinning and evaporation, the layers are densified in a furnace or laser treatment. During furnace densification, the sample is placed in a furnace and cured in air at temperature T for a time t. For laser curing, the power density P and interaction time τ are determined by [8]

$$P = \frac{I}{\pi\left(\frac{x}{2}\right)^2} \qquad \tau = \frac{x}{v} \tag{2.2}$$

Here x is the diameter, I the intensity of the laser beam and v its scanning velocity.

The densification of sol-gel layers takes place by mass transport from particles to the interconnecting points between these particles, hereby reducing total porosity. The mass transport may take place through diffusion processes or viscous flow. The driving force results from minimisation of the surface energy. Three stages can be distinguished in the densification process.

In figure 2.5 the mechanisms contributing to densification are displayed as well as changes in morphology at various stages. The first stage is neck

formation between attracting particles. The dominant transport mechanisms are surface and lattice diffusion and vapour transport, all of which are transporting mass from the surface of the particles to the interconnecting neck.

In the intermediate stage a grain boundary is formed between crystalline particles. With the grain boundary, a grain boundary energy γ_{gb} is associated, determining the shape of the pores. Mass transport takes place by lattice and boundary diffusion, transporting mass from the grain boundary to the interconnecting neck. In this stage pronounced densification is observed, due to material removal between particle centers, causing the distance between centers to decrease.

In the final stage the remaining pores are no longer interconnected. Densification is very slow, hence theoretical densities will not be reached.

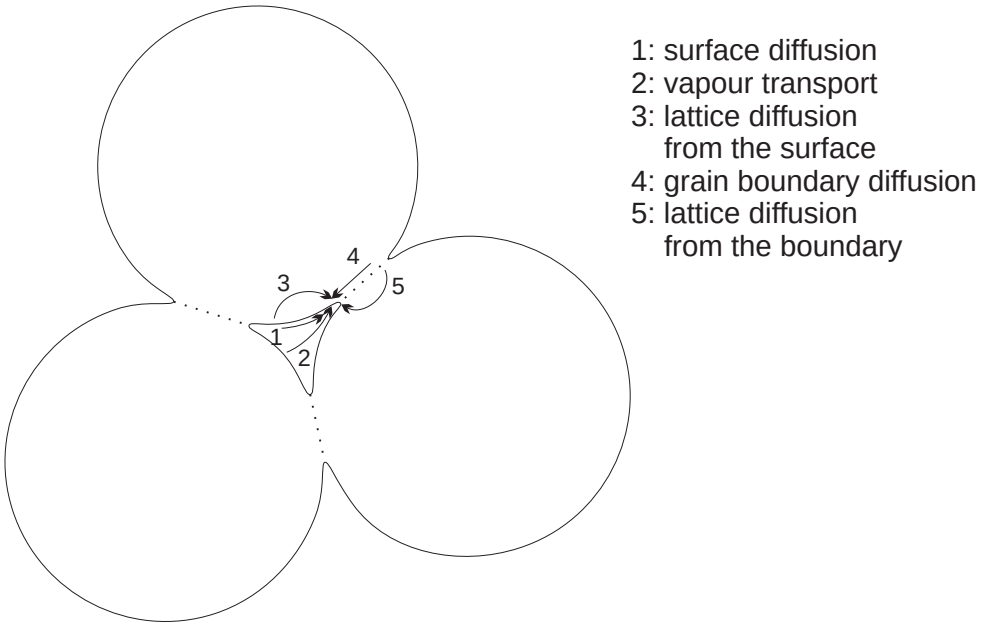

figure 2.5: *Densification mechanisms in the sinter process. From the listed mechanisms, only lattice and grain boundary diffusion bring about densification.*

2.3 Low-voltage scanning electron microscopy

In a scanning electron microscope, high energy electrons are used as the imaging medium. The wavelength of the electrons, the so-called De Broglie wavelength, depends upon their accelerating voltage

$$\lambda = \frac{12.3}{\sqrt{E_{eV}}} \cdot 10^{-10} \qquad (2.3)$$

with E_{eV} the energy of the electrons in electronvolts depending on the accelerating voltage. This wavelength is significantly smaller than the wavelength of visible light. Therefore, the resolving power of a scanning electron microscope can be much larger than that of a light microscope.

In figure 2.6, the set-up of a scanning electron microscope is schematically depicted. Electrons can be produced via a heated hairpin filament or a heated LaB_6 crystal. The electrons generated by the LaB_6 crystal have energies in a narrower window, causing less focusing errors due to chromatic aberrations. The more recently commercially available scanning electron microscopes are equipped with a field emission gun (FEG). The FEG sources generally make use of a single crystal of tungsten. Electrons are extracted from the source by

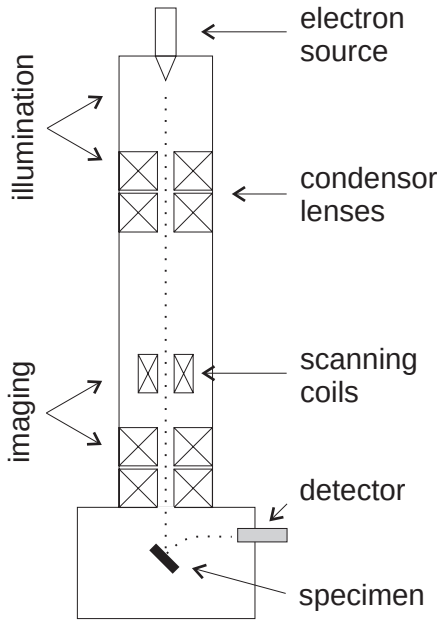

figure 2.6: *Principal elements of a scanning electron microscope.*

a very high electrostatic field (in the order of 10^{10} V/m) at the surface, enabling the electrons to tunnel through the potential barrier. The high brightness and spatial coherence make these sources excellent for use in high resolution scanning electron microscopes.

The electron beam is focused by a system of magnetic lenses to a small spot of around 1-10 nm in diameter. The beam scans the surface by means of deflecting coils. As the primary electrons enter the surface, several processes are initiated. The processes which are important for the imaging part of a scanning electron microscope are depicted in figure 2.7.

If the energy of the primary electrons is high enough, they produce electrons, excited from the conduction band, which can escape from the surface. These electrons, also called secondary electrons, are low energy electrons. Due to the low energy, they have short mean free paths, of the order of nanometers. Therefore, only secondary electrons coming from the point of incidence of the primary beam can be detected by the detector, making these secondary electrons of importance for topographical studies. The lateral resolution, using secondary electrons, of the scanning electron microscope is of the order of nanometers.

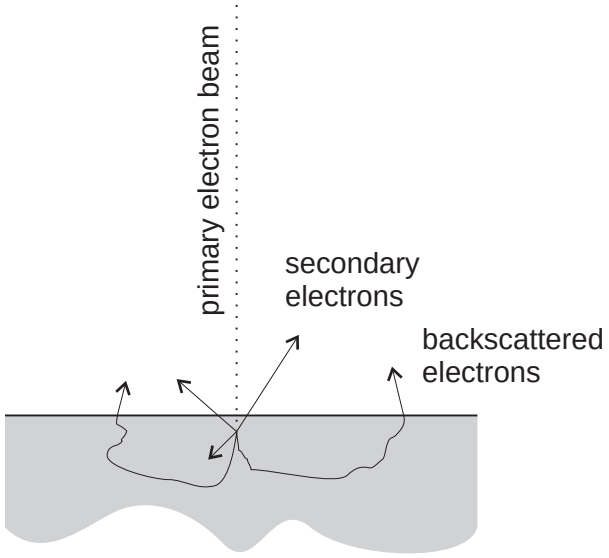

figure 2.7: *Interaction of the primary electron beam with the specimen under investigation. Two of the processes taking place are highlighted, namely the generation of secondary electrons and the backscattering of primary electrons.*

Primary electrons which enter the specimen are scattered elastically or inelastically by the atoms near the surface layer. This can cause primary electrons to exit the specimen, i.e. backscattering, after travelling through the specimen. Since the material volume in which the electrons are backscattered, can be much larger than for the secondary electrons, the lateral resolution is much smaller. Operating the microscope in the backscattered mode results in a lateral resolution of the order of micrometers.

The primary electrons current is approximately 10^{-8} to 10^{-7}A. The penetration depth of the high energy electrons will cause the electrons to be trapped in the material. When studying conducting materials, the electrons will be transported away from the point of incidence. If the specimen is a non-conducting material, the excess electrons will cause charging of the surface. The electrostatic charge on the surface deflects the incoming electrons, giving rise to distortion of the image. In order to reduce surface charging effects, a conducting layer of metal, with typical thicknesses 5-10nm, can be sputtered onto the surface. This layer will transport the excess electrons, reducing the negative charging effects. A negative effect of the sputtered layers is that it may diminish the resolving power of the microscope, since topographical information is no longer gained from the surface of the material, but from the sputtered layer.

Another way to minimise charging effects is to balance the incoming and emitted electron current. The secondary electron yield δ is defined as the number of secondary electrons emitted per incident primary electron. Similarly, the backscattered electron yield η is defined as the fraction of electrons backscattered per primary electron [9]. The total yield per primary electron, $(\delta+\eta)$, is a function of the accelerating voltage as well as the density of the materials studied, as depicted in figure 2.8.

From the graph it is clear that when the energy of the incident beam is smaller than E_1, the total secondary electron yield is smaller than 1, resulting in negative charging of the surface. As a consequence of the negative charging effect, the image will turn white. If $E_1<E<E_2$ then $\delta+\eta>1$, resulting in positive charging of the surface. The image will turn white. To minimise charging effects, the energy of the primary beam should be chosen equal to E_2, being typical 2-3 keV. A conducting layer is then not required, and the balancing of the electron yield will prevent the surface from charging.

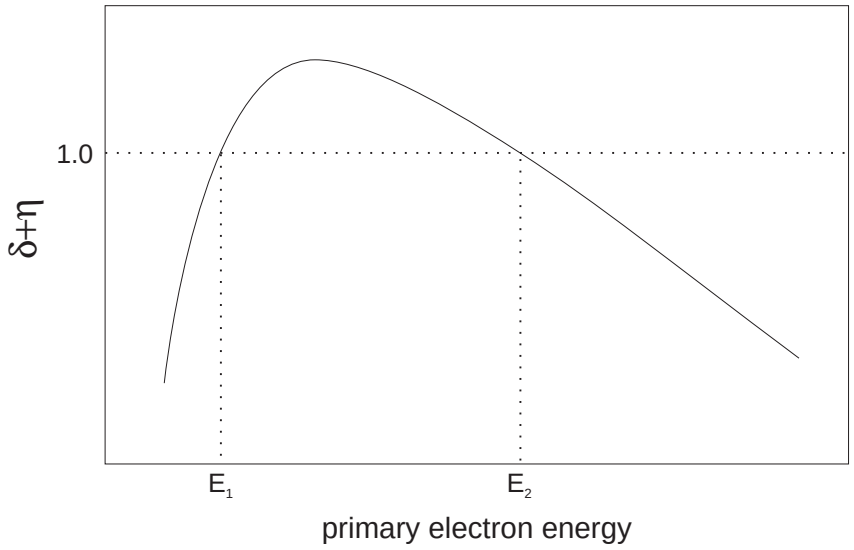

figure 2.8: *Secondary electron yield as a function of accelerating voltage. Adjusting the energy of the primary electrons results in a yield larger or smaller than unity, and hence positive or negative charging of the specimen.*

Charging of the surface is not the only factor determining the resolution of a scanning electron microscope. The width of the electron beam, as described by equation 2.4, is also an important factor for the lateral resolution [10]. A narrow electron beam results in a high resolution. The spot size however, is a function of the accelerating voltage.

$$d_p^2 = \frac{1}{\alpha^2}\left[\underbrace{\frac{i}{B}}_{\text{beam}} + \underbrace{(1.22\lambda)^2}_{\text{diffraction}}\right] + \underbrace{\left(\frac{\Delta E}{E_0}C_c\right)^2\alpha^2}_{\text{chromatic}} + \underbrace{\left(\tfrac{1}{2}C_s\right)^2\alpha^6}_{\text{spherical}} \qquad (2.4)$$

The broadening of the spot size is the sum of broadening due to several processes. The first contributor is the beam itself, B is the brightness of the source, i is the beam current and α its divergence angle. The second part is the contribution due to diffraction of the electrons of wavelength λ by the size of the final aperture. The last two parts are the broadening caused by chromatic and spherical aberrations. In order to achieve the smallest spot size, all contributions should be as small as possible. Decreasing the

accelerating voltage will not only cause the wavelength of the electrons to increase, but also the chromatic aberration increases as well, resulting in increasing of the spot size and, as a consequence, a decrease in resolving power of the microscope.

A field emission gun has a very high brightness B, reducing the contribution in broadening due to the beam itself in equation 2.4. The energy spread ΔE in the electron energies is also small. Together with the fact that the coefficients C_s and C_c can be reduced by optimising the lenses for low-energy electrons, provides the FEG low voltage scanning electron microscope with very high resolving power.

2.4 X-ray diffraction

2.4.1 X-ray diffraction

Similar to visible light, x-rays are diffracted by a grating [11]. One of the requirements for the diffraction of x-rays, and for visible light as well, is that the wavelength of the used radiation is of the same order of magnitude as the spacing of the grating. Using the three dimensional regular and periodic lattice of any crystalline material as a grating, x-rays are diffracted following to a simple equation which is known as Bragg's law

$$n\lambda = 2d\sin\theta \qquad (2.5)$$

In this equation, λ represents the wavelength of the x-radiation used, d is the distance between the lattice planes of the crystal and θ is the diffraction angle. By using monochromatic x-rays of known wavelength λ and measuring the diffraction angle θ, the lattice spacing d_{hkl} of various planes in the crystal can be determined. Since planes in crystals, described by the Miller indices *{hkl}*, all have different interlattice spacings, they also have different diffraction angles. Performing an angular scan for all angles θ therefore delivers a set of diffraction angles which is unique for the material under investigation. It is thus possible to determine from measured diffraction angles the composition and phase of a material.

2.4.2 *Production of x-rays*

Any electrically charged particle which is rapidly decelerated emits x-rays. An x-ray tube exists of two electrodes. Over the electrodes, a high voltage is maintained, accelerating the electrons from the cathode to the anode. The high energy electrons impact on the anode, decelerating very rapidly, hereby radiating x-rays in all directions. The resulting spectrum of these x-rays, shown in figure 2.9, is independent of the used anode material in the tube, for low accelerating voltages.

The intensity is zero up to a certain wavelength, directly correlated to the accelerating voltage, increasing rapidly to a maximum and again decreasing with no sharp limit on the long wavelength side. Radiation represented by such curves is called Bremsstrahlung, from the deceleration of the charged particles. Increasing the accelerating voltage of the electrons results in the emission of characteristic radiation of the target material. This is a result of the high energy electrons impinging on the material, displacing electrons from its shell around the nucleus. When an electron from a higher shell fills up the vacant state left by the displaced electron, it is accompanied by the emission of an x-ray photon with an energy characteristic for the atom

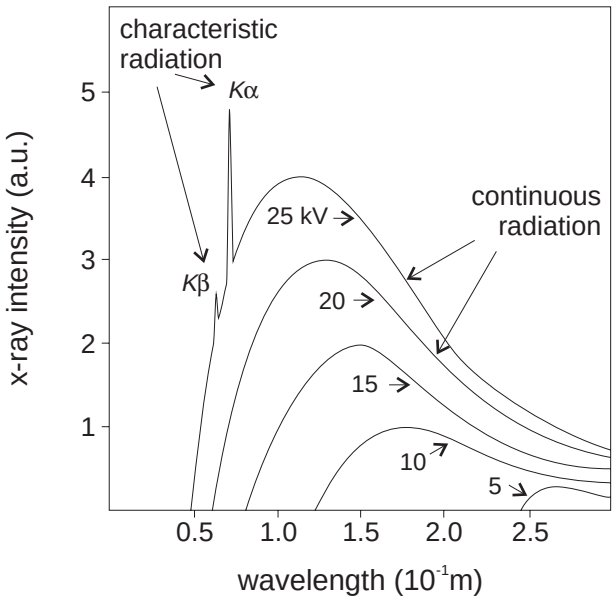

figure 2.9: *Characteristic spectrum of an x-ray tube. The total output is depicted as a function of the accelarating voltage, with the characteristic lines superimposed on the continuous spectrum.*

involved, as is depicted in figure 2.10. These lines fall into several sets, referred to as *K, L, M,* etc., with each line having its own critical excitation voltage. For x-ray diffraction, commonly $K\alpha$ radiation is used. To obtain characteristic radiation from the target material, the applied accelerating voltage has to be at least equal to the excitation energy. The intensity of the radiation increases with the applied voltage according to

$$I = Ai(V - V_k)^{1.5} \tag{2.6}$$

with i the tube current, V the applied voltage, V_k the critical excitation potential and A a constant. The intensity of a $K\alpha$ line of an x-ray tube with a copper target operating at 30 kV, is about 90 times the intensity of the continuous spectrum at the same wavelength.

2.4.3 Interaction of x-rays with matter

The electromagnetic behaviour of x-rays causes them to interact with any charged particle. When, for example, an x-ray beam encounters an electron, the oscillating electric field of the beam will set the electron into oscillatory

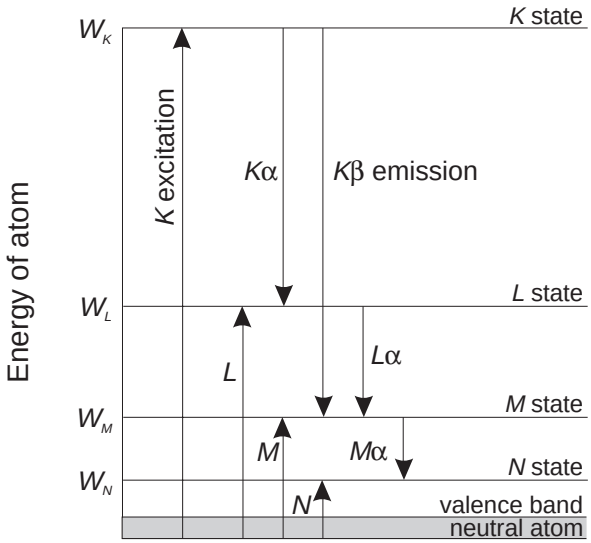

figure 2.10: *Electronic transitions causing emission of characteristic radiation. K radiation is produced when an electron is ejected from the K shell and the L shell supplies the electron to fill the vacancy left in the K shell. Depending upon the spin of the L electron, $K\alpha_1$ or $K\alpha_2$ radiation is produced.*

motion about its mean position. Due to acceleration and deceleration, the electron will emit an electromagnetic wave. An electron is therefore said to scatter an x-ray beam, where the scattered beam is the beam radiated by the electron under the action of the incident beam. The scattered beam has the same wavelength of the incident beam and is referred to be coherent with it, since there is a definite relationship between the phase of the incident and scattered beams.

X-rays are scattered in all directions by an electron. The intensity of the scattered beam depends on the angle of scattering, in a way which was first derived by Thomson, according to

$$I_P = I_0 \frac{K}{r^2}\left(\frac{1+\cos^2(2\theta)}{2}\right) \tag{2.7}$$

Here I_0 is the intensity of the incident beam, K is a constant, r the distance of point P to the scattering electron and 2θ is the scattering angle with respect to the incident beam. The interaction of x-rays with matter does not solely exists of the interaction of the incident x-ray beam and the electrons in the material. The nucleus of an atom also bears a charge and should be capable of oscillating under the influence of the incident beam. However, the nucleus has a relatively large mass and therefore cannot be made to oscillate to any appreciable extent. The net effect is that coherent scattering by an atom is due only to electrons.

The wave scattered by all electrons is however not necessarily the sum of the waves scattered by its component electrons. Only if the scattering is in the forward direction ($2\theta=0$) the waves scattered by all the electrons are in phase and the amplitudes can be added directly. For other scattering directions this is not true. The fact that the scattering electrons of an atom are situated at different points in space introduces differences in phase between the waves scattered by different electrons, resulting in partial interference of the waves. The total diffracted intensity in any direction $2\theta\neq0$ is therefore less than the algebraic sum of waves scattered by the electrons. The atomic scattering factor f is used to describe the efficiency of scattering of an atom in a given direction and is defined by the ratio of amplitudes of the wave scattered by an atom and the wave scattered by an electron.

The scattering of x-rays for loosely bound outer electrons is different from the scattering of x-rays by tightly bound inner electrons. The outer electrons

scatter part of the incident beam and slightly increase its wavelength. The inner electrons are set into oscillation and radiate x-rays of the same wavelength as that of the incident beam. The former is called incoherent and the latter coherent scattering. If the atom, scattering the incident beam, is part of a large group of atoms arranged in space in a regular periodic fashion, then the coherently scattered radiation from all the atoms undergoes reinforcement in certain directions and cancellation in other directions, producing diffracted beams.

If the atoms are arranged regularly and periodically, it is possible and convenient to assign a unit cell to the structure. The intensity of the beam diffracted by a crystal is described by the way in which the atoms are arranged within this unit cell. The phase difference between the wave scattered by an atom at position *B (x,y,z)* and an atom *A (0,0,0)* at the origin is given by

$$\phi = 2\pi(hu + kv + lw) \tag{2.8}$$

in which h, k and l are the Miller indices for the given reflection and u, v and w are the fractional coordinates $\frac{x}{a}$, $\frac{y}{b}$ and $\frac{z}{c}$. Here a, b and c are the unit cell lattice constants. Each scattered wave of an atom in the unit cell is given by

$$Ae^{i\phi} = fe^{2\pi i(hu+kv+lw)} \tag{2.9}$$

with f the atomic scattering factor [12]. Adding all the waves scattered by the individual atoms results in [13]

$$F_{hkl} = \sum_{n=1}^{N} f_n e^{2\pi i(hu_n+kv_n+lw_n)} \tag{2.10}$$

Here F_{hkl} is the so-called structure factor, describing in which way the atomic arrangement, given by u, v and w for each atom, affects the scattered beam. The structure factor expresses both the amplitude and phase of the resulting wave. The magnitude of this complex value is defined as the ratio between the amplitude of the wave scattered by all the atoms of a unit cell and the amplitude of the wave scattered by one electron.

2.4.4 Residual stress determination

Elastic deformation of a polycrystalline material causes the lattice spacings in constituent grains to deviate from their stress-free value d_0 [14]. The stressed value for the lattice spacing, $d_{\phi,\psi}$, will be essentially the same for any particular set of lattice planes *{hkl}* of any grain which is oriented similarly to the stress. Measuring the lattice spacings for differently oriented grains will deliver a set of d_{hkl}-values as a function of the orientation of the grains measured, as depicted in figure 2.11. Using the determined lattice spacings as a strain gauge, the internal or externally applied stress can be determined within the framework of linear elasticity theory.

In the following, relations between the stress state in a specimen and the experimentally detectable lattice strains will be derived in the case of isotropic linear elasticity. Consider the system in figure 2.12.

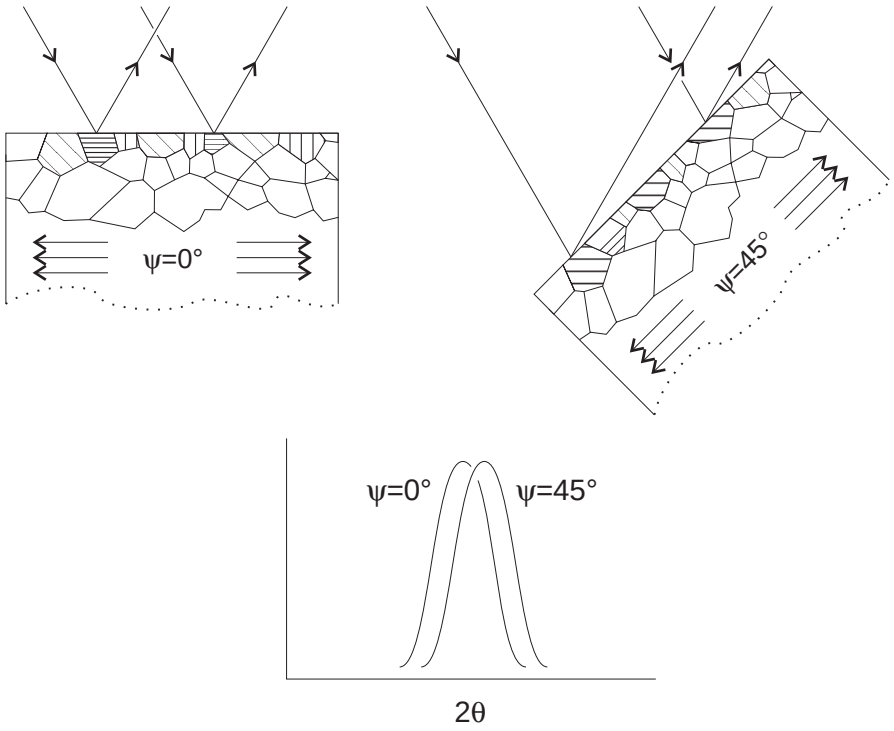

figure 2.11: *Dependence of the lattice strains measured in a crystallite family, and hence the position of the Bragg reflection, as a function of the orientation ψ of the crystallites with respect to the laboratory frame.*

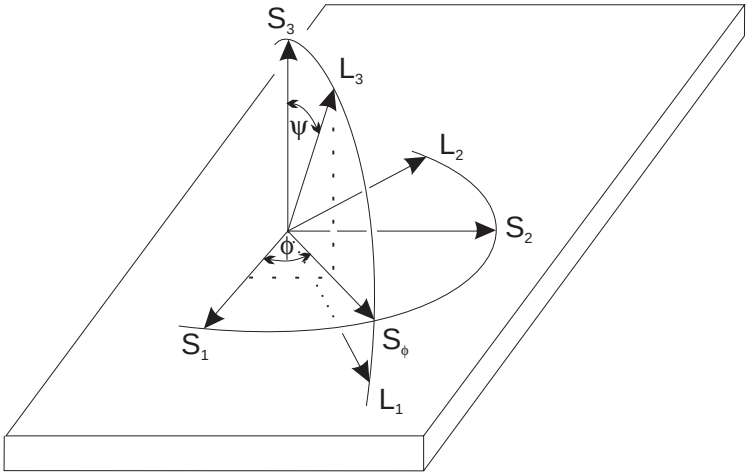

figure 2.12: *Definition of the angles ϕ and ψ determining the orientation of the specimen frame with respect to the laboratory frame.*

Measuring the lattice spacing, $d_{\phi\psi}$, the microstrain for the grain in diffraction is obtained from

$$\varepsilon_{33,L,\phi\psi} = \frac{d_{\phi\psi} - d_0}{d_o} \tag{2.11}$$

with d_0 the measured d-value for $\phi,\psi=0$. Transformation of this strain from the laboratory system to the specimen system, readily delivers a relation between measured strain and the strain components in the specimen.

$$\begin{aligned}\varepsilon_{33,L,\phi\psi} = {} & \varepsilon_{11}\cos^2\phi\sin^2\psi + \varepsilon_{12}\sin 2\phi\sin^2\psi \\ & + \varepsilon_{22}\sin^2\phi\sin^2\psi + \varepsilon_{33}\cos^2\psi \\ & + \varepsilon_{13}\cos\phi\sin 2\psi + \varepsilon_{23}\sin\phi\sin 2\psi\end{aligned} \tag{2.12}$$

Transformation of the strains to macrostresses then yields

$$\begin{aligned}\varepsilon_{33,L,\phi\psi} = {} & \frac{1+\nu}{E}\left(\sigma_{11}\cos^2\phi + \sigma_{12}\sin 2\phi + \sigma_{22}\sin^2\phi - \sigma_{33}\right)\sin^2\psi \\ & + \frac{1+\nu}{E}\sigma_{33} - \frac{\nu}{E}(\sigma_{11} + \sigma_{22} + \sigma_{33}) \\ & + \frac{1+\nu}{E}(\sigma_{13}\cos\phi + \sigma_{23}\sin\phi)\sin 2\psi\end{aligned} \tag{2.13}$$

where E is the Young's modulus and ν represents the Poisson's ratio, the latter of which is the ratio between lateral contraction and axial expansion of a material under an uniaxial stress. From equation 2.13 it is seen that in the biaxial stress case, where the only non-zero entries in the stress tensor are σ_{11} and σ_{22}, the measured strain is a function of ϕ and ψ only. This causes equation 2.13 to transform into

$$\varepsilon_{33,L,\phi\psi} = \frac{1+\nu}{E}\left(\sigma_{11}\cos^2\phi + \sigma_{22}\sin^2\phi\right)\sin^2\psi - \frac{\nu}{E}(\sigma_{11}+\sigma_{22}) \qquad (2.14)$$

With this relation, the macroscopic stress state of the material can be determined. If we assume $\sigma_{11}=\sigma_{22}=\sigma_\phi$ and if stresses only acting in the ϕ–direction are of interest, equation 2.14 may be rewritten in its concise and commonly used form

$$\varepsilon = \frac{1+\nu}{E}\sigma_\phi \sin^2\psi \qquad (2.15)$$

In practice, stresses in materials are determined by measuring Bragg reflections for several specimen orientations ψ. Provided that the material constants are known, the stress σ_ϕ can be calculated from the gradient of determined lattice spacings $d_{\phi\psi}$ as a function of specimen orientation ψ. Neglecting the second part of equation 2.14 does not introduce an error in the determination of values for σ_ϕ since it does not exhibit ψ-dependence. However, a serious error in the stress values is introduced by using incorrect values for the material constants E and ν. Although in literature the macroscopic material constants are commonly used, these material constants may deviate from the plane specific x-ray elastic constants, for the isotropic linear elastic case being defined as $S_1^{hkl} = -\frac{\nu}{E}$ and $\frac{1}{2}S_2^{hkl} = \frac{1+\nu}{E}$. For the anisotropic case the x-ray elastic constants can be calculated from the single crystal elastic constants using either the Reuss or Voigt approximation.

The assumption in the Reuss model is that in all the crystallites the stress is identical [15]. The measured strains in the laboratory system of any polycrystalline material are described by equation 2.16

$$\varepsilon_{33,L} = \frac{\int_0^{2\pi} \varepsilon_{33,L}(\lambda) f(\lambda) d\lambda}{\int_0^{2\pi} f(\lambda) d\lambda} \tag{2.16}$$

In this general expression, $\varepsilon_{33,L}(\lambda)$ stands for the elastic strain in the direction L_3, depending on ψ and ϕ. $f(\lambda)$ Is the crystallite orientation distribution function that describes the crystallographic texture. λ Is the angle of rotation around L_3 which brings a crystallite, which is for λ=0° in diffraction, also in a preferred orientation, as is graphically depicted in figure 2.13. Since the stress $\sigma_{ij,L}$ is independent of λ, equation 2.16 leads to

$$\varepsilon_{33,L} = r^R_{33ij,L}\sigma_{ij,L} \tag{2.17}$$

In this equation, $r^R_{33ij,L}$ are the x-ray elastic compliances according to Reuss. They can be calculated as follows

$$r^R_{33ij,L} = \frac{\int_0^{2\pi} S_{33ij,L}(\lambda) f(\lambda) d\lambda}{\int_0^{2\pi} f(\lambda) d\lambda} \tag{2.18}$$

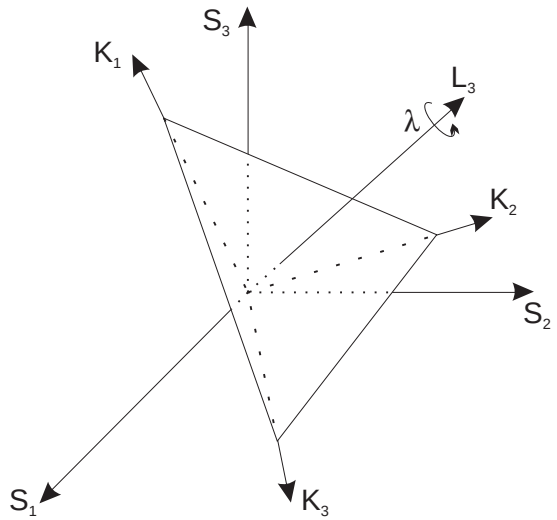

figure 2.13: *Definition of λ. K_1, K_2 and K_3 are (100), (010) and (001) directions of a crystallite in diffraction. λ Is the angle that rotates this crystallite into other crystallites in diffracting positions.*

in which $S_{33ij,L}(\lambda)$ are the expressions of the elastic compliances in the laboratory system

$$S_{33ij,L}(\lambda) = a_{3k}a_{3l}a_{im}a_{jn}S_{klmn} \tag{2.19}$$

The a_{ij} are the matrix elements of the Euler transformation between L_i, the laboratory system, and K_j, the crystallite coordinate system They are independent of ϕ and ψ but they do depend on λ. The S_{klmn} are the elastic compliances of a single crystallite as expressed with respect to the principal crystal directions. If the material under investigation is isotropic, equation 2.18 simplifies very much because $f(\lambda)$ is then always equal to 1. For cubic materials, as an example, analytical solutions can be derived for the x-ray elastic constants depending only on the Miller indices *{hkl}* of the diffracting plane and the elastic compliances S_{ijkl} [16].

$$\begin{aligned} S_1 &= S_{1122} + \Gamma S_0 & S_0 &= S_{1111} - S_{1122} - 2S_{1212} \\ \tfrac{1}{2}S_2 &= S_{1111} - S_{1122} - 3\Gamma S_0 & \Gamma &= \frac{h^2k^2 + k^2l^2 + l^2h^2}{h^2 + k^2 + l^2} \end{aligned} \tag{2.20}$$

The Voigt model, in contrast to the Reuss model, assumes that in all the crystallites the elastic strains are equal [17]. This leaves the stress in every crystallite to be different

$$\sigma_{ij}(g) = C_{ijkl,S}(g)\varepsilon_{kl} \tag{2.21}$$

Here $C_{ijkl,S}(g)$ are the elastic constants transformed from the crystal system (*K*-system) to the sample system (*S*-system). An average stress can be defined by the integration over all grains

$$\overline{\sigma_{ij}} = \int \sigma_{ij}(g)f(g)dg \tag{2.22}$$

An expression for the uniform strain can now be derived

$$\varepsilon_{ij} = r^V_{ijkl}\overline{\sigma_{kl}} \tag{2.23}$$

The r^V_{ijkl} are the elastic compliances according to Voigt. In contrast to the Reuss model they are independent of the diffraction planes *{hkl}*.

Replacing the stresses in equations 2.17-2.19 by the average stress $\overline{\sigma_{ij}}$ and the Reuss elastic compliances by the elastic compliances according to Voigt, delivers the x-ray elastic constants according to Voigt. For cubic materials and the isotropic case they have been reported by Voigt

$$S_1 = \frac{2S_0(S_{1111} + 2S_{1122}) + 20S_{1122}S_{1212}}{6S_0 + 20S_{1212}}$$

$$\tfrac{1}{2}S_2 = \frac{20S_{1111}S_{1212} - 20S_{1122}S_{1212}}{6S_0 + 20S_{1212}} \qquad (2.24)$$

$$S_0 = S_{1111} - S_{1122} - 2S_{1212}$$

From the two models it is clear that the x-ray elastic constants derived from various assumptions deliver different values. If the constants are plotted as a function of Γ, as in figure 2.14, a range can be given in which the true x-ray elastic constants are to be expected.

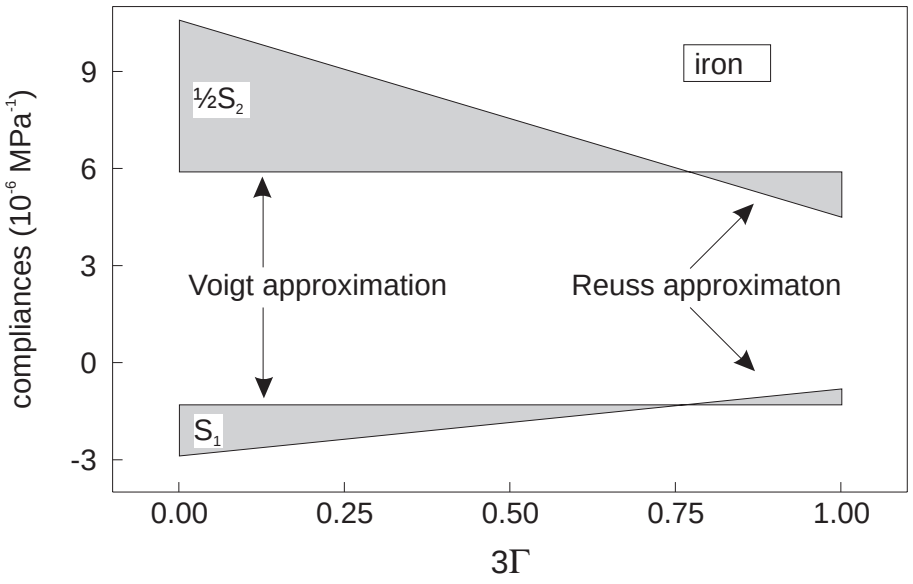

figure 2.14: *Comparison between the compliances in the Reuss and Voigt approximation as a function of Γ{h,k,l}. The true elastic constants are expected in the shaded region.*

For materials with isotropic hexagonal crystal structure the expressions for S_1 and $½S_2$ are given in the Reuss approximation by [18]

$$\begin{aligned} S_1 &= \tfrac{1}{2}(S_{1122} + S_{3322)} \\ &\quad + \tfrac{1}{2}(S_{1111} + S_{3333} - S_{3322} - S_{1122} - 4S_{2323})l^2 \\ &\quad - \tfrac{1}{2}(S_{1111} + S_{3333} - 2S_{3322} - 4S_{2323})l^4 \end{aligned} \qquad (2.25)$$

$$\begin{aligned} \tfrac{1}{2}S_2 &= \tfrac{1}{2}(2S_{1111} - S_{1122} - S_{3322}) \\ &\quad - \tfrac{1}{2}(5S_{111} + S_{3333} - 5S_{3322} - S_{1122} - 12S_{2323})l^2 \\ &\quad + \tfrac{3}{2}(S_{1111} + S_{3333} - 2S_{3322} - 4S_{2323})l^4 \end{aligned}$$

with $l^2=cos^2\Phi$ and Φ the angle between the *(0001)* axis and the normal to the *{hkil}* plane used for the diffraction experiment. Using the Voigt approximation, the expressions read

$$\begin{aligned} S_1 &= \frac{3(C_{2323} - C_{1111} - C_{3333} - 5C_{1122} - 8C_{3322})}{2C_{1111} + C_{3333} + 2C_{1122} + 4C_{3322}} \\ &\quad * (7C_{1111} + 2C_{3333} - 5C_{1122} - 4C_{3322} + 3C_{2323}) \end{aligned} \qquad (2.26)$$

$$\tfrac{1}{2}S_2 = \frac{15}{7C_{1111} + 2C_{3333} - 5C_{1212} - 4C_{3322} + 3C_{2323}}$$

2.4.5 X-ray elastic constants

To exclude errors introduced by approximating the x-ray elastic constants by averaged values, it would be more appropriate to actually measure these. A suitable technique consists of subjecting a specimen to several applied loads, and measuring the elastic response of planes of interest as a function of crystallite orientation [19]. External loading of a specimen causes equation 2.14 to transform into a new form in which the applied load is, within the framework of linear elasticity, superposed upon the internal stress state in the material.

$$\varepsilon_{33,\phi=0,\psi} = \tfrac{1}{2}S_2^{hkl}\left(\sigma_\phi^{IS} + \sigma^{AS}\right)\sin^2\psi + S_1^{hkl}\left(\sigma_{11}^{IS} + \sigma_{22}^{IS} + \sigma^{AS}\right) \qquad (2.27)$$

The superscripts *IS* and *AS* stand for internal stress and applied stress, respectively. To derive the x-ray elastic constants from this relation, the response of the lattice strains for applied loads and crystal orientations is determined. This is done by taking the derivative of equation 2.27 with respect to applied stress, σ^{AS}. The gradient of the equation now delivers $\frac{1}{2}S_2^{hkl}$ and the abscissa S_1^{hkl}.

References

1 C. He, Y.S. Wang, J.S. Wallace and S.M. Hsu, Wear, **162**, (1993), 314.

2 Y. Matsumoto, K. Hirota and O. Yamaguchi, J. Am. Ceram. Soc., **76**, (1993), 2677.

3 H. Harada and T. Sakuma, J. Ceram. Soc. Jap., **99**, (1991), 132.

4 L.C. Stearns and M.P. Harmer, J. Am. Ceram. Soc., **79**, (1996), 3013.

5 C.J. Brinker and G.W. Scherrer, Sol-Gel Science, Academic Press, San Diego, (1990).

6 L.E. Scriven, Mat. Res. Soc. Symp. Proc., **121**, (1988), 717.

7 D. Meyerhofer, J. Appl. Phys., **49**, (1978), 3993.

8 F. van Looyengoed, Thesis, Rijksuniversiteit Groningen, (1996), 19.

9 J.H. Butler, D.C. Joy, G.F. Bradley and S.J. Krause, Polymer, **36**, 1995, 1781.

10 J.I Goldstein, D.E. Newbury, P. Echlin, D.C. Joy, C. Fiori and E. Lifshin, Scanning Electron Microscopy and X-ray Microanalysis, Plenum, New York, (1981), 44.

11 M.J. Buerger, X-ray Crystallography, John Wiley and Sons, New York, (1953), 29.

12 N.W. Ashcroft and N.D. Mermin, Solid State Physics, Saunders College Publishing, Philadelphia, (1976), 107.

13 B.E. Warren, X-ray Diffraction, Addison-Wesley, Massachusetts, (1969), 31.

14 B.D. Cullity, Elements of x-ray diffraction, Addison-Wesley, Massachusetts, (1978), 447.

15 A. Reuss, Z. für angew. Math. and Mech., **9**, (1929), 49

16 H. Möller and G. Martin, Mitt. K.-Wilhelm-Inst. Eisenforsch., **21**, (1939), 261.

17 W. Voigt, Lehrbuch der Kristallphysik, Teubner-Verlag, Berlin, (1928).

18 P.D. Evenschor, W. Frohlich and V. Hauk, Z. Metallk., **62**, (1971), 38.

19 I.C. Noyan and J.B. Cohen, Residual Stress, measurements by diffraction and interpretation, Springer-Verlag, New-York, (1987), 145.

3 STRAIN EFFECTS DURING CURING

Introduction

To understand the residual stress state of a material, it is necessary to know what may cause the evolution of the stresses. Residual stresses arise when a material stays constrained in a strained state. Straining of the material may take place throughout the production phase of the material. Strains may be induced through thermal treatments of the material, mechanical treatments like grinding or machining, or even the material itself may give rise to straining of discrete parts within the material, e.g. as a result of a phase transformation. All these strains induce stresses in the material which may persist after the processing of the material. These stresses are the so-called residual stresses.

In the first section of this chapter, the sintering process will be discussed. During the curing of powder compacts, diffusional mechanisms in the material induce densification in the product by reducing the total pore volume. When a powder compact densifies faster from one region to another, local straining of the powder compact may arise.

Consequently, the influence of a second phase on the densification of the matrix material will be studied. The addition of a second phase to the ceramic matrix may not only alter the densification rate of the matrix, but may also change the mechanical properties of the matrix. In this thesis the addition of ZrO_2 to an α-alumina matrix is considered.

Finite elements calculations will be employed to simulate the residual stress state in the specimen after the curing process. The magnitude and the sign of the stress components in both layers of the pellet play an important role in the eventual mechanical behaviour of the ceramic product.

3.1 Sintering

3.1.1 Densification mechanisms during sintering.

The precursor powders are compacted and formed in a uniaxially pressing process. After forming the green products, they are densified in a sintering process. During this sintering process, the powder compact densifies from

the initial density achieved in the compaction stage to a final density, depending on the material properties, the compaction process and the parameters used during sintering. The free-energy change that gives rise to densification is the decrease in surface area and the elimination of solid-vapor interfaces [1-7]. Commonly, the sintering process is divided into multiple, typical three, separate stages, based on the geometry of the pore structure and the density of the powder compact [8]. Several mechanisms contribute to the densification in every stage.

In the compaction stage, the separate particles are placed in contact and adhere through Van der Waals forces. Subsequently, the contact, or neck, develops by material that is transported out of the contact area by grain boundary diffusion and by material that flows to the neck region by surface diffusion. This stage may be enhanced by applying an external force to increase the number of contacts between the particles in the powder compact and to achieve a greater packing density through plastic deformations of the particles [9,10]. The boundary conditions for densification in the sintering process are defined in this stage, e.g. by tailoring the particle size distribution and the pore size distribution. Therefore, this stage is referred to as stage 0.

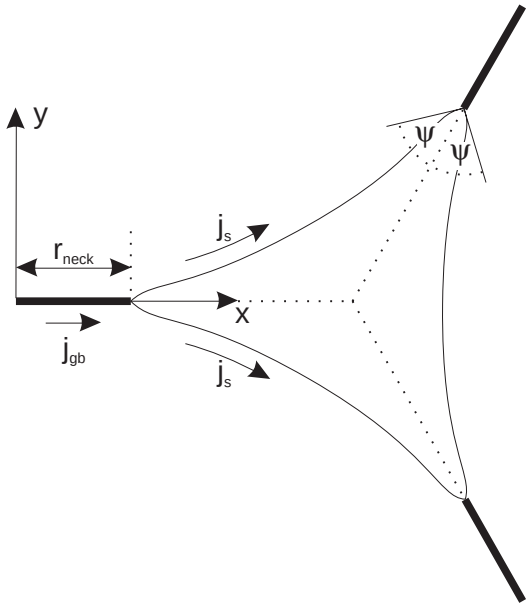

figuur 3.1: *Definition of material fluxes by grain boundary and surface diffusion during the sinter process.*

In the next stage, stage 1, necks between interconnecting particles grow rapidly by diffusional processes. Due to the densification in the compact, the average number of contacts per particle increases. The processes taking place in this stage are schematically depicted in figure 2.5. The only mechanisms contributing to the densification of the compact are mechanism 4, grain boundary diffusion, and mechanism 5, lattice diffusion. The other mechanism merely reduce the driving force for densification by rounding the neck between the interconnecting particles. Stage 1 sintering leads to connected, roughly cylindrical pores, which shrink in radius in stage 2 of the sintering process. During this stage, as already discussed in section 2.2.2, the densification mechanisms are lattice and boundary diffusion.

In the final stage the pores become isolated. Their shapes are roughly spherical. In contrast to the intermediate stage, stage 2, where any gas in the pores may escape to the surface through the interconnecting pores, entrapped gas in the pores in this stage causes the pressure in the pores to rise as they shrink further.

The diffusional mechanisms dictating densification in stage 2, lattice and grain boundary diffusion, are governed through the fluxes of atoms along the surface, j_s, and the grain boundary, j_{gb}, as depicted in figure 3.1, according to [6,11]

$$j_s = \frac{-2\gamma_s \Omega \delta_s D_s}{kT} \nabla \kappa$$

$$j_{gb} = \frac{\Omega \delta_{gb} D_{gb}}{kT} \nabla \sigma_n \qquad (3.1)$$

Here γ_s is the surface energy per unit area, Ω is the atomic volume, D_s and D_{gb} are the transport coefficients for surface and grain boundary diffusion (in m^3 s^{-1}), respectively, δ_s and δ_{gb} are the surface diffusive width (Ω times the number of atoms per unit area) and the grain boundary diffusive width, respectively, k is Boltzmann's constant, T the absolute temperature, κ is the mean curvature of the pore surface and σ_n is the normal component of the stress acting on the grain boundary.

Using equations 3.1, the total amount of material transported from the grain boundary and the lattice to the neck may be derived, hence the densification of the compact may be derived if the number of contacts per particle in the

powder compact is known. In the case of sintering mechanisms governed by either lattice diffusion or grain boundary diffusion, the rate equation is given by [12]

$$\frac{d\rho}{dt} = \frac{f(\rho)}{kTr^m} D_0 \exp\left(\frac{-Q}{kT}\right) \tag{3.2}$$

Here $f(\rho)$ is a function of the density, reducing to 0 for ρ=0 and ρ=1, and r is the particle size. D_o and Q are the prefactor and activation energy for lattice or grain boundary diffusion. Together with the exponent m, m=3 for lattice diffusion and m=4 for grain boundary diffusion, they describe the densification rate for the powder compact during the sintering process.

Several models have been derived for the densification as a function of material properties, powder compact packing properties, pore size distributions and particle size distributions [13-20]. Here, a procedure proposed by Ashby et al. is followed to determine the densification as a function of processing conditions, material properties and initial particle sizes [21-23].

In the model, a particle distribution is used which consists of monosized particles, made up of separate grains. These particles are compacted to an initial density, which is typically taken as ~60-75% of the theoretical density of the material, depending upon the compaction process. Consequently, the pore radius and the number of contacts per particle are calculated for both the intermediate and the final state.

$$\begin{aligned} Z &= 12\rho \quad r_n = r(\rho - \rho_0) && \text{for the initial state} \\ r_p &= r\left(\frac{1-\rho}{6}\right)^{\frac{1}{3}} && \text{for the final state} \end{aligned} \tag{3.3}$$

Here, Z is the number of contacts per particle, r_n is the curvature of the neck between interconnecting particles, ρ is the density, ρ_0 is the initial density, r_p is the pore radius and r is the particle radius. Then, using material properties like the diffusional constants for grain boundary diffusion and surface diffusion, the main diffusional mechanism for the processing parameters, sintering temperature and time, are determined. The densification rate by boundary diffusion during the initial stage is given by [24]

$$\dot{\rho} = \frac{12\rho^{1/3}\rho_0^{2/3}}{g(\rho)} \frac{(\delta D_b + r_n D_v)}{kTr^3} Z\Omega P \qquad (3.4)$$

Here δD_b and D_v are the diffusion coefficients, δD_b is the grain boundary thickness times the grain boundary diffusion coefficient, D_v is the lattice diffusion coefficient, k is Boltzmann's constant, T the absolute temperature, Z is given by equation 3.3, Ω is the atomic volume and P the external curing pressure.

Erroneous densification rates may be predicted if the assumptions made in the model are not justified. The most important of the effects influencing the densification rate equations is grain growth during the sintering process. For short sintering times, the influence of grain growth is little, but when sintering times increase, grain growth may become a problem. This is due to the effect that grain growth may remove many of the necks between particles, suppressing diffusional densification by grain boundary diffusion.

Experimental

The pellets described in section 2.1 are made from precursor α-alumina powder. For this powder, several sintering maps are determined using the described procedure. To calculate the densification rates, the powder properties have to be known. The material properties for α-alumina are listed in table 3.1.

table 3.1: material properties α-alumina [25,26]

parameter		prefactor/constant	activation energy
boundary diffusion	δD_{gb}	$8.6\ 10^{-10}$ m^3 s^{-1}	419.0 kJ mol^{-1}
lattice diffusion	D_l	$2.8\ 10^{-3}$ m^2 s^{-1}	477.0 kJ mol^{-1}
surface diffusion	D_s	$5.0\ 10^{-6}$ m^3 s^{-1}	544.0 kJ mol^{-1}
melting point	T_m	2320 K	
surface energy	γ_s	0.90 J m^{-2}	
atomic volume	Ω	$4.25\ 10^{-29}$ m^3	
solid density	ρ_s	3987.0 kg m^{-3}	
initial density	ρ	0.73	

To calculate the densification rate equations, the particle size and the grain sizes in the particles are also required. Using a method known as the linear

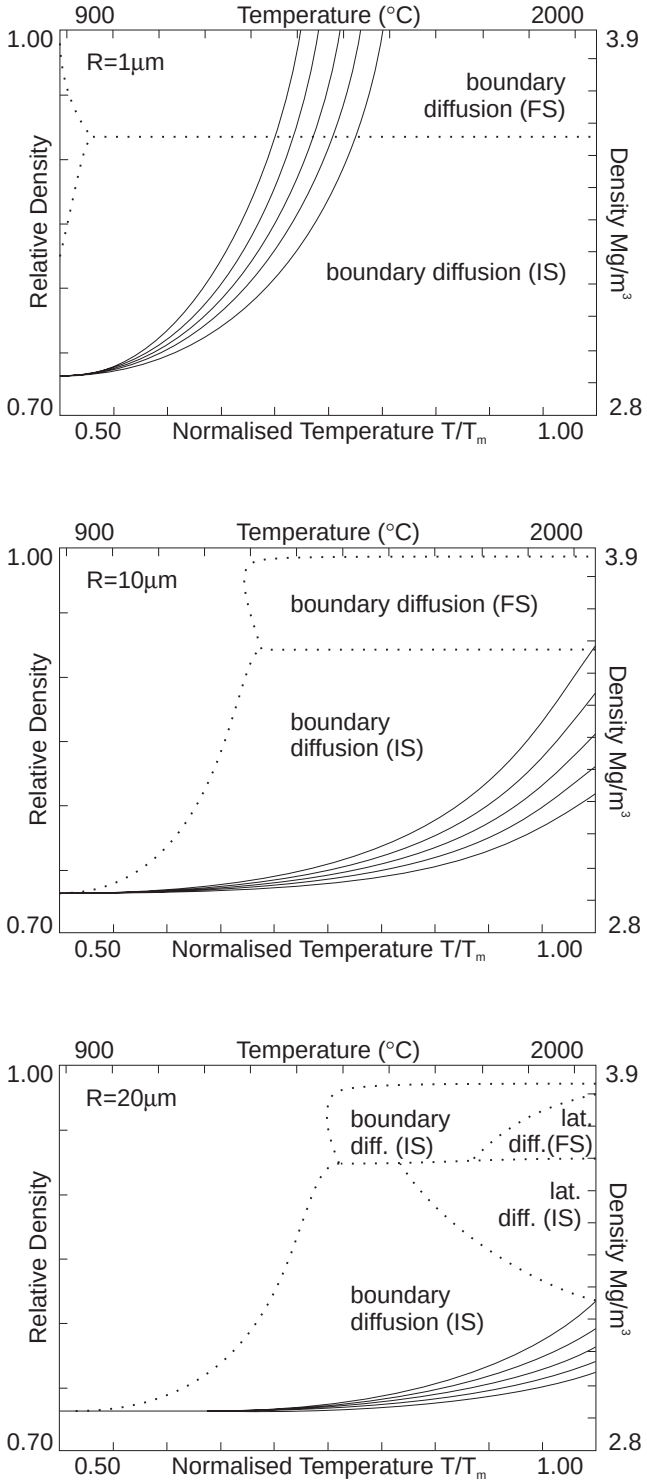

figuur 3.2: *Calculation of densification curves during the sinter process. In the graphs the densification as a function of homologeous temperature is plotted depending on the sinter time (0.25-4 hours) for various starting particle sizes (1-20 µm). The densifying mechanisms for the several sinter temperature regimes are indicated.*

interception method, which will be discussed in more detail in section 4.2, a micrograph of the precursor powder (see figure 2.1) yields a value for the average grain size in the powder compact. A similar procedure is followed to derive the average size of the grains within the particles. The values determined for the average particle and grain sizes are listed in table 3.2.

table 3.2: average particle/grain sizes

grain size	100 nm
particle size	10 μm

Using the average grain size and particle size of the powder compact together with the material properties, densification maps are determined. In figure 3.2 the calculated maps are displayed. The displayed maps are determined for powder compacts containing particles of a size of 1μm, 10mm and 20μm, respectively. Since in the determination of the sintering maps a monosized particle distributions is assumed, a different curve is obtained for powder compacts which do not contain monosized particle size distributions. Nevertheless, it is still an indication for the densification behaviour of the powder compact and the main densification mechanisms are determined for the processing parameters used.

From the maps it is seen that the main densification mechanism for the three different particle sizes is grain boundary diffusion. This holds for both intermediate and final stage sintering. For the 20 μm particle sizes, lattice diffusion becomes important for high, that is larger than ~1600°C, sintering temperatures. For increasing particle sizes, the average number of contacts between particles per unit volume decreases, which increases the influence of bulk diffusion over grain boundary diffusion, explaining the increasing influence of bulk diffusion. The solid curves in the graphs represent the amount of densification attained for a specific curing time as a function of sintering temperature. From the different maps it is seen that the powders with smaller particle sizes densify faster than powders made up of larger particles.

Discussion

The densification maps show that the main mechanism for densification is grain boundary diffusion, for the three precursor powders considered. Densification initiates at lower sintering temperatures for powders with

small particle sizes and solid density is attained at lower temperatures. The effect of grain growth is not incorporated in these calculations and this may influence the sintering behaviour as will be discussed in section 4.2. Examination of the densification behaviour for powder aggregates with larger particle sizes, indicates that a transition in diffusion mechanism takes place from grain boundary to lattice diffusion. The increase of grain sizes in the powder compact does not only reduce the number of contacts between interconnecting particles per unit volume, but the number of grain boundaries in the powder compact is reduced as well. Therefore, the contribution of lattice diffusion becomes more relevant to the densification process for larger particles.

3.1.2 Zirconia addition

Zirconia is used as an additive in the α-alumina matrix to tailor the properties of the matrix [27-29]. The addition of a second phase may have an effect both on densification behaviour and on grain size development of the matrix. To study the differences in densification behaviour, the shrinkage of ceramic specimen during the sinter process is recorded as a function of curing temperature. The experimental densification curves for the layers of the pellets are displayed in figure 3.3.

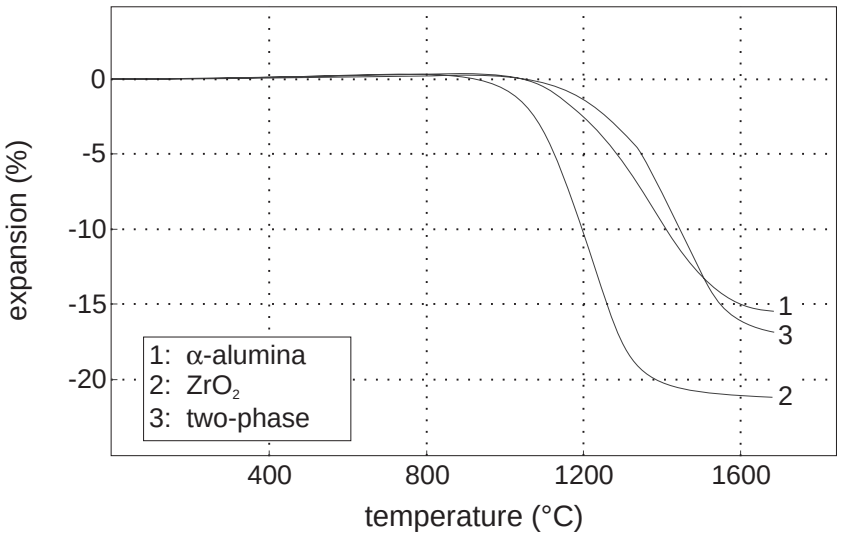

figuur 3.3: *Experimental densification curves for various ceramic powder compacts during the sinter process. The expansion of the powder compact is plotted as a function of the curing temperature for both homogeneous as well as the two-phase material.*

In figure 3.3, the experimental densification curves as a function of sintering temperature are plotted for the α-alumina, zirconia and the two-phase material, containing 20 wt% ZrO_2, respectively. From the curves it is seen that densification of the pure zirconia material starts at lower temperatures than for the two-phase and α-alumina material. Furthermore, the curve of the pure ZrO_2 pellet exhibits only a small gradient for temperatures higher than 1400°C, indicating that the densification at this stage is little and the sintered material is approaching theoretical density.

The densification in the two-phase material and the α-alumina material starts at temperatures larger than the densification onset temperature of ZrO_2. During the first stage, densification in the homogeneous material is stronger than in the two-phase material. In the intermediate stage the gradient of the densification curve is steeper for the two-phase material than for the homogeneous material. The two-phase material densifies faster during this stage. At the end of the final stage, the total shrinkage is larger for the two-phase material than for the homogeneous α-alumina. Assuming that the density in stage 0, the mechanical compaction step, is comparable for both the homogeneous material and the two-phase material, this may be an indication that the densification in the homogeneous material is inhibited.

An explanation for the lower densification in the homogeneous material is the growth of grains in the alumina matrix, reducing the amount of grain boundaries and hence grain boundary diffusion is restrained. The larger shrinkage of the pure ZrO_2 may be explained by non-equal densification in the compaction step. The initial density is a function of the particle size distribution and the material properties, e.g. if the material has a low yield strength, the powder compact may reach higher densities. If the initial density of the powder compact is smaller, larger shrinkage of the product during the sintering step can take place before solid density is reached in the compact.

ZrO_2 is used as an additive in ceramic matrices for its strengthening properties. The strengthening effect is accomplished through a phase transformation in the dispersed ZrO_2 particles [30-32]. Pure ZrO_2 is known to transform from the tetragonal phase to the monoclinic phase upon cooling [33]. The transformation temperature for pure ZrO_2 is ~1240°C. A sample of pure ZrO_2 cooled down to room temperature is completely monoclinic and cracked, due to the dimensional changes accompanied by the phase transformation.

The phase transformation from the tetragonal to the monoclinic symmetry is a displacive transformation, i.e. it is a diffusionless and the a-thermal change of lattice symmetry which occurs instantly when the driving force is sufficiently high [34]. The transformation involves no long-range diffusion processes. Since the monoclinic unit cell has larger dimensions than the tetragonal unit cell, the increase in volume is about 4%. Strains accompanied with the transformation are compressive. The transformation takes place under elastic constraints from the matrix. Depending upon the grain size of the dispersed ZrO_2 particles, the volume expansion can overcome the elastic constraint exerted by the matrix and the transformation may occur spontaneously upon cooling down to room temperature [35]. If the ZrO_2 particles are transformed in the matrix, the accompanying strains may induce microcracks in the α-alumina matrix, surrounding the particles. These microcracks can extend and absorb additional fracture energy when a macroscopic crack is propagating through the material, thereby increasing the toughness of the material. This process is referred to as transformation toughening.

If the size of the ZrO_2 falls below a critical size, no transformation occurs on cooling, retaining the metastable phase down to room temperature. In the stress field of a propagating macrocrack, however, the transformation may be induced by large tensile stresses ahead of the crack tip, increasing the crack resistance and fracture toughness through absorption of energy from the external stress for the phase transformation. This process is known as stress-induced transformation toughening.

Since the strains accompanied with the phase transformation are of influence on the microresidual stress state, they may influence x-ray residual stress measurements. Second order residual stresses locally modify the macro residual stress state, imposing a random distribution of lattice strains upon the global lattice strains. As a result, measured line profiles are broadened, however, the lattice strain of interest for the macro residual stress measurements may still be determined, since only the shift of the line profiles is used to determine the macroscopic residual stress state.

To tackle the influence of the volumetric change of the material, ZrO_2 may be stabilised in the tetragonal phase [36]. This stabilisation of the material in the tetragonal phase is achieved by adding a stabiliser to the ZrO_2. Common stabilisers for the ZrO_2 system are for instance Mg, Y or Ce. The added ZrO_2 in the two-phase pellets, is stabilised using 3w% Y_2O_3. To investigate if phase

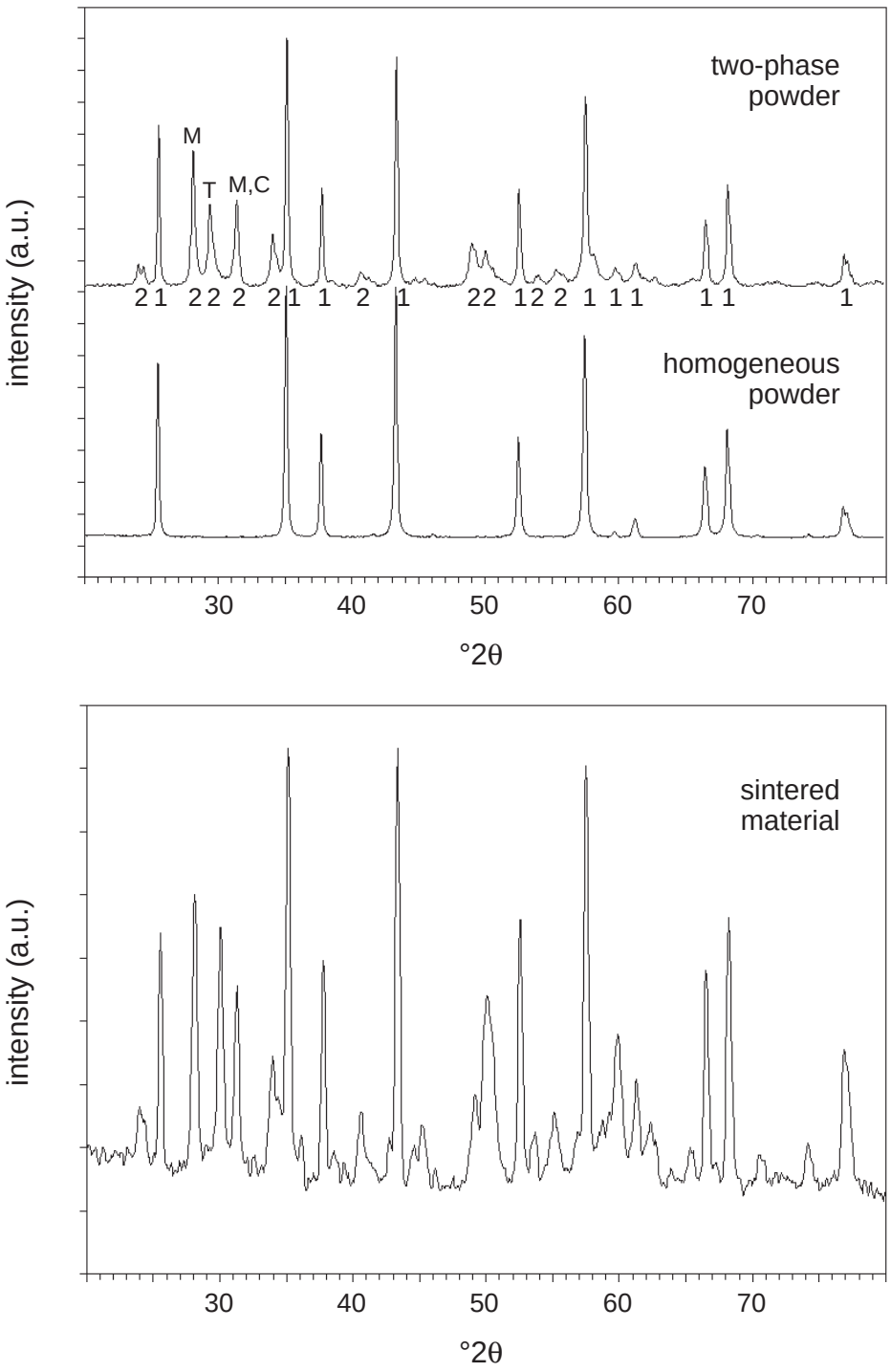

figure 3.4: *X-ray diffractograms of the homogeneous and heterogeneous precursor powders as well as the sintered two-phase material. Bragg reflections labelled 1 arise from the α-alumina phase in the two-phase material whereas reflections labelled 2 originate from the ZrO_2 phase.*

transformations occurred in the ZrO_2 particles during the sintering process of the two-phase material, diffractograms are made from the precursor powder as well as from the uniaxial pressed and sintered pellets. Both diffractogramms may serve as a check whether or not phase transformations have taken place. In figure 3.4.*a*, two diffractograms are displayed of the precursor powders of both the homogeneous phase and the two-phase material.

The Bragg reflections labelled 1 are caused by Al_2O_3 crystallites, reflections labelled 2 are diffracted by ZrO_2 crystallites. Reflections of interest, due to the monoclinic and the tetragonal or cubic phase are labelled *M, T* and *C*, respectively. Using relation 3.5 the volume fraction of the monoclinic phase may be derived from the diffractograms [37].

$$f_m = \frac{2.374\, I^{M}_{(11\bar{1})}}{2.374\, I^{M}_{(11\bar{1})} + I^{T+C}_{(111)}} \tag{3.5}$$

In the expression the intensities, as defined as the area under the peak, are required for the monoclinic and tetragonal, cubic reflections of the lattice sets indicated. From figure 3.4.*a* and relation 3.5 the monoclinic volume fraction is determined at 0.73. To determine if the ZrO_2 has transformed during the sintering process, a diffractogram of a pellet after sintering is also recorded, as depicted in figure 3.4.*b*. Using expression 3.5 and figure 3.4.*b* the monoclinic volume fraction in the sintered material is determined at 0.74.

The diffractograms of both the sintered and the non cured two-phase powder indicate that the amount of transformed ZrO_2 is little. For both materials the volume fraction monoclinic ZrO_2 is comparable. Therefore, during sintering of the two-phase material, only little transformation strains are induced in the two-phase material.

3.2 Strain evolution

3.2.1 Densification mismatch of both layers

During the sintering step in the processing of pellet material, the layers will shrink through the densifying effects. The amount of shrinkage during the sintering step is a function of the initial density of the powder compacts, the densifying qualities of the material and the processing parameters. From

figure 3.3 it is seen that the α-alumina material and the two-phase material exhibit comparable densification curves. The differences in densification for both materials is that the homogeneous material densifies faster in the first and intermediate stages of the sintering process, but the heterogeneous material exhibits faster densification in the final stage. Assuming that the initial densities are comparable for both powder compacts, the total shrinkage of the heterogeneous material is larger than the total shrinkage of the homogeneous material.

This difference in shrinkage for both materials may give rise to the evolution of densification strain fields in the pellet material. Especially for the simultaneously processed pellets these densification strains are important. This is in contrast to the separate processed pellet, in which the layers are densified in the pre-sintering process. Hence differences in shrinkage will not take place in the final sintering step.

During the sintering step of the pellets, densification strains are expected to arise, due to the differences in shrinkages of both layers. At the elevated sintering temperature, typically larger than half the homologous temperature, however, creep processes take place [38]. Creep can be described by several processes of mass transport, Nabarro and Herring derived steady state equations for mass transport by lattice diffusion [39]. Another model, by Coble, describes transport along grain boundaries [40,41]. For α-alumina the total creep rate is given through the sum of Nabarro-Herring type and Coble type of creep, according to

$$\dot{\varepsilon} = \frac{\lambda \Omega \sigma}{2\pi k T r^2}\left\{ D_l + \frac{\delta D_{gb}}{r} \right\} \tag{3.6}$$

Here Ω is the atomic volume, σ is the stress in the specimen, r is the grain size, λ is a factor dependent upon the shape of the grains, D_l and D_{gb} are the lattice and grain boundary diffusivities and δ is the effective grain boundary width. The creep rate is proportional to the stress in the specimen. The diffusivities in equation 3.6 have temperature dependencies according to [42]

$$\begin{aligned} D_l &= C_l \exp\left(\frac{-Q_l}{RT}\right) \\ \delta D_{gb} &= C_{gb} \exp\left(\frac{-Q_{gb}}{RT}\right) \end{aligned} \tag{3.7}$$

Here Q_l and Q_{gb} are the activation energies for lattice diffusion and grain boundary diffusion respectively. The creep rate is calculated using the values listed in table 3.3 and plotted in figure 3.5 as a function of temperature and stress in the specimen.

table 3.3: creep rate parameters

parameter		constant	activation energy
lattice diffusion	D_l	$2.8\ 10^{-3}\ m^2s^{-1}$	477 kJ mol^{-1}
boundary diffusion	δD_{gb}	$8.6\ 10^{-10}\ m^3s^{-1}$	419 kJ mol^{-1}
atomic volume	Ω	$4.25\ 10^{-29}\ m^3$	
particle size	r	$10.0\ 10^{-6}$ m	

In the contour plot, figure 3.5, the creep rate is plotted as a function of sintering temperature and stress. At 1600°C, the sintering temperature, the creep rate ranges between ~0.006-0.02% s^{-1} for internal stresses in the range of 10-50 MPa.

Due to creep phenomena in the pellet, evolving stresses will relax, provided that the sintering time and temperature are large enough. Consequently,

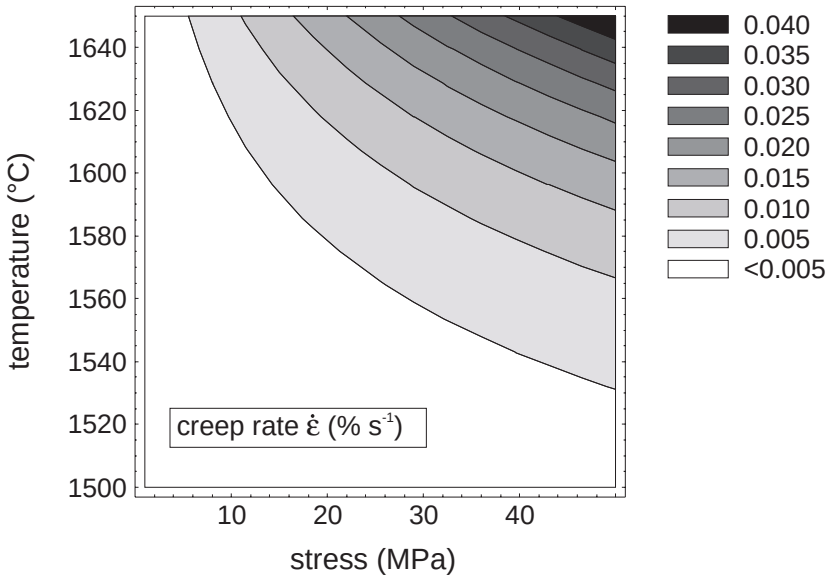

figuur 3.5: *Creep rate in α-alumina as a function of temperature and applied stress, calculated according to equations 3.6 and 3.7.*

differences in shrinkage for the specimen induce stresses, which are assumed to relax through creep processes during the sintering process.

3.2.2 Thermal expansion misfit

During the sintering step in the processing of the pellets, the pellets are heated to the final sintering temperature. Upon heating they will expand due to thermal expansion of the material [43]. This effect may be seen in figure 3.3 where the curves at lower temperatures, before densification starts, take on positive expansion values. The linear expansion coefficients of α-alumina as well as ZrO_2 are listed in table 3.4.

table 3.4: thermal linear expansion coefficients [44]

material	α (10^{-6} K^{-1})
α-alumina	8.2
ZrO_2	10.0

The thermal linear expansion coefficient of the two-phase material can be calculated according to several methods. If the material is anisotropic, for example if the two phases of the composite are lamellar in the material, then the expansion coefficient is taken as the average of both constituents, depending on the direction of the lamellae. If the lamellae are parallel to the slab, then the aggregate thermal expansion coefficient is determined as

$$\alpha_{agg} = f_1\alpha_1 + f_2\alpha_2 \tag{3.8}$$

Here f_i are the volumetric fractions of both phases and α_i are the thermal linear expansion coefficients of both phases. When the lamellae are perpendicular to the slab, the aggregate thermal expansion coefficient is determined as

$$\frac{1}{\alpha_{agg}} = \frac{f_1}{\alpha_1} + \frac{f_2}{\alpha_2} \tag{3.9}$$

If the second phase is dispersed randomly in the matrix, then the aggregate thermal expansion coefficient can be determined from the stress fields arising around the inclusions from the different thermal expansion coefficients of the phases. Assuming that these microstresses are purely hydrostatic, delivers an expression for the total stress state in the material. The summation of all the

stresses over a volume is zero, delivering a value for the aggregate thermal expansion coefficient [45]

$$\alpha_{agg} = \frac{\frac{\alpha_1 K_1 f_1}{\rho_1} + \frac{\alpha_2 K_2 f_2}{\rho_2}}{\frac{K_1 f_1}{\rho_1} + \frac{K_2 f_2}{\rho_2}} \qquad (3.10)$$

Here K_i are the bulk moduli and ρ_i are the densities of both phases. The dependence of the expansion coefficient in the three different approaches on the volume fraction of the α-alumina is depicted in figure 3.6.

From the graph it is seen that the aggregate thermal expansion coefficient is comparable for the first two approaches. Deviating values, however, are found for the isotropic approach. The value for the aggregate thermal expansion coefficient is taken from the isotropic approach, since the second phase in the powder compacts is assumed to be randomly dispersed in the α-alumina matrix. In the thermal stress calculations, a value for the aggregate thermal expansion of α=8.5 10^{-6} K^{-1} is used. This value is obviously comparable to the value for the α-alumina matrix, since the influence of the ZrO_2 on the average value is little. If the temperature difference is large, however, significant strains may arise from the difference in thermal

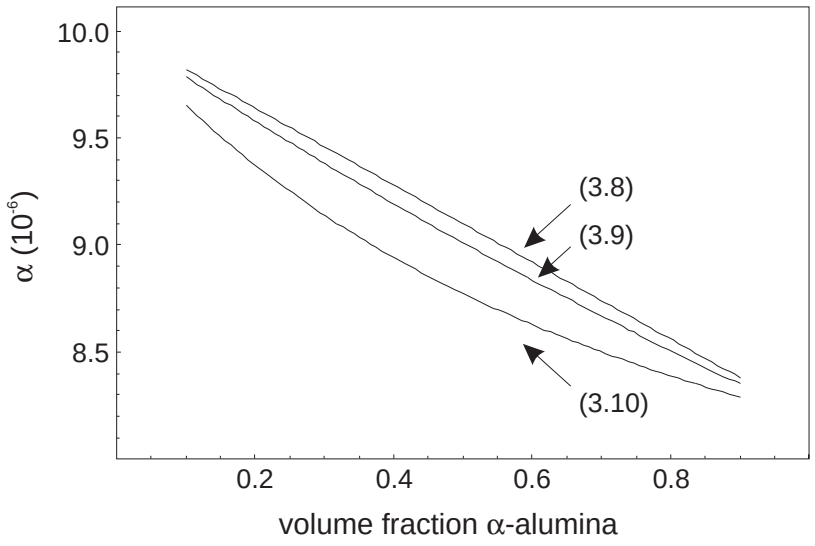

figure 3.6: *Calculation of the thermal linear expansion coefficient of the two-phase material.*

expansions of both the α-alumina matrix and the two-phase material. As already elaborated for the differences in densification, any stresses induced by the differences in thermal expansion upon heating are supposed to be relaxed by creep phenomena during the temperature hold. If the temperature falls below a critical value for creep processes, stress relaxation by creep phenomena will no longer occur, leaving stresses induced by thermal strains in the specimen upon cooling to room temperature.

3.2.3 Finite element calculations

Residual stresses in the pellets induced by differences in thermal expansion coefficients upon cooling, may reach critical values and cause the specimen to fail in the sinter bonding process. If the stresses in the specimen are not large enough to fracture the specimen, they may still influence the mechanical performance of the specimen in a negative or a positive way, depending upon the sign and magnitude of the stresses induced. As an example, the tailoring of the residual stress state in tempered glass by choosing an appropriate cooling rate is considered. Tailoring the thermal treatment will result in a residual stress profile over a cross section of the plate which, depending on the cooling rate, may be compressive or tensile at the surface. Compressive residual stresses at the surface of the glass plate toughens the plate, an effect which is used in the production of safety glass. On the other hand, when stresses at the surface are tensile, microcracks may develop more easily at the surface and failure of the specimen occurs more easily, less fracture energy is required for macrocracks to propagate.

Residual stresses evolving in the pellets upon cooling of the specimen are ascribed fully to a difference in thermal expansion coefficients of both layers [46]. The temperature field in the specimen before cooling is assumed to be homogeneous. Upon cooling the temperature field is assumed to be also homogeneous. This assumption is justified by adjusting the cooling rate of the specimen. Care is taken not to introduce any temperature gradients in the specimen which will cause a non-uniform shrinkage within the specimen locally.

An estimate of the residual stresses induced in the layer as a result of the thermal expansion misfit may be calculated according to [47]

$$\sigma_l = \sigma_T \left[\frac{m^4 + m n_e}{n_e^2 + 2 m n_e (2m^2 + 3m + 2) + m^4} \right] \tag{3.11}$$

Here m,n_e and σ_T are defined through

$$m = \frac{h_l}{h_s} \qquad \sigma_T = \frac{E_l}{1-\nu_l}\int_{T_r}^{T_C} \Delta\alpha dT$$
$$\text{and} \quad n_e = \left(\frac{E_l}{1-\nu_l}\right)\left(\frac{1-\nu_s}{E_s}\right) \tag{3.12}$$

with h_l and h_s the thickness of the layer and substrate, respectively. E_i and ν_i represent Young's modulus and Poisson's ratio of layer and substrate, $\Delta\alpha$ is the difference in thermal expansion coefficient, T_C is the curing temperature and T_R is room temperature. For various temperature differences the expected average stress, according to equation 3.11, is plotted in figure 3.7 as a function of layer thickness h_l for a substrate thickness of 5 10^{-3} m.

The curves indicate that the thermally induced misfit stress in the layer, in this case the two-phase ceramic, is in tension. The average stress induced is, for the 1500°C temperature difference and a layer thickness of 5 10^{-3} m, about 30 MPa. An indication for the maximum tensile stress in the two-phase layer is derived using equation 3.12 [48].

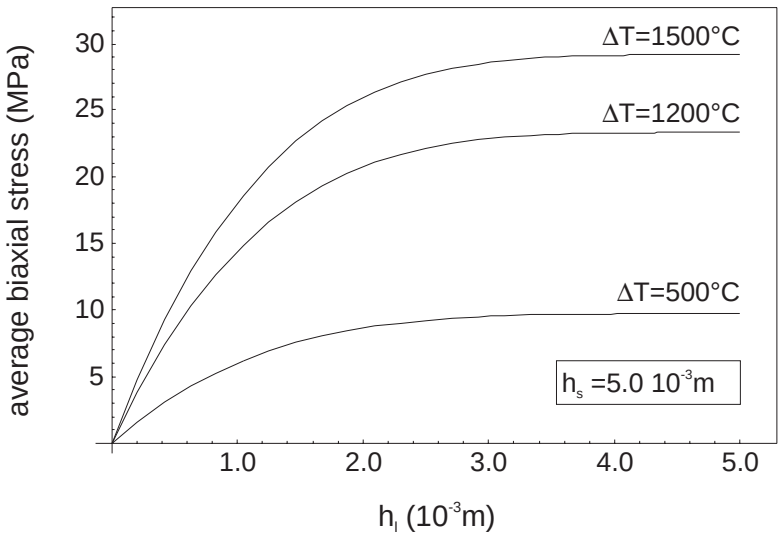

figure 3.7: *Calculation of the average biaxial stress in the two-phase layer as a function of sintering temperature and thickness of the layer.*

$$\sigma^{max} = \sigma_T \left[\frac{m^2 n_e (4m+3)+1}{m^4 n_e^2 + 2mn_e(2m^2+3m+2)+1} \right] \qquad (3.13)$$

where m and n are defined as in equations 3.12. From equation 3.13, a maximum tensile stress, which occurs at the interface, can be derived for the geometry of the composite ceramic and the curing temperature used. The value for the expected maximum tensile stress is indicated in table 3.5.

table 3.5: calculated σ_{max}

T_C (°C)	σ_{max} (MPa)
1600	122
1400	107

The values derived exceed the expected average stress in the layer, figure 3.8. This is expected since the specimen is in maximum tension at the interface and the stress state makes a transition, due to the bending moment, from tension to compression at the top surface. The value for 1400°C is presented, since stress relaxations through creep processes are assumed to be inhibited at this temperature.

The overall stress state throughout the specimen may be determined from finite elements calculations [49]. To perform finite element calculations the specimen are divided in small segments, called elements. These elements are interconnected at joints, called nodes. The macroscopic displacement of the specimen, imposed by thermal expansion of the specimen, is locally approximated by a polynomial function in the elements. In this case the polynomial functions are derived by a minimisation of the elastic energy in every element. This will cause the elements to alter in geometry. The total volume is made up of the elements, therefore, minimisation of the total elastic energy delivers coefficients for the polynomials describing the distortion of each element. From these strains the stresses may be calculated using Hooke's law.

Using the linear thermal expansion coefficients, Young's modulus and Poisson's ratio, residual stress fields are calculated, using isotropic linear elasticity theory, for the specimen geometry used in the sintering processes. The calculations were performed in collaboration with W. Kranendonk, Hoogovens Research Laboratorium. The program used for the finite element calculations is ANSYS5.1. The results of the calculations are displayed in

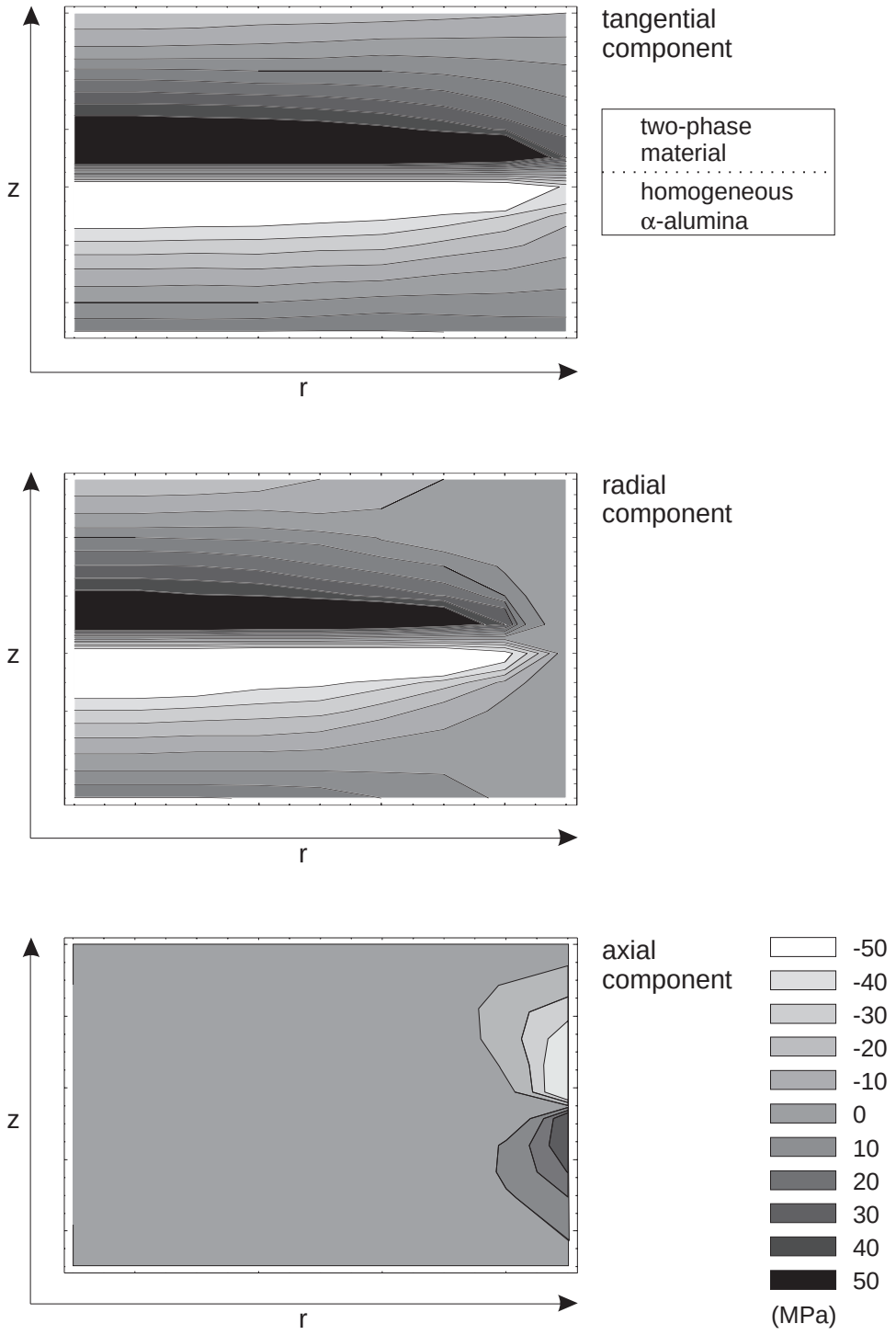

figure 3.8: *Calculations of the residual stress components in the pellets. The stresses calculated are induced by a misfit in thermal expansion coefficient for the homogeneous and heterogeneous materials.*

figure 3.8. In these contour plots, the axial, radial and tangential stress components, $\sigma_{i,j,k}$, are plotted for the cross section of a half plane.

From the plots it is seen that for the radial and tangential stress components, the sign of the stress reverses over the interface. The homogeneous layer is in compression in the vicinity of the interface. Tensile stresses are calculated for the interfacial area in the two-phase material. This is in agreement with the larger thermal expansion coefficient of the two-phase material, upon cooling the two-phase material will shrink more than the homogeneous material, inducing tensile stresses since the layer is constrained by the homogeneous layer.

The radial stress component decreases in magnitude to zero upon approaching the free interface, as expected since radial stresses can not be sustained by a free surface. The tangential stress component, however, is not constrained by the free surface boundary condition. From the calculations a stress gradient is seen at the free surface over the interface. Overall, at remote positions of the free surface, the magnitude and sign of the radial and tangential stress components are equivalent, as expected from elasticity for a axisymmetric stress distribution in a material with no body forces and no holes [50].

The axial stress component reaches a significant value only in the vicinity of the free surface. Throughout the specimen the axial residual stress component is typically zero. At the free edge the axial stresses increase in the vicinity of the interface.

Discussion

The magnitude of the stresses over the interface, as calculated by the finite elements method, range typically from ~80 to –80 MPa. If the stress intensity factor for microcracks in the material approaches the critical stress intensity factor, $K_{Ic} \cong 4\ MPa\sqrt{m}$ for α-alumina, the specimen will fail over the interface, resulting in debonding of both layers. Therefore, care should be taken in tailoring the processing parameters and specimen geometry to maintain the evolving stresses below the critical value. The stress intensity factor is governed through [51]

$$K_I = \sigma\sqrt{\pi a} \qquad (3.14)$$

For microcracks ~5 μm in size, the critical stress is found to be equal to ~1GPa. Ceramics are typically 10-20 times stronger in compression than in tension [52]. The addition of ZrO_2 as a second phase in an α-alumina matrix may increase the fracture toughness from 4 $MPa\sqrt{m}$ for the α-alumina to

22 D.S. Wilkinson and M.F. Ashby, Sci. Sintering, **10**, (1978), 67.

23 E. Artz, M.F. Ashby and K.E. Easterling, Metall.Trans., **14A**, (1983), 211.

24 A.S. Helle, K.E. Easterling and M.F. Asby, Acta Metall., **12**, (1985), 2163.

25 S.H. Hillmann and R.M. Germann, J. Mater. Sci., **27**, (1992), 2641

26 E. Dörre and H. Hübner, Alumina, Springer-Verlag, Berlin, (1984), 52.

27 Y. Matsumoto, K. Hirota and O. Yamaguchi, J. Am. Ceram. Soc., **76**, (1993), 2677.

28 L.C. Stearns and M.P. Harmer, J. Am. Ceram. Soc., **79**, (1996), 3013.

29 H. Harada and T. Sakuma, J. Ceram. Soc. Jap., **99**, (1991), 132.

30 N. Claussen, R.L Cox and J.S. Wallace, J. Am. Ceram. Soc., **65**, (1982), 190.

31 A.G. Evans and A.H. Heuer, J.Am. Ceram. Soc., **63**, (1980), 241.

32 R.M. McMeeking and A.G. Evans, J. Am. Ceram. Soc., **65**, (1982), 242.

33 E. Ryshkewitch, Oxide Ceramics, Academic Press, New York, (1960), 350.

34 D.A. Porter and K.E. Easterling, Phase transformations in metals and alloys, Chapman and Hall, London, (1981), 383.

35 W.Y. Yan, G. Reisner and F.D. Fischer, Acta Mater., **45**, (1997),1969.

36 L. Ruiz and M. J. Readey, J. Am. Ceram. Soc., **79**, (1996), 2331.

37 P. van den Berg, PhD thesis, University of Eindhoven, (1992), 18.

38 W.D. Callister, Materials science and engineering, John Wiley and Sons, New York, (1985), 227.

39 C. Herring, J. Appl. Phys., **21**, (1950), 437.

40 R.L. Coble, J. Appl. Phys., **34**, (1963), 1679.

41 P.M. Hazzledine and J.H. Scheibel, Acta. Metall. Mater, **41**, (1993), 1253.

42 E. Dörre and H. Hübner, Alumina, Springer-Verlag, Berlin, (1984), 156.

43 R.Pampuch, Constitution and properties of ceramic materials, Elsevier, Amsterdam, (1990), 249.

44 G.V. Samsonov, The oxide handbook, Plenum, New York, (1973), 125.

45 W.D. Kingery, H.K. Bowen and D.R. Uhlmann, Introduction to ceramics, John Wiley and Sons, New York, (1976), 604.

46 T. Chartier, D. Merle and J.L. Besson, J. Eur. Ceram. Soc., **15**, (1995), 101.

47 P.Z. Cai, D.J. Green and G.L. Messing, J. Am. Ceram. Soc., **80**, (1997), 1929.

48 P.Z. Cai, D.J. Green and G.L. Messing, J. Am. Ceram. Soc., **80**, (1997), 1940.

49 M.J. Fagan, Finite element analysis, Longman Scientific and technical, Singapore, (1992)

50 Timoshenko, Theory of Elasticity, McGraw-Hill, New York, (1951), 58.

51 D. Broek, Elementary Engineering and Fracture Mechanics, Noordhof International Publishing, Leyden, (1974), 10.

52 Anon., Engineered Materials Handbook, vol. 4; Ceramics and Glasses, ASM international, (1991), 585.

53 Y. Matsumoto, K. Hirota and O. Yamaguchi, J. Am. Ceram. Soc., **76**, (1993), 2677.

4 STRUCTURAL EFFECTS

Introduction

Changes in morphology during the sintering process of engineering ceramics determine the eventual material properties to a large extent. This holds for the powder compacts as well as for the sol-gel derived thin ceramic layers. In this chapter, high resolution low voltage scanning electron microscopy will be used as a tool to study the structural changes of the materials as a result of the sintering process.

For the powder compacts, i.e. the composite pellet materials, the bonding between the dissimilar layers will be studied. Since the aim of the diffusion bond process is to attach separate layers to one another, the quality of the interface is of great importance. Consequently, the evolution in grain size and the influence of the second phase on the eventual grain sizes will be studied.

In the second part, the impact of the various curing processes on the sol-gel derived layers will be studied. For several precursors, the influence of furnace curing as well as laser curing will be considered. Points of focus are the evolution of grain sizes, the decrease in porosity and debonding between layer and substrate as a result of the curing process. Especially the sol-gel derived layers of TiO_2 are of interest, which will be studied in chapter 5 in more detail.

4.1 Experimental procedures

4.1.1 Sample preparation

The microscopes used to produce the micrographs in this chapter are a Philips XL30-FEG SEM and a Philips XL30S-FEG SEM. Both microscopes produce primary electrons using a field emission gun. The latter is equipped with an especially designed lens, where the specimen is placed at the location where the magnetic field is the largest. To study features of the materials in a scanning electron microscope the specimen have to be prepared. In the following, the procedures used to prepare the specimen for optimal imaging conditions in the scanning electron microscopes, are discussed.

Pellets

Scanning electron microscopy is used to examine several aspects of the two layer ceramic pellets. Topics of interest are:

- bonding between layers
- location of zirconia particles in the two-phase ceramic material
- evolution of grain and pore sizes

Since all these features are studied best in cross section, the specimen are sectioned using a diamond precision saw. After sectioning, the specimen are lapped and polished using diamond slurries, with particle sizes decreasing from 30 μm to 6 μm, on flat solid plates. The final polishing step is performed on a polishing cloth, using a slurry with 0.06 μm particles. The polishing media in the slurry is a mix of amorphous silica and iron oxide particles. The samples are polished to a high degree of flatness. After polishing, the samples are thermally etched in order to reveal the microstructure. Etching takes place in a furnace, operating at 1300°C, for 45 minutes in air. During the etching process, material diffuses from the grain boundaries to the bulk of the grains, hereby reducing grain boundary energy [1]. After etching, the material is gradually cooled down in air to room temperature. The samples are now ready to be studied in the scanning electron microscope.

Sol-gel layers

After drying and the heat treatment of the sol-gel layers, they are studied using scanning electron microscopy. The main topics of interest are:

- the dimensions of the nano-sized particles
- grain growth
- debonding of the layer
- cracks in the layer

Since some of these topics can be studied in top-view, the samples do not require any preparation. The other features, debonding of the layer and cracks in the layer, require cross sectional examination. Simple cutting using a precision saw is not an option, since this will distort the layers to a large extent. A cross section of the samples is therefore obtained by cleaving the

samples. First a pre-crack is induced in the non-coated surface of the substrate. This pre-crack is extended through the substrate and the layer by bending, leaving a cross sectioned sample. This procedure results in very clean cross sectional specimens which can be studied directly in the microscope.

4.1.2 Low-voltage high resolution SEM

As described in section 2.3, charging of non-conducting samples in a scanning electron microscope should be minimised, since this will decrease the obtained image quality drastically. Charging can be prevented by balancing the incoming and outgoing current, or by sputtering a conducting layer onto the surface of the ceramic. This sputtered layer however will decrease the resolution since features present in the micrograph do belong to the conducting layer and are not necessarily present in the underlying ceramic itself.

Using the high voltage setting to balance the incoming and outgoing current should theoretically deliver adequate results. In the case of the bulk ceramic materials the optimum settings for the microscopes are found to be 2.0 kV and the smallest beam current. By lowering the incoming current the charging effects may be minimised.

The settings for the sol-gel thin ceramic layers are less critical since, due to conducting compounds present in the sol, the layers do not easily charge in the scanning electron microscope. The conducting properties of the layer do however depend very much on the sol used. A severe problem of the examination of the layers using SEM is that the image tend to darken when they are studied at very high magnifications (of the order of ~10^5X). This effect may be a result of the disintegration of carbon compounds in the layer. To circumvent these negative effects, a wide range of settings is used. Variations in accelerating voltage, spot size and integration methods are used to achieve resolutions down to ~10 nm.

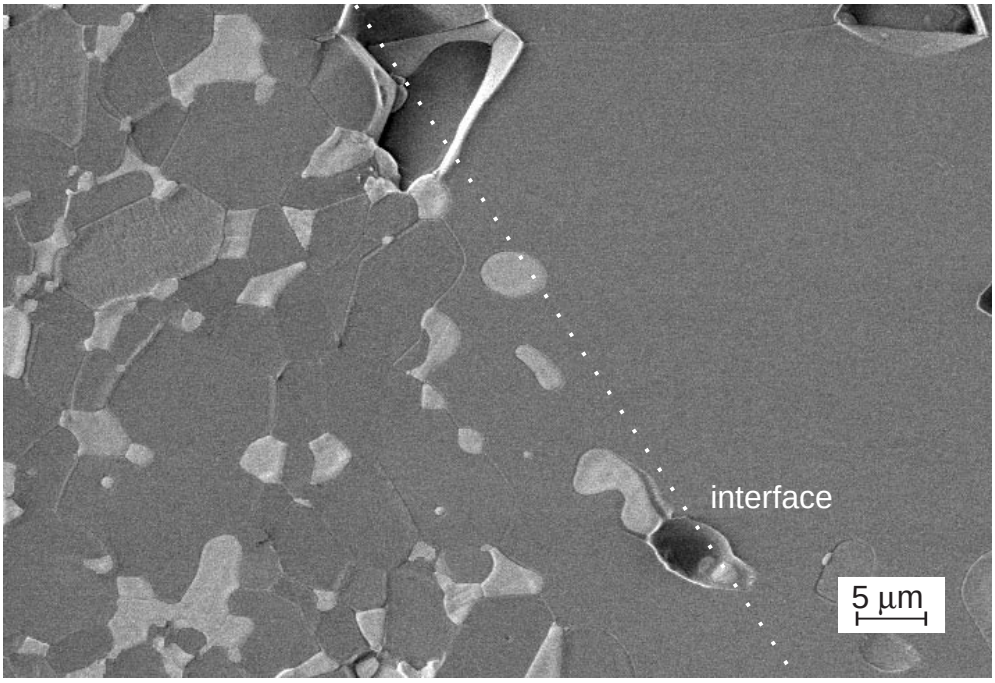

figure 4.1: *Pellet derived through separately processing of the layers.*

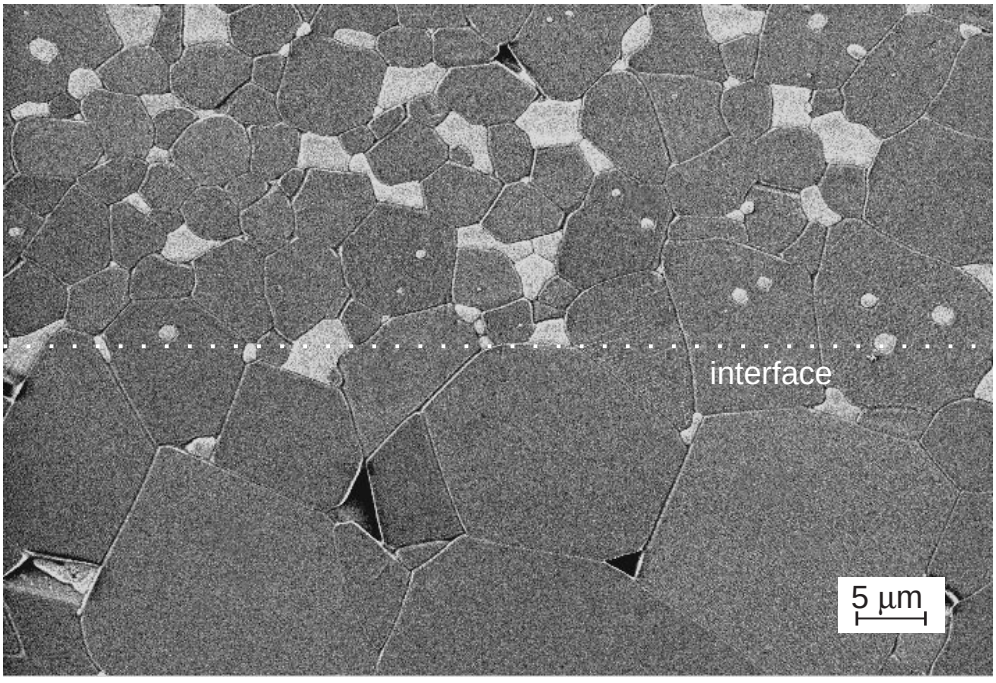

figure 4.2: *Pellet produced by combined processing of separate layers.*

4.2 Morphology of the sinter bonded pellets

Introduction

The morphology of the sinter bonded ceramic pellets is of influence on the eventual mechanical properties of the material. It is therefore important that insight is gained in the microstructure of the pellets. Of special interest are the grain size developments in both layers, since they determine the strength of the material, and the role of the added zirconia in grain size evolutions. Furthermore, the bonding between the separate layers is studied.

4.2.1 Bonding between layers

To study the bonding between the dissimilar ceramic layers, several samples are examined in the scanning electron microscope. Cross sectional surfaces are obtained by cutting the specimens and subsequently by polishing to a low surface roughness. To study the differences in processing of the composite ceramics derived using alternate routes, both classes of specimens are investigated, the combined pressed and sintered as well as the pre-pressed and pre-sintered specimens.

As a typical example, a micrograph of a separately processed sample is depicted in figure 4.1. The interfacial area between the two layers is distinctly visible. It is apparent that there are regions where the interface is fully joined. This in contrast to other regions where cracks and voids over the interface are observed.

In contrast to the separately processed specimens, the combined processed specimen depicted in figure 4.2, exhibit full bonding over the interface. There are no cracks visible between the homogeneous and the two-phase material layers and there are no voids present. The zirconia particles in the two-phase material, identifiable as the bright particles in the micrographs, are located at the grain boundaries in the alumina matrix and at the intersections of those grain boundaries. However, there are also zirconia particles visible which are embedded in relatively large alumina particles. These particles were initially located at grain boundaries and, in the process of grain growth, they did not migrate along with the grain boundary. As a consequence, they remain located within the alumina grains.

4.2.2 *Grain size development*

During the sintering process, the centers of interconnecting grains tend to move towards each other as a result of atoms diffusing away from the neck region. The spacing between the centers is hereby decreased. Atoms do not only diffuse along the grain boundary, they may also leave grain 1 and be accomodated by grain 2, a migration process which will cause grain 1 to shrink and grain 2 to grow. This diffusion of atoms can be so severe that the grain boundary moves through the grains and, eventually, the two separate grains are left as one grain. The larger grains tend to absorb the smaller grains, hereby decreasing the total surface of the grains together. From the surface energy point of view it is thus advantageous for grains to grow.

The densification of the material, assuming that the main densification mechanism in the sintering process is grain boundary diffusion, is however inhibited by grain growth. This can be seen from the fact that the amount of grain boundaries in the material is approximately inversely proportional to the grain size in the material.

In the micrographs of the etched samples, the grain boundaries are very distinct features. Applying a method which is known as the linear intercept method, readily delivers values for the average grain size in the samples. The linear intercept method makes use of a line of known length l drawn over the surface of the samples. Every intersection of this line with a grain boundary is counted. When sufficient intersections are determined, the average grain radius R is a direct measure from the number of intersections per total line length [2,3]

$$R = \frac{3L}{4N} \tag{4.1}$$

Here L is the total line length and N the total numbers of intersections. If the systematic error, that is the error being made by the fact that the lines start and end within a grain, $\delta R/R$, is approximated by

$$\frac{\delta R}{R} \cong \sqrt{\frac{20.25}{N^2}} \tag{4.2}$$

about 450 intersections has to be counted when a systematic accuracy of ~1% is desired.

In the composite ceramic materials, the average grain radii are determined using the linear intercept method for both layers of the samples. A total of ~450 intersections were determined for the different materials.

In the homogeneous α-alumina material, the determined average grain radius corresponds to the grain radius of the alumina particles. In the two-phase ceramic material, the determined average grain radius is, however, a measure for the grain radius of both the added second phase and the alumina matrix. Since a comparison between both grain sizes in the homogeneous and the heterogeneous material of the alumina matrix is required, the influence of the second phase on the measured particle radius has to be minimised. This is done by choosing lines which intersect as little second phase particles as possible. The resulting average grain sizes, calculated according to equation 4.1, are listed in table 4.1.

table 4.1: average grain radius

material	average radius (μm)
homogeneous α-alumina	14.4±0.1
2-phase ceramic	3.1±0.1

From the micrographs it is clear that the average grain radius of the alumina grains in the homogeneous material is larger than the alumina grain sizes in the two phase material. The values given in the table for the experimental average grain sizes measured confirm this observation. The grain growth in the alumina matrix is inhibited by the presence of the second phase [4-6].

The influence of the second phase on the grain growth in the alumina matrix may be explained by several physical concepts. A model, known as the topological model, uses the second phase particles as anchoring points for the matrix grain boundaries [7,8]. If the second phase particles are assumed to be rigid and immobile in the matrix, a model can be derived where the alumina matrix grain boundaries are pinned by a distribution of second phase particles. The nodes span the grain boundaries, hereby limiting the maximum matrix grain sizes.

A second model describes the grain size, in contrast to the topological model, in an analytical way. This model is known as the Zener model [9-15]. It applies to a system that contains monosized, insoluble, immobile particles

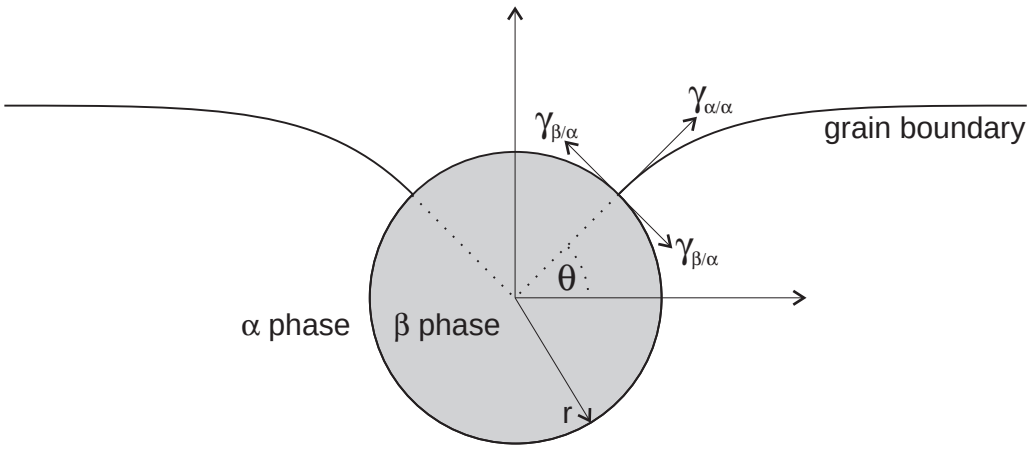

figure 4.3: *Interaction of a grain boundary with a second phase particle, inhibiting grain growth in the matrix.*

and considers the retarding force exerted by these particles on rigid, moving grain boundaries. The force exerted on a boundary by a single particle, F_s, is given as

$$F_s = 2\pi r\gamma_b \cos\theta \sin\theta \tag{4.3}$$

where r is the particle radius, γ_b is the grain boundary energy per unit area and θ is the angle between the grain boundary and the normal to the particle surface at the point of intersection with the particle, as depicted in figure 4.3. Assuming that each particle exerts the maximum force on the boundary, F_m, which occurs for θ=45°, equation 4.3 transforms into

$$F_m = \pi r\gamma_b \tag{4.4}$$

If the particle grain boundary intersections are purely random, the number of particles per unit of grain boundary area are calculated by

$$N_{ba} = N_V d = \frac{fd}{\frac{4}{3}\pi r^3} \tag{4.5}$$

with N_V the number of particles per unit volume, d the particle diameter *(=2r)* and f the particle volume fraction. The total pinning force, F_p, is now the

multiplication of the pinning force per particle, F_m, times the total number of pinning particles, N_{ba}. The grain boundary experiences a driving force for grain boundary migration, F_b, given through by

$$F_b = \frac{2\gamma_b}{R} \tag{4.6}$$

with R equal to the grain boundary radius of curvature, which is assumed to be equal to the grain radius of the matrix. When the retarding force, F_p, equals the grain boundary migration force, grain growth stops. The limiting grain radius, R_L, is solved by equating F_p to F_b

$$R_L = \frac{4r}{3f} \tag{4.7}$$

This equation describes the relation between maximum grain radius in the matrix material and the properties of the second phase added. It is clear that only the particle size of the added second phase and the particle volume fraction are of influence, determining the final limiting grain radius. The sintering temperature does not influence the grain size in the matrix, it does however influence the rate at which the system attains equilibrium.

The second phase powder which is used in the specimens consists of zirconia particles with an average grain radius of ~0.5 μm. The added particle volume fraction is ~20%. Using the second phase properties and equation 4.3, a maximum matrix grain radius may be derived as listed in table 4.2.

table 4.2: matrix grain size

second phase properties	calculated	experimental
r=0.5μm/f=0.20	3.3 μm	3.1 μm

The model describes grain growth in a way that the observed grain size is limited by the expected calculated grain size. Note that the observed grain size is an average grain size and not the maximum grain size. The grain size of the added second phase however is again an average grain size, so that the calculated as well as the observed maximum grain sizes are somewhat larger than the values listed in table 4.2.

4.2.3 Grain growth versus densification

During the sintering process several regimes in the temperature-densification processes can be identified. In each regime a specific process dominates. The processes predominating a regime can, for example, be densification, which may be sub-categorised into the different diffusional regimes. Another dominating process may be grain growth. If the temperature during the sintering process is divided roughly in two regimes, one at high temperatures and one at low temperatures, the processes dominating each regime may be explored in more detail.

At low temperatures grain growth is the dominating process. Supremacy of grain growth over densification processes can arise when one of the following conditions occur [16].

- the activation energy for grain growth is less than for diffusional mechanisms
- the activation energy for both processes are similar, but the diffusional mechanism makes a transition to surface diffusion at low temperatures

In the latter case, the surface diffusion can be considered a grain growth intensive regime, since only grain growth and not densification can occur by diffusion along particle surfaces. At high temperatures densification processes dominate over the grain growth processes [17]. In section 3.1 it was already mentioned that the main densification processes for bulk ceramic powder compacts, having particle sizes in the micrometer range, are grain boundary diffusion and lattice diffusion.

Grain growth can be remedied by the addition of a second phase, as discussed in section 4.2.2. Furthermore, tailoring the pore size distribution in the green product may also deliver higher densification rates and smaller final grain sizes, since the pores can act as grain boundary anchors themselves, limiting grain growth in a similar way as added second phase particles [18,19].

Avoiding grain growth prior to the onset of densification is all the more important because densification rates depend strongly on the inverse of the grain size, to the third power for volume diffusion and fourth power for grain boundary diffusion. Increasing grain sizes will thus decrease densification rates. This can be seen in figure 4.2 where a cross section of a

pellet is depicted. Pores are clearly visible in the homogeneous α-alumina phase, whereas the two-phase material appears to be fully densified. The homogeneous phase material exhibits very large particles relative to the two-phase material, underlining the grain inhibiting and densifying properties of the added second phase in the matrix.

4.2.4 Discussion

Scanning electron microscopy was employed to obtain results on the bonding between the separate layers as well as the grain and pore size evolutions. For both processing routes, separate and simultaneous processing, bonding between the layers is achieved, although in the separately processed layers still some cracks and voids remained over the interface. This difference is ascribed to the fact that in the pre-sinter processing of the separate layers already an evolution in grain sizes and densification has taken place. In the final diffusion bonding process the separate layers are placed in contact with each other. The connecting particles are of relatively large sizes, compared to the connecting particles in the simultaneous process, resulting in lower densification rates according to equation 3.2. Hence, the initial pores are reduced at lower rates, compared to the simultaneous process, and voids may remain at the interface after the final curing process.

The addition of ZrO_2 in the α-alumina matrix results in an inhibition of grain growth in the matrix. This may be explained by the force which the dispersed particles exert on the moving grain boundaries in the matrix. Equating the driving force for grain boundary migration and the retarding force which the dispersed second phase particles exert on the moving grain boundaries, delivers a limited grain size in the matrix. This limitation of the grain size in the matrix enhances the grain boundary diffusion controlled densification of the powder compact, resulting in relative densities which may be larger for the two-phase ceramic than for the homogeneous ceramic.

4.3 Morphology of sol-gel derived thin ceramic layers

Introduction

The sol-gel derived thin ceramics layers are consolidated using two different processes, the furnace curing process and the laser curing process. The differences between the two processes are the area which is cured per unit

time, and the interaction time during which thermal energy is supplied to the ceramic layers. In contrast to the furnace curing process, the laser curing is very localised and the interaction area is determined by the spot size of the laser used. Furthermore, the interaction time in the laser curing process is typically very short, of the order of microseconds. The interaction time in the furnace curing process is typically of the order of an hour.

In this section the impact of the curing process on the morphology of the sol-gel derived layers is studied. Several sol-gel derived layers, which experienced various curing treatments, are considered. Points of focus are the evolution of grain and pore sizes, densification of the layers, and cracking and debonding of the layers.

4.3.1 TiO_2 thin films

This class of thin films examined using HRSEM consists of similar substrate/layer systems. The substrate is fused silica. The layer is made from a tetraethylorthotitanate precursor, $Ti(OC_2H_5)_4$ or TEOTI. This precursor will

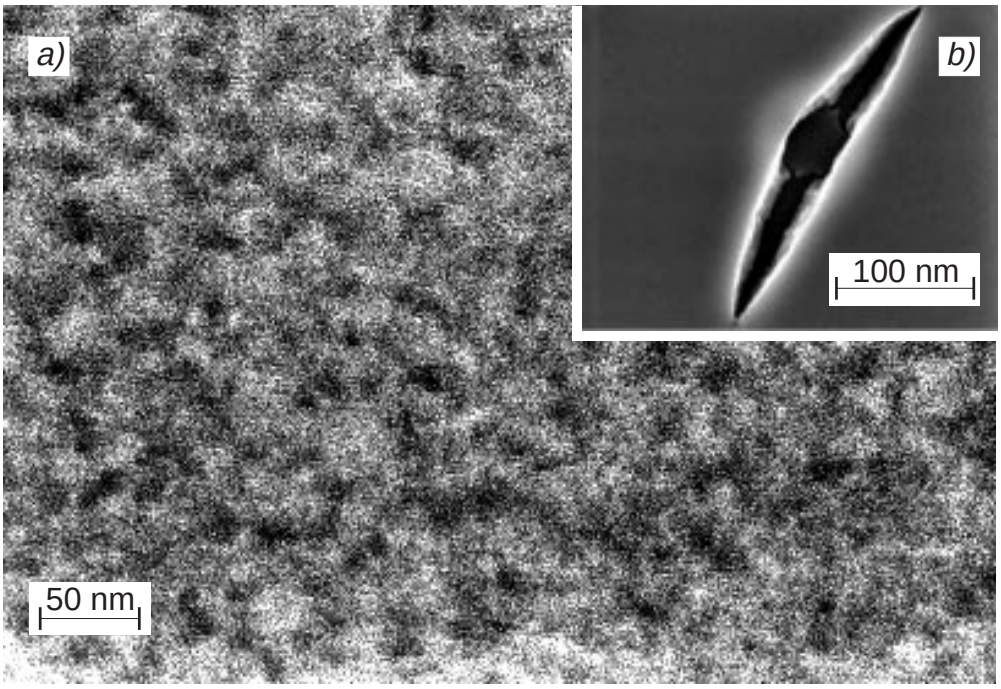

figure 4.4: *Micrograph of a 300°C furnace cured TiO_2 layer.*
a) Morphology of the layer, exhibiting features <10nm.
b) Sub-micron sized cracks appearing throughout the layer, ranging in radius between 50 and 300nm.

result in a layer of TiO_2 after spinning [20]. The expected thickness of the films is of the order of ~200-500 nm. After spinning, the specimens are dried to remove excess liquids, left after spinning, from the layers. A set of specimens is cured using a Nabertherm tube-furnace. The specimens are directly cured in air at temperatures ranging from 300°C to 1200°C.

An alternative way to densify as-spun thin films, is to cure them in a laser treatment, as described in section 2.2. This process consists of radiating the thin films with a 80W CW-CO_2 laser (RS80), using a wavelength of 10.6 μm, the experiments were conducted at CFT-Philips.

Since the area of interest of this class of samples is the thin top layer, the operating settings of the microscope are chosen in such a way, that the secondary electron image is mainly generated by the layer. Blurring of the images due to secondary electrons induced by the substrate can be prevented by adjusting the accelerating voltage of the primary electrons, hereby decreasing the penetration depth of the primary electrons. Doing so will increase the resolution of the images. As a consequence of lowering the accelerating voltage, positive charging of the samples is more likely to occur, especially at higher magnifications. Recording images is therefore performed by scanning at high scan speeds and integrating the images afterwards. Since the primary electron beam, operated at these conditions, does not dwell at the same location at the sample for long times, the charging effects can be suppressed.

Furnace cured TiO_2 layers

In figure 4.4 a micrograph is depicted of a TEOTi sample which is heat treated in the furnace at 300°C for 30 minutes. Figure 4.4.*a* depicts the morphology of the thin layer. There are no grains or particles distinguishable, although overall some sort of texture may be observed, indicating nanopores or very small grains. The transition from amorphous films to the crystalline anatase phase depends on the synthesis conditions of the sol and depending on those conditions crystallisation starts at temperatures in the order of ~300°C [21,22]. Cracking of the layer, as depicted in figure 4.4.*b*, is observed on a global scale. The cracks are sub-micron sized, and are assumed to be formed in the drying process already.

Evolution of stresses during drying of the layers

Upon drying the film, as schematically depicted in figure 4.5, the rate of evaporation of liquid, $\dot{V}_E$, must equal the flux of liquid, J, from the solid porous network to the surface as described by Darcy's law [23]

$$J_{surface} = \frac{-D}{\eta_L}\nabla P = \dot{V}_E \tag{4.8}$$

with D the permeability of the film and η_L the viscosity of the liquid. ∇P is the pressure gradient in the liquid. This gradient causes the liquid-vapor interface to remain at the surface of the drying film and to compress the network in the film. The liquid covering the solid phase is in tension. The tension is balanced by compressive stresses which tend to suck the network under the surface of the liquid. The more compliant the network, the less effort has to be expended to keep it submerged. From equation 4.8 it is seen that the pressure gradient ∇P in the liquid phase of the drying film is directly correlated to the permeability D of the network and the rate of evaporation $\dot{V}_E$. An estimation for the permeability of the porous network can be derived by assuming the pores to be a bundle of straight parallel capillaries of uniform diameter $\bar{\delta}$, with n capillaries per unit area. According to the Hagen-Poiseuille law [24], the flow per unit area will be

$$J = \frac{-n\pi\bar{\delta}^4}{128\eta_L}\nabla P \tag{4.9}$$

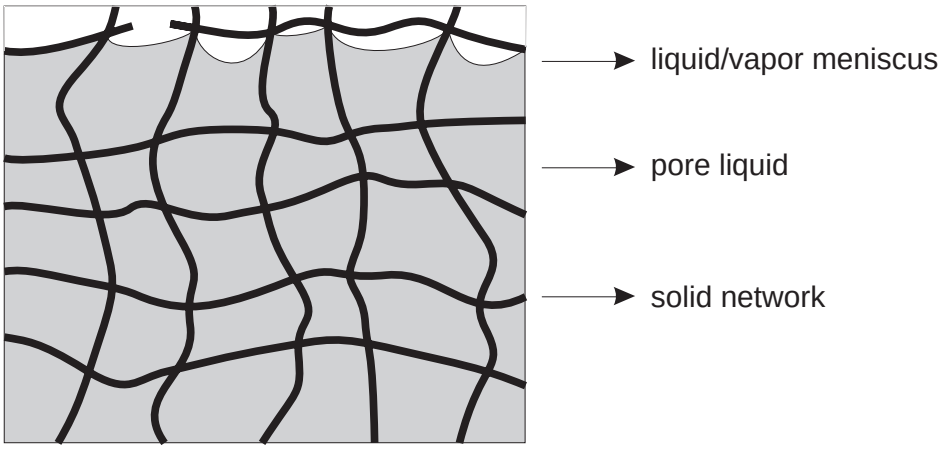

figure 4.5: *Drying of the solid network by evaporation of volatiles.*

From equations 4.8 and 4.9 an expression for the permeability of the solid network is derived as

$$D = \frac{n\pi}{128}\bar{\delta}^4 \tag{4.10}$$

It is seen that the permeability depends strongly upon the average capillary size, hence upon the pore size in the solid network. Because of the very small pore sizes of the solid network in the drying film, the permeability is relatively low with respect to ordinary bulk ceramics. As a consequence of this low permeability, very steep pressure gradients may arise, even for modest drying rates. The steeper ∇P, the greater the difference in shrinkage rate between the exterior and the interior of the network, and the more likely the film is to fracture. From the pressure gradient, a relation for the maximum tensile stress, which occurs at the surface of the film, can be approximated. This relation also includes the thickness of the film L.

$$\sigma_x \approx \frac{L\eta_L \dot{V}_E}{3D} \tag{4.11}$$

From this relation, high tensile stresses are expected for thick films, or when drying at high evaporation rates, $\dot{V}_E$, and for networks which have low permeability. Upon drying of the layer the average pore diameter in the layer will decrease. This decreasing pore size distribution will result in, according to equation 4.10, a decrease in permeability of the layer, hence increasing the stress state in the layer. The stress in the layer is however not the factor governing crack initiation and propagation. For cracks to propagate it is required that the critical stress intensity factor, K_{Ic}, is exceeded.

$$K_I = \sigma_x \sqrt{\pi a} \geq K_{Ic} \tag{4.12}$$

with σ_x the stress state in the layer as defined by equation 4.11 and a the radius of an existing crack or flaw in the material. From equation 4.11 it is seen that the stress state in the layer is depending on $\dot{V}_E$. Increasing the evaporation rate will result in an increase of the stress intensity factor of the layer due to the tensile stress increase. On the other hand, as the evaporation rate increases, the crack pattern in the layer will become more scattered, resulting in an effectively smaller average flaw size a and, consequently, in a lower stress intensity factor.

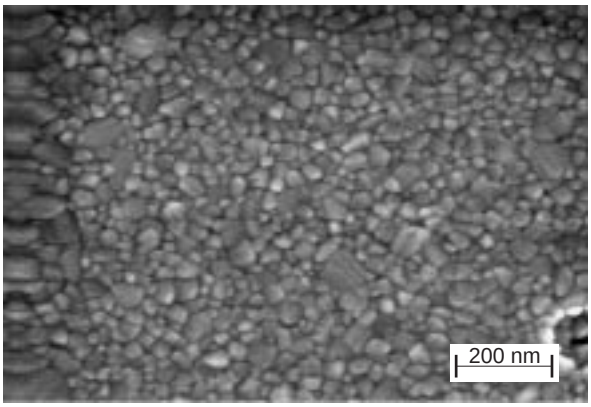

figure 4.6: *Micrograph of a 700°C furnace cured TiO_2 layer. In contrast to the 300°C specimen, grain growth has taken place in the layer. The average grain radius determined is r=24.2 nm.*

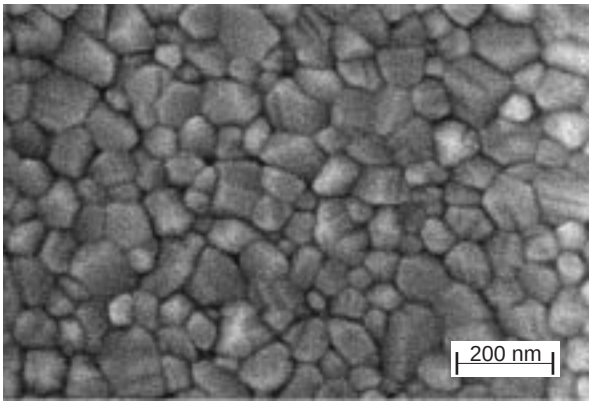

figure 4.7: *Micrograph of a 900°C furnace cured TiO_2 layer. Further evolution in grain sizes is observed. The average grain radius determined is r=50.1 nm.*

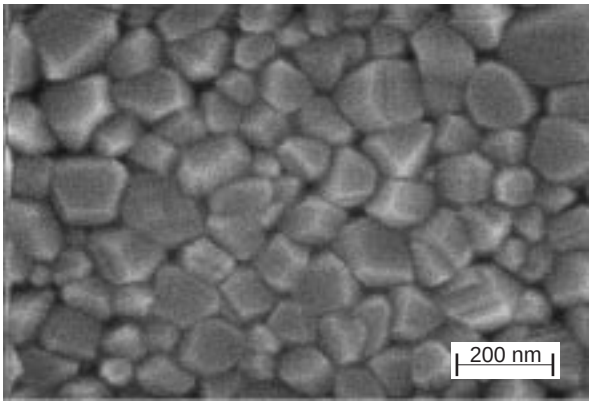

figure 4.8: *Micrograph of a 1200°C furnace cured TiO_2 layer, with average grain radius r=89.7nm.*

A micrograph of a sample furnace treated at 700°C is depicted in figure 4.6. This sample is similar to the one depicted in figure 4.4 for the 300°C sample, the only difference is the heat treatment it has experienced. The initial film properties, film thickness, sub-micron cracks, grain and pore size

distributions are however similar. The sample is heat treated at 700°C for 30 minutes. From the micrograph it is apparent that an evolution in grain size has taken place. In figure 4.4 no separate grains are distinguishable whereas in figure 4.6 grains are clearly visible. A second remarkable feature is that the observed sub-micron cracks in the 300°C heat treated sample are less frequently observed in the 700°C heat treated sample. Increasing the curing temperature for the samples to 900°C, results in a further evolution in grain growth for the TiO_2 layers. In figure 4.7 a micrograph is depicted for a 900°C sample. Micrograph 4.8, in which the 1200°C sample is depicted, visualises the further grain growth when the samples are subjected to 1200°C for 30 minutes. The radius of the grains are of the order of ~90 nm. Sub-micron cracks in the layer, occurring for samples which have experienced a heat treatment at lower temperatures, disappeared.

Grain size evolution

The average grain sizes in the layers cured at the various temperatures are measured using the linear intercept method as described in section 4.2. The results of the measurements are listed in table 4.3.

table 4.3: grain size TiO_2

heat treatment (°C) 30min. hold	avg. grain radius (nm)
300	-/-
700	24.2±0.1
900	50.1±0.1
1200	89.7±0.1

Since the resolution of the micrograph of the 300°C furnace cured sample is too low and the size of the grains, if any, is too small, an average grain size can not be determined. The grain radius in this sample is assumed to be around 5 nm, which is a value found, using low-frequency Raman scattering, for TiO_2 thin films prepared using sol-gel synthesis [25].

In the next part, the evolution in grain size with increasing heat treatment temperature is discussed. Assuming that the mean radius of curvature of the grain boundaries is proportional to the mean grain radius $\bar{R}$, the mean driving force for grain growth will be, according to equation 4.6,

proportional to $2\gamma/\bar{R}$. The average velocity of a boundary experiencing such a driving force is given through

$$\bar{v} = M\frac{2\gamma}{\bar{R}} \tag{4.13}$$

Here M is the mobility of the grain boundary. This mobility is directly correlated to the grain boundary migration activation energy [26].

In figure 4.9 the free energy of an atom, moving from one grain to an other, is depicted. In this figure, ΔG^{a} is the thermal activation energy for an atom to leave grain 1, lowering its free energy with an amount of ΔG when accommodated in grain 2. The number of actual atoms moving from grain 1 to grain 2 is a function of this thermal activation energy and given by equation 4.14

$$J_{1\to 2} \propto \exp\left(\frac{-\Delta G^{a}}{RT}\right) \tag{4.14}$$

The net flux of atoms moving from grain 1 to grain 2 is the difference in effective flux of atoms moving from grain 1 to grain 2 and vice versa. When

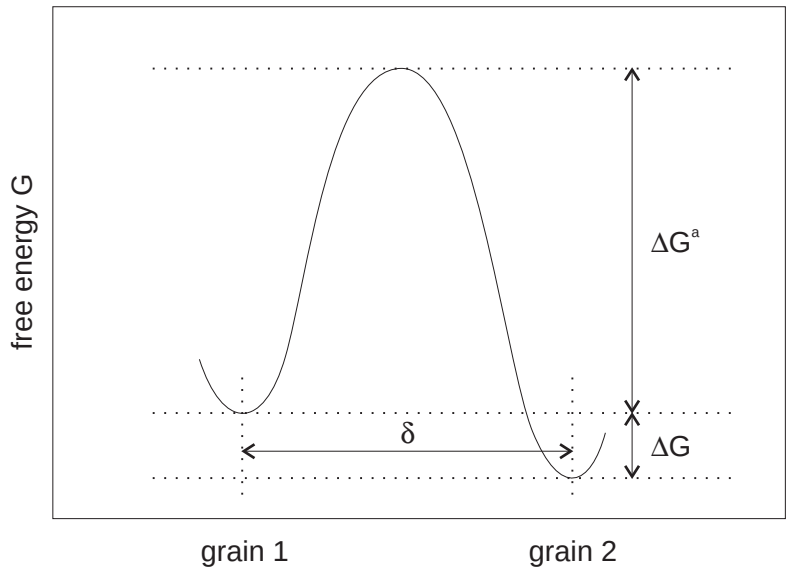

figure 4.9: *Free energy change for atoms moving from grain 1 to grain 2 by thermal activation.*

ΔG=0, this net flux will be zero, there are no atoms moving effectively from grain 1 to grain 2, in any other case the net flux is given by

$$J_{net} \propto \exp\left(\frac{-\Delta G^a}{RT}\right)\left\{1-\exp\left(\frac{-\Delta G}{RT}\right)\right\} \tag{4.15}$$

If the boundary is moving at a velocity v, this net flux has to be proportional to the amount of atoms displaced, $v/(V_m/N_a)$, with (V_m/N_a) the atomic volume. Rewriting equation 4.15 for the case where $\Delta G << RT$ then yields

$$v \propto \frac{V_m^2}{N_a RT}\exp\left(\frac{-\Delta G^a}{RT}\right)\frac{\Delta G}{V_m} \tag{4.16}$$

Since $\Delta G/V_m$ can be interpreted as the driving force for grain boundary migration, an expression for the mobility M of the grain boundary can be derived from equations 4.13 and 4.16.

$$M \propto \frac{1}{T}\exp\left(\frac{-\Delta G^a}{RT}\right) \tag{4.17}$$

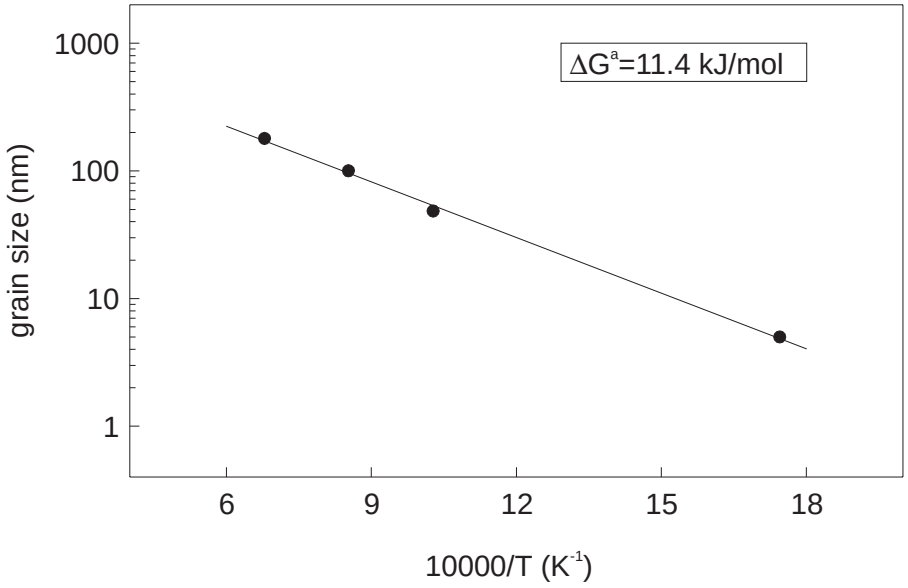

figure 4.10: *Arrhenius plot of the determined grain sizes as a function of curing temperature. The slope of the curve is a measure for the activation energy for grain growth.*

From equation 4.17 it is seen that the mobility of the grain boundaries, hence the grain growth, increases exponentially with increasing temperature. Plotting the measured average grain sizes in an Arrhenius plot delivers a straight line, with the activation energy for grain growth proportional to the slope of the line, as visualised in figure 4.10. From the line, the activation energy for grain growth in the thin TiO_2 layers is determined to be ΔG^a =11.4 kJ/mol. This value for the grain growth activation energy corresponds to values from the literature, where values ΔG^a =5-10 kJ/mol are found depending on additives like hydrolysis catalysts [27].

The micrographs of the furnace cured TiO_2 layers may give rise to the impression that the coatings consist of a layer with thickness comparable to the average grain size. Since x-ray residual stress measurements will be performed on the various cured layers, as will be discussed in section 5.4, it is important to know what the morphology of the layers is. To study the layers in cross section, a sample which has experienced a furnace treatment at 1200°C, is cleaved. A micrograph of the cross sectioned sample is depicted in figure 4.11.

The thickness of the layer as seen from figure 4.11 is larger than the average particle size as determined from figure 4.8. The layer appears to be dense

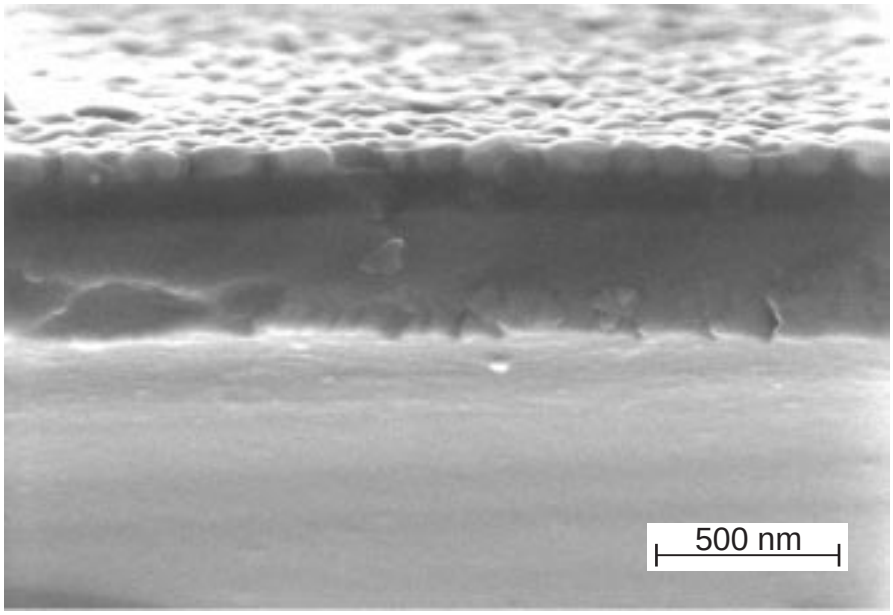

figure 4.11: *Micrograph of a cross sectioned 1200°C furnace curedspecimen. The layer has a thickness of ~500nm and appears fully dense.*

with a thickness of ~500 nm. Due to charging effects, the appearance of the layer may be blurred, masking the separate grains in the layer as they exist in the upper and lower regions of the layer. From both pictures, figures 4.8 and 4.11 it is concluded that the layer is dense and that microcracks are not present in the layer.

Laser cured TiO_2 layers

Subsequently, the laser cured thin TiO_2 are studied using scanning electron microscopy. The morphology of the laser cured layers, as depicted in figure 4.12, show a remarkable resemblance with the furnace cured layers as depicted in the preceding section. The laser cure parameters for the layers considered are listed in table 4.4

table 4.4: laser cure parameters

sample	power density ($Js^{-1}m^{-2}$)	interaction time (s)
4.12.*a*	$7.5\ 10^{9}$	$1\ 10^{-3}$
4.12.*b*	$10\ 10^{9}$	$1\ 10^{-3}$

Micrograph 4.12.*a* represents a layer which has had a low intensity laser treatment. During this laser treatment, no obviously morphology evolution of the layer has taken place. Separate grains are not visible, even at higher magnifications. Drying cracks, as observed in the furnace cured samples, are visible in the layer. Overall, the layer strongly resembles the layer which has had a furnace treatment at 300°C, indicating that the amount of energy stored in the samples during the curing process was too low to significantly change the morphology of the layer.

A sample which has experienced a laser treatment with a larger power density is depicted in micrograph 4.12.*b*. In this sample the granular structure of the layer, as observed for the samples experiencing higher curing temperatures in the furnace cured layers, is clearly present. The resolution of this micrograph is however lower than the resolution of pictures 4.4 through 4.8, since the latter micrographs were obtained using a scanning electron microscope equipped with a special immersion lens. The resolution is however large enough to distinguish between separate grains. The average radius of the particles in the layers is of the order of ~20-40 nm, which corresponds to the average grain sizes measured for the 700°C and 900°C

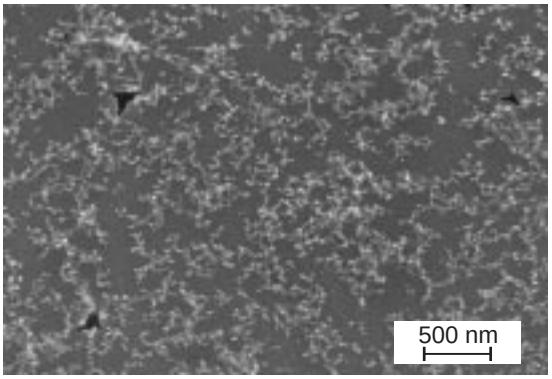

figure 4.12: *Micrographs of the laser cured TiO_2 specimen.*

a) micrograph of specimen cured with laser parameters $7.5 \cdot 10^9 Js^{-1}m^{-2}$, $1 \cdot 10^{-3}s$.

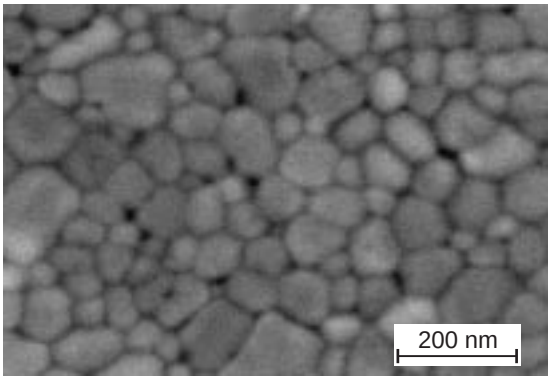

b) micrograph of specimen cured with laser parameters $10 \cdot 10^9 Js^{-1}m^{-2}$, $1 \cdot 10^{-3}s$. An evolution in grain sizes, comparable to the 300°C and the 900°C specimen is observed.

furnace treated samples. Since the interaction time during the laser treatment is small compared to the furnace curing time, the expected temperatures reached during the laser curing process in the layers has to be larger than the equivalent furnace curing temperatures.

4.3.2 Furnace densified SiO_2 thin films

The samples studied consist of a layer of SiO_2 upon a substrate of fused silica. The processing of the layer is similar to the process applied in the case of the TiO_2 layers. The precursor compound tetraethylorthosilicate, $Si(OC_2H_5)_4$ or TEOS, hydrolyses to the monomer $Si(OH)_4$, which is tetrafunctional [28]. These monomers tend to form, by condensation reactions, a network of silica polymers. After spinning, the expected thicknesses of the films is of the order of ~100-200 nm. The heat treatment of the samples consists of curing the samples in a tube-furnace at temperatures ranging from 300°C to 1200°C for

periods of time of 30 minutes. These samples are studied in cross section. To achieve a cross sectional sample, the samples are cleaved as described in section 4.1.1.

In figure 4.13 the differences in morphology of the SiO_2 layers which have experienced heat treatments at various temperatures are displayed. Micrograph 4.13.*a* depicts a sample which has experienced no heat treatment. After spinning and drying, the morphology of the layers contains features similar to the ones in this micrograph. The porosity in the layer is large. Pores of the order of particle sizes and larger can be observed. Aggregation of particles has taken place. The size of the particles is of the order of ~20-30nm. In the following micrographs, 4.13.*b-d*, the layers are depicted which have experienced heat treatments at 500°C, 1000°C and 1200°C, respectively.

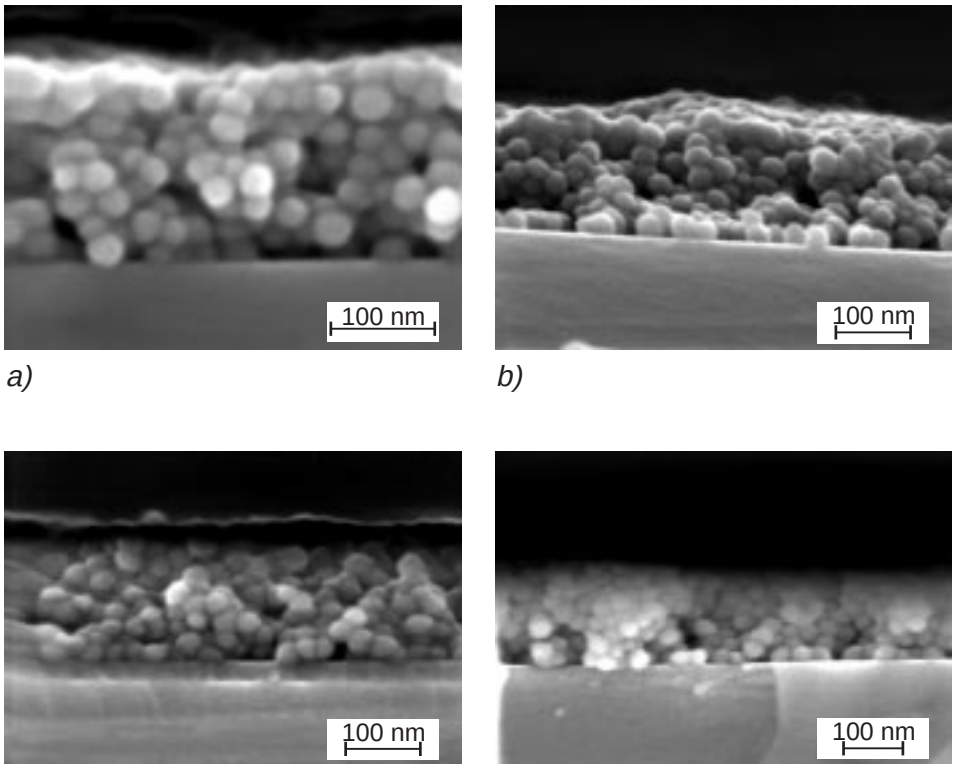

a) *b)*

c) *d)*

figure 4.13: *Micrographs of the furnace cured SiO_2 specimen.*
a) micrograph of an as spun sol gel derived SiO_2 layer.
b) micrograph of an as spun layer, which is consequently furnace cured at 500°C.
c) similar as for b) however cured at 1000°C.
d) cured at 1200°C.

From these micrographs it can be seen that no evolution in grain sizes has taken place, in contrast to the TiO_2 layers studied in section 4.3.1, an effect which may be explained by the fact that SiO_2 is more reluctant to crystallise than TiO_2 [29]. For SiO_2 thin layers, diffusional densification is expected to take place between 1000°C and 1300°C [30], explaining the decrease in porosity for the 1200°C sample.

4.3.3 Laser densified Al_2O_3 thin films

These samples receive a pre-treatment before laser curing takes place. The aim of this pre-treatment is to remove excess fluids from the layers. The procedure consists of curing the samples in a furnace at moderated temperatures for a short period of time. Subsequently, the samples are laser cured. The curing is performed using several laser parameters, as listed in table 4.5.

table 4.5: laser curing parameters

pre-treatment parameters		
code	*temperature (°C)*	*time (min.)*
1	200	5
2	400	5
3	600	5
laser parameters		
code	*power density ($Js^{-1}m^{-2}$)*	*interaction time (s)*
a	$1.3\ 10^{10}$	$2.7\ 10^{-5}$
b	$1.3\ 10^{10}$	$1.9\ 10^{-5}$

A sample with code *2b* is, as defined in the table, a sample which is dried at 400°C and during the laser curing the power density P is set to $1.3{\cdot}10^{10}Js^{-1}m^{-2}$with an interaction time τ of $1.9{\cdot}10^{-5}s$.

In figure 4.14 several micrographs are depicted of layers which have had dissimilar pre-treatments and curing conditions. Micrograph 4.14.*a* is a cross-sectional picture of a *2a* layer. Separate grains may be observed with an average grain size of the order of ~25-40 nm. The layer appears to be relatively dense, although voids and cracks may be observed. At the right-hand side debonding of the layer and substrate has taken place.

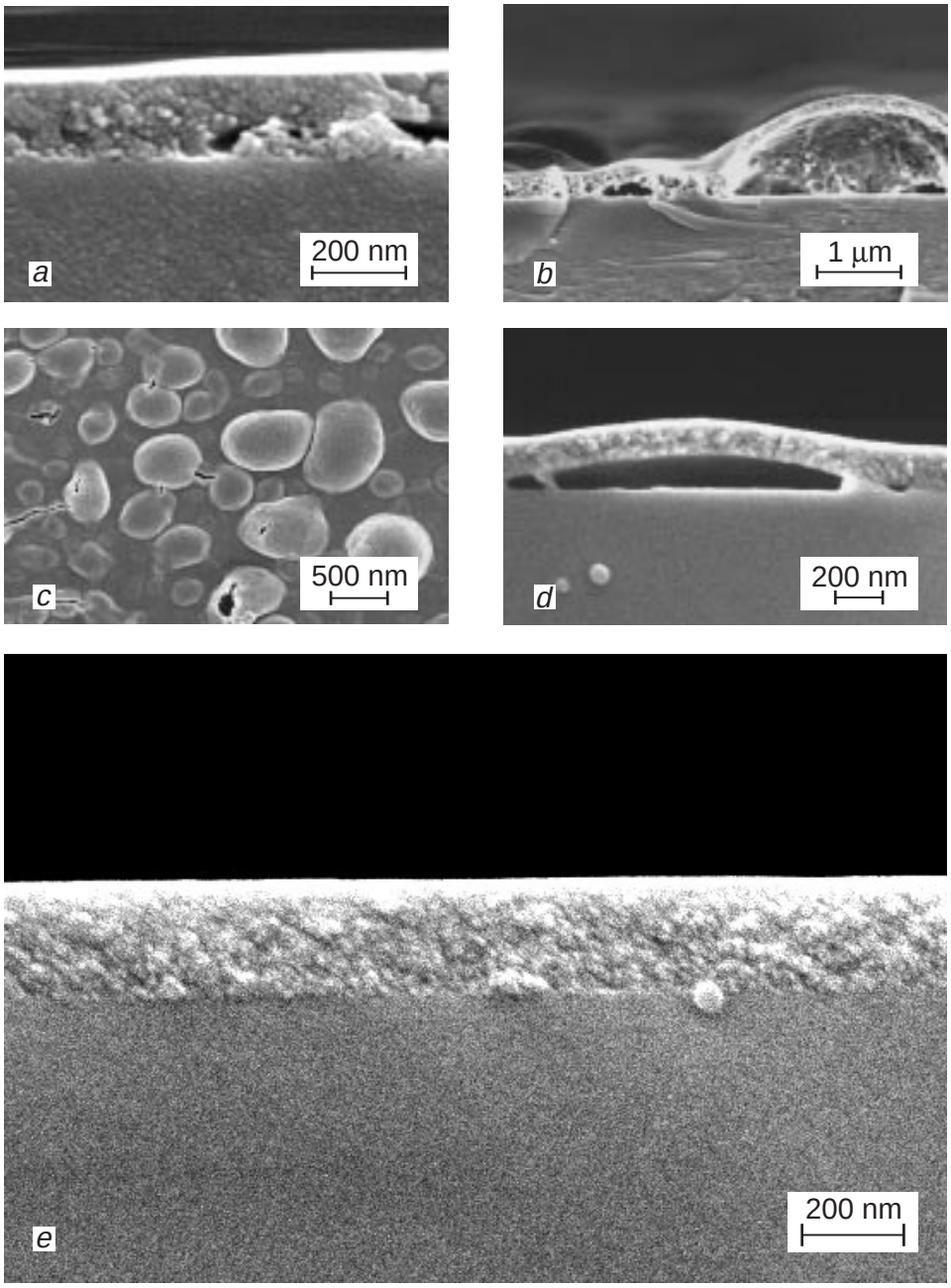

figure 4.14: *Micrographs of laser cured Al_2O_3 layers.*
a) micrograph of a 2a specimen.
b) micrograph of a 2a specimen, exhibiting catastrophical debonding between layer and substrate. The debonding may find its origin in two processes, namely buckling due to compressive thernal stresses upon curing, or degassing of entrapped liquids in the layer.
c) topview micrograph of a 2a specimen, illustrating the blisters in the layer.
d) micrograph of a 3b specimen, indicating that intensifying the pre-heat treatment reduces blister formation.
e) micrograph a 3b specimen, illustrating a homogeneous, well bonded and densified layer.

Micrograph 4.14.*b* also depicts a *2a* layer. The debonding effect as seen in micrograph 4.14.*a* is worsened and is severe. The layer is detached from the substrate and has formed a dome. A planar view of this sample, micrograph 4.14.*c*, illustrates the formation of blisters in the layer.

The blister formation may find its origin in two processes. The first effect may be due to the dissimilar thermal linear expansion coefficients of the layer and the substrate [31,32]. Since the expansion coefficient of the layer is higher than the expansion coefficient of the substrate, the layer will expand more upon heating of the layer/substrate system. This will cause compressive stresses in the layer to build up. Whenever the difference in expansion between layer and substrate, and thus the compressive stress in the layer, is large enough, the layer may fail in a buckling process and debonding between the layer and substrate will take place.

A second origin for the blister formation may be excess liquids trapped in enclosed pores [33]. During gelation of the layers, particles tend to aggregate and some fluid may be entrapped in pores. Upon heating of the layers this liquid becomes gaseous and expands drastically, building up pressure in the layer. Since the permeability of the layers is low, due to the small pores, the pressure can not leave and will cause the layer to blister. After the laser curing process, the layer is consolidated in its blistered form.

To investigate whether the blisters may be caused by entrapped fluids in the layers before laser curing, samples are dried at higher temperatures. Micrograph 4.14.*d* depicts a *3b* sample, pre-treated at 600°C. This sample still exhibits blister forming, though the effect is less severe than for samples pre-heat treated at 400°C.

Micrograph 4.14.*e* displays a region of the layer which is perfectly bonded and where densification is homogeneous. The effect that blister formation is less for layers which have had more intense pre-drying processes, suggests that the blister formation is due to entrapped fluid that expands upon heating. The pre-heating on the other hand causes the layer to densify before the laser curing. As a result of this pre-densification a tensile stress state may occur which will lower the compressive stress state in the layer due to the thermal expansion mismatch, lowering the possibility for the film to buckle. The buckling mechanism as well as the entrapped fluid mechanism will be discussed in chapter 6 in more detail.

4.3.4 Discussion

During the curing process of sol-gel derived thin TiO_2 layers, the ceramic material exhibits large changes in morphology. For the furnace cured samples, the changes involve mainly a pronounced evolution in grain sizes. It is seen that the curing temperature is influencing the final grain sizes in the layer. From the dependence of the grain size upon the curing temperature, an activation energy for grain growth is derived. The value of the activation energy, ΔG^a =11.4 kJ/mol, is comparable to values found in other studies, ranging from ~5-10 kJ/mol depending upon a grain growth catalyst added. Furthermore, the sub-micron sized cracks disappeared upon increasing the curing temperature. The cracks, as observed for the 300°C samples, are expected to be induced during the drying process of the layers. In this process, large tensile stresses evolve as a result of capillary pressures in the pores of the solid network.

The laser cured TiO_2 layers exhibit a similar evolution in grain sizes with curing parameters. Laser curing the layers with low power density results in a layer comparable to the 300°C furnace cured samples. Increasing the power density results in a layer morphology comparable to the 700°C and 900°C furnace cured layers.

The sol-gel layers derived from a TEOS precursor, resulting in SiO_2 layers, show no evident evolution in grain sizes or densification of the layer. Although the grains in the TiO_2 layers grow while being cured at elevated temperatures, the SiO_2 layers show no evolution in grain sizes. Therefore it may be concluded that the grain growth activation energy for SiO_2 is larger than the activation energy for TiO_2. Furthermore, although some evolution in the sizes of necks between particles is observed, high densities are not achieved for the lower curing temperatures. For the 1200°C cured sample, however, dense regions are observed. Diffusional densification is not expected at temperatures lower than 1000°-1300°C.

Laser curing the Al_2O_3 layers not necessarily results in homogeneous, dense layers, as may be observed from figure 4.14. The various laser treatments result in very different structures of the layers. Cracking, debonding and blister formation may be the result of the laser treatment. The formation of blisters may be ascribed to two processes. Evolution of large compressive stresses cause the layer to fail in a buckling process. The stresses necessary for buckling of the layer are assumed to be provided by the mismatch in thermal linear expansion coefficients of the substrate and the layer. Upon

heating, this mismatch induce large compressive stresses. Another cause for the formation of blisters may be the presence of volatiles in the layer, physically bound or trapped in closed pores. These volatiles expand upon heating. Due to the constraining effect of the layer, having a low permeability, the bubbles will exert a force on the layer, resulting in blister formation in the layer.

Choosing the right pre-processing treatment before laser curing the samples, results in a homogeneous, dense layer, as observed in figure 4.14.*e*.

References

1 A. Tsoga and P. Nikolopoulos, J. Am. Ceram. Soc.,**77**, (1994), 954.

2 L.J.M.G. Dortmans, R. Morell and G. de With, J. Eur. Ceram. Soc.,**12**, (1993), 205.

3 E.E. Underwood, Quantitative Stereology, Addison-Wesley, Reading, (1970).

4 L.C. Stearns and M.P. Harmer, J. Am. Ceram. Soc.,**79**, (1996), 3013.

5 M. Jimenez-Melendo, C. Clauss, A.D. Rodriquez, A.J. Sanchez-Herencia and J.S. Moya, J. Am. Ceram. Soc., **80**, (1997), 2126.

6 S.I. Bae and S. Baik, J. Am. Ceram. Soc.,**77**, (1994), 2499.

7 M.P. Anderson, G.S. Grest, R.D. Doherty, K. Li and D.J. Srolovitz, Scripta Metall., **23**, (1989), 753.

8 D.J. Srolovitz, M.P. Anderson, G.S. Grest and P.S. Sahni, Acta Metall.,**32**, (1984), 1429.

9 C. Zener, see C.S. Smith, Trans. Am. Inst. Min. Metall. Soc.,**175**, (1948), 15.

10 L.C. Stearns and M.P. Harmer, J. Am. Ceram. Soc.,**79**, (1996), 3020.

11 S. Hori, R. Kurita, M. Yoshimura and S. Somiya, J. of Mat. Sc. Lett.,**4**, (1985), 1067.

12 E. Nes, N. Ryum and O. Hunderi, Acta Metall.,**33**, (1985), 11.

13 C.J. Tweed, B. Ralph and N. Hansen, Acta Metall.,**32**, (1984), 1407.

14 R.D. Doherty, D.J. Srolovitz, A.D. Rollett and M.P. Anderson, Scripta Metall., **21**, (1987), 675.

15 Y. Liu and B.R. Patterson, Scripta Metall. Mater.,**27**, (1992), 539.

16 M.J. Mayo and D-J. Cheng, Synthesis and Processing of Nanocrystalline Powder, The Minerals, Metals and Materials Society, (1996), 227.

17 J.A. Varela, O.J. Whittemore and E. Longo, Ceramics International,**16**, (1990), 177.

18 A.G. Evans and C.H. Hsueh, J. Am. Ceram. Soc.,**69**, (1986), 444.

19 A.S. Helle, K.E. Easterling and M.F. Ashby, Acta Metall.,**33**, (1985), 2163.

20 Y. Ohya, H. Saiki, T. Tanaka and Y. Takahashi, J. Am. Ceram. Soc., **79**, (1996), 825.

21 K. Terabe, K. Kato, H. Miyazaki, S. Yamaguchi, A. Imai and Y. Iguchi, J. of Mater. Sc., **29**, (1994), 1617.

22 I. Manzini, G. Antonioli, P.P. Lottici, G. Gnappi and A. Montenero, Physica B, **208**, (1995), 607.

23 A.E. Scheidegger, The Physics of Flow through Porous Media, University of Toronto Press, Toronto, (1974), 74.

24 H. Lamb, Hydrodynamics, Cambridge University Press, London, (1932).

25 M. Gotic, M. Ivanda, A. Sekulic, S. Music, S. Popovic, A. Turkovic and K. Furic, Mater. Lett., **28**, (1996), 225.

26 W.D. Kingery, H.K. Bowen and D.R. Uhlmann, Introduction to ceramics, John Wiley and Sons, New York, (1976), 453.

27 Bokhimi, A. Morales, O. Navaro, T. Lopez, E. Sanchez and R. Gomez, J. Mater. Res., **10**, (1995), 2788.

28 S.H. Melpolder and B.K. Coltrain, Mat. Res. Symp. Proc., **121**, (1988), 811.

29 D.J. Taylor and B.D. Fabes, J. Non-Cryst. Solids, **147-148**, (1992), 457.

30 J.Y. Ying and J.B. Benzinger, Coll. and Surfaces A, **74**, (1993), 23.

31 A.G. Evans and J.W. Hutchinson, Int. J. Solids Structures, **20**, (1984), 455.

32 E. Madence, H. Balkan and M. Quan, Int. J. Solids. Structures, **32**, (1995), 3465.

33 C.J. Brinker and G.W. Scherrer, Sol-Gel Science, Academic Press, San Diego, (1990), 636.

5 RESIDUAL STRESS FIELDS

Introduction

In this section the determination of induced residual stresses during the curing process of the ceramic materials is discussed. For all engineering materials, it is of interest to know the residual stress state of the material and to be able to tailor the residual stress state. Especially for engineering ceramics, which exhibit brittle like crack behaviour, the existence of residual stresses may have a catastrophical impact on the mechanical properties of the product. Together with the grain size and pore distribution, the residual stress state determines the strength of the material.

In the first section a novel experimental method is proposed and used to measure the x-ray elastic constants of the material under consideration. This is necessary to perform the residual stress measurements on the two phase ceramic material in an accurate way. The x-ray elastic constants are derived using a method which employs a compressive applied load. This is in contrast to the more commonly used method of tensile loading.

Using the derived x-ray elastic constants the residual stress state throughout the processed specimen is determined. The derived residual stress profiles will be compared to the simulated stress profiles as described in chapter 3.

In a next section, an alternative method will be explored to determine the residual stress state in the material. This method employs a procedure of material removal. Existing stress fields will relax upon the alteration of the strained matrix. Measuring the strain relaxations in the material provides a method to determine the initial residual stress state in the material.

Finally, the sol-gel derived thin ceramic films are studied in more detail. Crystallisation, grain growth and phase evolution will be discussed. Through an extensive study of the residual stress state in the layers, more insight is gained in the evolution of stresses during the curing process of the sol-gel derived ceramics.

5.1 Determination of x-ray elastic constants

In the x-ray analysis of residual stresses based on linear elasticity theory, material constants are used. Commonly, the macroscopic materials constants, such as Young's modulus and Poisson's ratio, are employed to derive residual stresses from measured lattice strains [1-3]. As discussed in section 2.4.4, substituting *{hkl}*-plane specific x-ray elastic constants yields more accurate values for the residual stresses [4.5]. These specific constants may be calculated, according to theorems of Voigt or Reuss [6-8], or they can be measured experimentally [9-12].

5.1.1 Experimental procedures

The procedure of the experimental determination of the x-ray elastic constants of a polycrystalline specimen involves external loading of the material in-situ whilst measuring the lattice spacings of the *{hkl}* lattice set under consideration. Determination of the line shift of the Bragg reflections delivers information of the elastic response of the lattice set induced by the applied external load. As discussed in section 2.4.5, an applied external load alters lattice strains, as measured by x-ray diffraction, according to

$$\varepsilon_{33,\phi=0,\psi} = \tfrac{1}{2}S_2^{\{hkl\}}\left(\sigma_{\phi}^{IS} + \sigma^{AS}\right)\sin^2\psi + S_1^{\{hkl\}}\left(\sigma_{11}^{IS} + \sigma_{22}^{IS} + \sigma^{AS}\right) \qquad (5.1)$$

In this equation, the superscripts *IS* and *AS* stand for internal stress and applied load, respectively; $\frac{1}{2}S_2^{\{hkl\}}$ and $S_1^{\{hkl\}}$ represent the *{hkl}*-plane specific x-ray elastic constants. Determining the lattice spacings $d_{\phi,\psi}^{\{hkl\}}$ of the externally loaded specimen will result in values that differ from the strain-free lattice spacing d_0. The resulting lattice strain can then be calculated according to equation 2.12.

To derive the x-ray elastic constants of the material under investigation from the measured lattice strains, the measured lattice strains are plotted versus the specimen orientation ψ. The gradient and the intersection with the ordinate of this line is a measure of $\frac{1}{2}S_2^{\{hkl\}}\sigma^{AS}$ and $S_1^{\{hkl\}}\sigma^{AS}$, respectively. If the applied stress state in the material is known, the plane specific x-ray elastic constants are known. This procedure does however only hold in the case when the material is internally stress free. For materials containing a non-zero internal stress state, or if the internal stress state in the material is unknown, an alternative procedure has to be followed.

A method to tackle the influence of an unknown internal stress state in the material is to consider not only the response of the lattice strain upon specimen orientation but also upon various applied external loads. Taking the derivative of equation 5.1 with respect to the applied load and specimen orientation will cancel the influence of an existing internal stress state. Following this procedure, expressions for the x-ray elastic constants can be derived.

$$\frac{\delta^2 \varepsilon_{33,\phi=0,\psi}}{\delta \sin^2\psi \, \delta\sigma^{AS}} = \tfrac{1}{2} S_2^{\{hkl\}} \quad \text{and} \quad \frac{\delta \varepsilon_{33,\phi=0,\psi=0}}{\delta\sigma^{AS}} = S_1^{\{hkl\}} \tag{5.2}$$

Experimental details

The experimental determination of the x-ray elastic constants is performed by in-situ loading the specimen on a Philips PW1820 goniometer. This goniometer is of the ω-type. The high voltage generator is operating at 30 kV and 40 mA. *Cu-K*α radiation is used. To eliminate multiple Bragg reflections, caused by β–radiation, a nickel filter at the primary optics side is used.

The actual loading takes place in a force-controlled pressing device, as depicted in figure 5.1. Specimens are subjected to a uniaxial compressive stress state in the pressing device. This loading mode is used in contrast to the commonly used techniques like bending or tensile testing. The reason for using the uniaxial compressive loading mode is that while loading the material in compression, surface defects, micro-cracks or pores in the upper surface layer, become of less influence to the induced stress state. This is not the case for loading in tension and bending.Another advantage of the uniaxial loading mode is that there is no dependence of the stress field with the depth in the specimen. A bending device for instance, delivers a stress gradient within the specimen, causing the determined lattice strain to be an average of all the lattice strains over the materials volume sampled.

Finally, using a compressive loading mode instead of a tensile loading mode, used in bending or tensile testing, the ultimate applied load may reach higher values before mechanical failure of the specimen occurs. The latter is especially an advantage in the determination of the x-ray elastic constants of brittle materials, like ceramic materials, for which the ultimate strength in compression is much larger than the ultimate strength in tension [13].

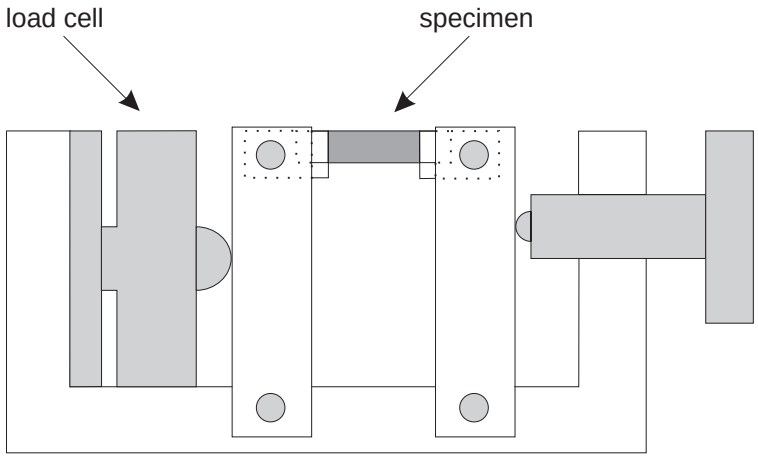

figure 5.1: *Main parts of the in-situ pressing device.*

In this kind of experiments a large error can be introduced by misalignment of the specimen with respect to the optical axis of the goniometer. A slight deviation in height adjustment will result in a deviation of the lattice spacings $d_{\phi\psi}$ measured. To check for the correct height adjustment of the specimen, a thin layer of silicon powder is brought onto the surface of the specimen. This is done by suspending silicon powder of appropriate grain sizes in iso-propanol. Applying the suspension to the surface will, after the evaporation of the iso-propanol, result in a thin layer of strain free silicon powder. The *{311}* lattice planes of silicon, at 2θ=56.122°, serve as a height calibration check before the actual measurements are performed. Along with the measurements also a silicon scan is recorded, which can be used for corrections afterwards.

For the homogeneous as well as the two-phase material, the *{146}* lattice planes of the α-alumina are measured for several applied loads and crystal orientations. The applied stresses, which are calculated from the applied load and the specimen dimensions, range from 75 to 275 MPa. The near surface stress distribution is assumed to be homogeneous and uniaxial, justified by the loading mode chosen. As a result of the homogeneous stress state in the specimen, no corrections for different penetrations depths, as necessitated for bending testing, are required. Since the goniometer only allows for ω-tilting, crystal orientations ψ are limited by the diffraction angle θ at which the Bragg reflections are measured. Specimen orientations range from 0 to 45 degrees with a step of $\Delta sin^2\psi$=0.05.

Several corrections are performed on the measured Bragg reflections. The range over which the line profiles are recorded is large enough to determine a background level. This background level is subtracted from the measured profiles. In the case of a linear background, subtraction of the background does not influence the peak position. If the background increases or decreases with 2θ, the position will deviate from the true 2θ value. Subtraction of the background then delivers more accurate values.

The same holds for $K\alpha 2$ stripping. The reflections of both $K\alpha 1$ and $K\alpha 2$ radiation are overlapping. The peak positions are influenced by the overlapping Bragg reflections, depending on the 2θ value of the reflection. For larger 2θ values, the overlap in 2θ space is less than for smaller 2θ values. A calculated $K\alpha 2$ profile, based on the measured profile, the $K\alpha 1/K\alpha 2$ intensity ratio and the $K\alpha 2$ wavelength, is substracted from the profile. The peak position may be derived in an accurate way from the corrected profile.

5.1.2 Experiments

The results of the loading experiments on the two-phase material are depicted in figure 5.2.*a*. In this graph the dependence of the Bragg-angles 2θ, which are converted to lattice spacings $d_{\phi\psi}$ using Bragg's law, on specimen orientation ψ and applied loads σ^{AS} are displayed. From the graph it is seen that the lines exhibit a common point of intersection. This common point of intersection provides a value for the strain-free lattice spacing d_0 and a value for $sin^2\psi_0$, the orientation for which the lattice spacings are not influenced by a stress state. An estimate for the point of intersection may be derived from figure 5.2.*a*, however, a better value for the intersection point of the lines may be derived following a method proposed in [14]. Plotting the intercept at $\sin^2\psi = 0$ versus the tangent of the $d^{\{hkl\}}_{\phi=0,\psi}$ versus $\sin^2\psi$ lines, as in figure 5.2.*b*, results in a data set through which, in the case of perfectly intersecting lines, a straight line may be fitted, according to

$$d^{\{hkl\}}_{\phi=0,\psi=0} = d^{\{hkl\}}_0 - (m_d)\sin^2\psi_0 \qquad (5.3)$$

In this formula, m_d represents the slopes of the $d^{\{hkl\}}_{\phi=0,\psi}$ versus $\sin^2\psi$ lines. With this relationship, the strain-free lattice spacing and orientation may be determined from the slope of the line, delivering the strain free orientation, $\sin^2\psi_0$ and the interception with the ordinate, $d^{\{hkl\}}_0$. Both values are listed in table 5.1.

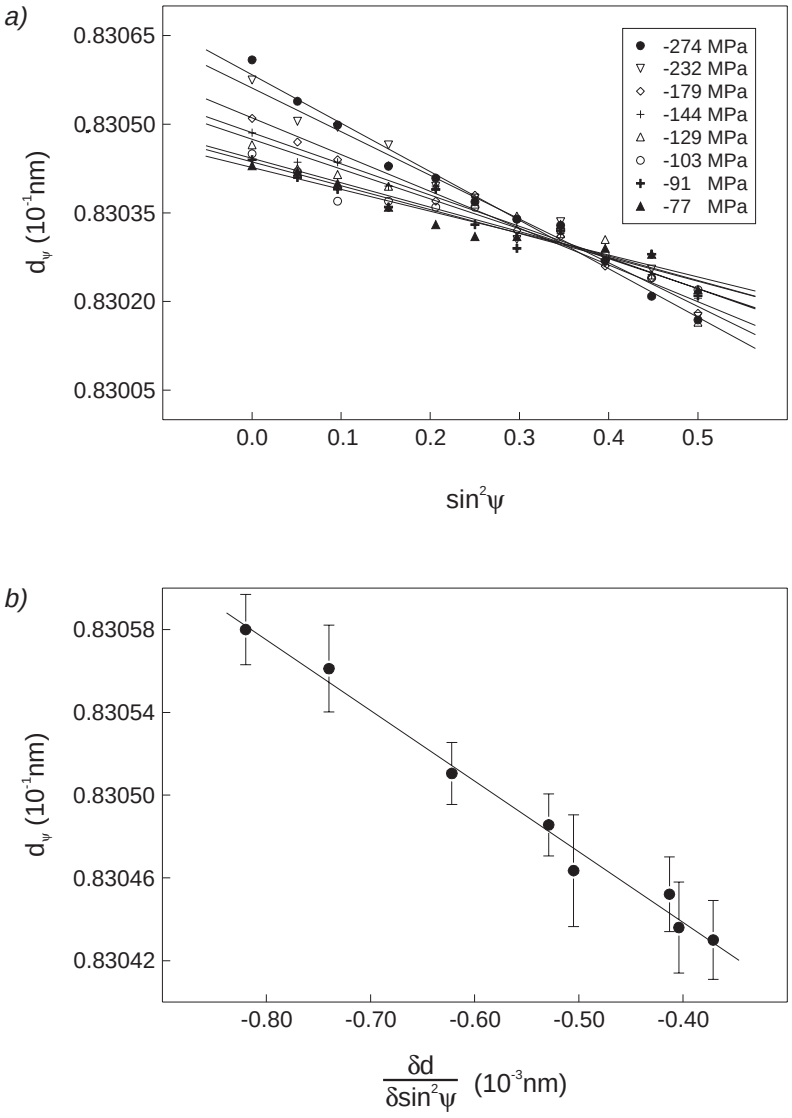

figure 5.2: *Results of the loading experiments*
a) Measured $d^{\{hkl\}}$-spacings as a function of crystallite orientation ψ for various applied loads.
b) Determination of the best intersection points of the lines depicted in a).

table 5.1: strain-free lattice parameters

spacing (10^{-2} nm)	orientation
d_0=8.30298	$\sin^2\psi_0$=0.348

The strain-free lattice orientation provides a value for the strain-free lattice spacing. Transformation of equation 2.14 using the strain-free lattice spacing and strain-free orientation yields

$$\sin^2\psi_0 = \frac{-2S_1^{\{hkl\}}}{\frac{1}{2}S_2^{\{hkl\}}} \tag{5.4}$$

Since the plane specific x-ray elastic constants, for the isotropic linear elastic case, are defined as $S_1^{\{hkl\}} = \frac{-\nu}{E}$ and $\frac{1}{2}S_2^{\{hkl\}} = \frac{1+\nu}{E}$, an expression for Poisson's ratio ν can be derived from equation 5.4

$$\nu = \frac{\sin^2\psi_0}{2-\sin^2\psi_0} \tag{5.5}$$

For the two-phase material, using equation 5.5 and the values listed in table 5.1, a value for Poisson's ratio is determined, ν=0.21, which is a value typical for polycrystalline α-alumina. From the strain-free lattice spacing, the strains $\varepsilon_{33,\phi=0,\psi}^{\{hkl\}}$ are calculated using equation 2.11. The strains are plotted in figure 5.3.*a* as a function of the applied load. Each line represents the elastic response to applied stress for different crystal orientations ψ in the specimen. The slopes of the lines $\delta\varepsilon_{33,\phi=0,\psi}^{\{hkl\}}/\delta\sigma^{AS}$ represents $\{\frac{1}{2}S_2^{\{hkl\}}\sin^2\psi + S_1^{\{hkl\}}\}$.

Consequently, plotting the derived slopes versus $\sin^2\psi$, figure 5.3.*b*, yields the x-ray elastic constants, the gradient of the line is a measure for $\frac{1}{2}S_2^{\{hkl\}}$. The intercept with the ordinate yields $S_1^{\{hkl\}}$. The linear relationship, expected from equation 5.1, is fulfilled in figure 5.3.*b*. The experimentally determined x-ray elastic constants for the two-phase material are listed in table 5.2.

table 5.2: x-ray elastic constants

Material	S_1 (10^{-6} MPa^{-1})	½S_2 (10^{-6} MPa^{-1})
Al_2O_3/ZrO_2	-0.99±0.08	2.83±0.16
Al_2O_3	-0.83±0.02	2.97±0.07

In table 5.2, the x-ray elastic constants for pure α-alumina are also given. These values are derived in a similar way as the values for the two-phase

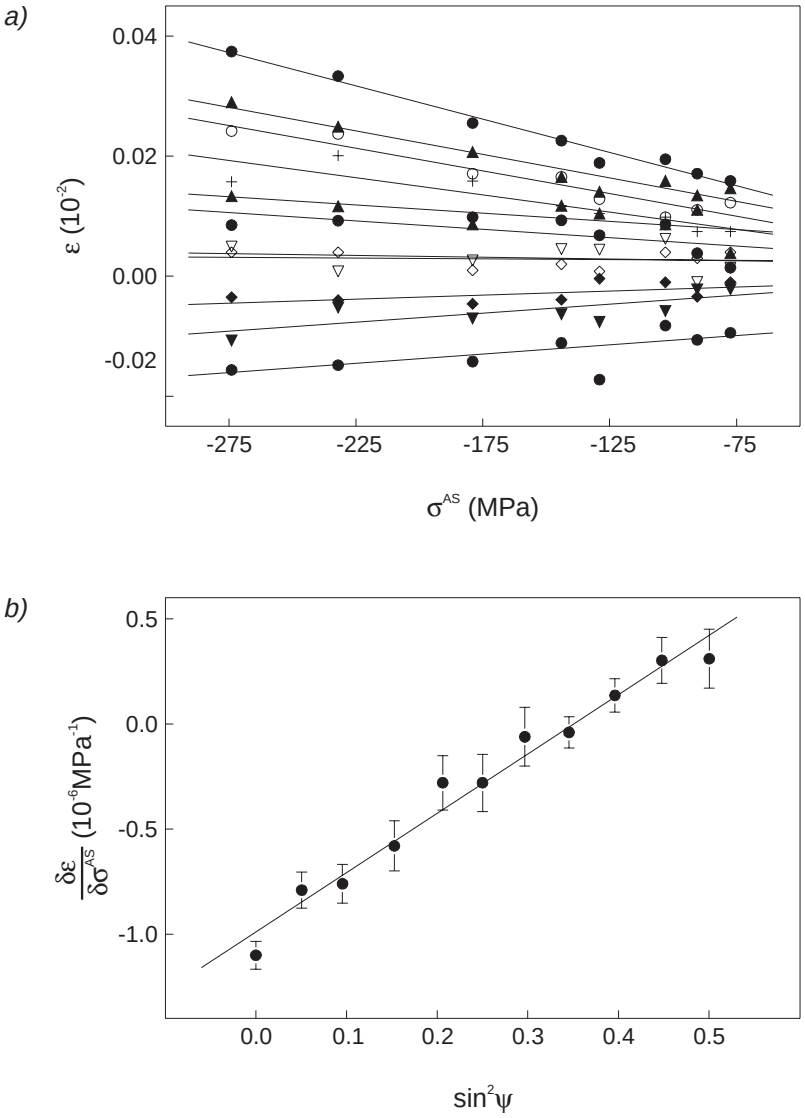

figure 5.3: *Derivation of the x-ray elastic constants from the measurements in 5.2*
a) Lattice strains, as derived from figure 5.2a using equation 2.12, as a function of the applied load for the various crystallite orientations considered.
b) The gradients of the lines depicted in figure (5.4) as a function of crystallite orientation ψ. The slope of the line represents ½S_2 and the intercept S_1.

material. From the table it is seen that the values for the stress constant $\frac{1}{2}S_2^{\{hkl\}}$ for both materials differ only by a small fraction. It means that the elastic response of the material for the lattice planes under investigation differs only by a small degree, which may be expected since both materials mainly consist of α-alumina.

In table 5.3 some other values for the x-ray elastic constants for the *{146}* lattice set of α-alumina are listed. The values are derived in various ways. The calculated values are mean values using the Reuss approximation. The other x-ray elastic constants are experimentally determined using different evaluation techniques, where the main difference in the experimental techniques is the applied mode of loading.

table 5.3: α-alumina x-ray elastic constants

evaluation technique	$\frac{1}{2}S_2$ (10^{-6} MPa^{-1})	S_1 (10^{-6} MPa^{-1})
Reuss average	3.57	-0.76
4-point bending	3.06	-0.42
	3.36	-0.92
tensile loading	3.08	-0.56

5.1.3 Discussion

Using the in-situ pressing device, the x-ray elastic constants are determined for the homogeneous as well as the heterogeneous material. The experimentally derived values for the x-ray elastic constants do not show significant discrepancies for the α-alumina and the two-phase material. Since the determination of these values is performed using similar methods and the experiments are conducted analogously, the derived values are comparable for both materials. X-ray residual stress analysis, using the derived values for the stress constant delivers more accurate values than using the macroscopic elastic constants, Young's modulus and Poisson's ratio.

The experimentally derived values for the x-ray elastic constants of α-alumina using compressive loading do, however, deviate from the calculated values using the Reuss and Voigt approximations. The other values in table 5.3, representing x-ray elastic constants derived in differing experimental procedures, do also exhibit deviating values from the calculated ones. This is an indication that the values obtained in the Reuss and Voigt approximations are only valid for ideal materials, that is to say where in all the crystallites the stresses, for the Reuss limit, or the strains, for the Voigt limit, are indeed equivalent. Since the experimental x-ray elastic constants differ from the calculated ones, these assumption do not hold. The order of magnitude of the calculated x-ray elastic constants does however correspond to the experimental values.

In the determination of residual stresses in the pellet material, the experimentally derived x-ray elastic constants for the homogeneous and the heterogeneous material will be used to make the conversion from experimentally determined lattice strains to residual stress fields in the ceramic materials.

5.2 Residual stress fields in two-phase ceramic pellets

Introduction

During the processing of the ceramic pellets there are several stages in which residual stresses may evolve in the specimen. In this section residual stress fields will be evaluated and compared to the calculated ones in section 3.2.3, based upon finite elements calculations involving thermal expansion misfit.

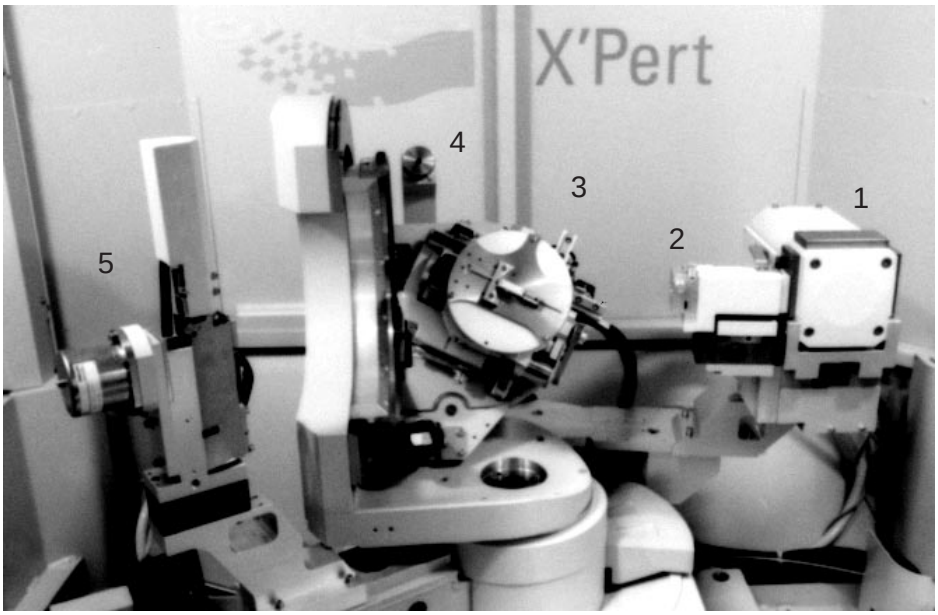

figure 5.4: *Experimental set-up of the diffractometer.*
1: X-ray tube
2: Crossed slit collimator
3: Specimen
4: Goniometer
5: Detector

The derivation of the residual stress fields is performed using the determined x-ray elastic constants for the two-phase and homogeneous material, see section 5.1. With use of these constants, the error in the measurements due to the contribution of erroneous material constants is minimised.

5.2.1 Experimental procedures

The actual residual stress measurements are performed on a Philips X'Pert PW 3040 x-ray diffractometer. A picture of the experimental set-up of the diffractometer is displayed in figure 5.4. The diffractometer is equipped with a ψ-goniometer, PW 3050 with MRD-Cradle. This ψ-goniometer, where the specimen tilt axis is perpendicular with the θ–axis, delivers a main advantage over a ω-goniometer, where the specimen tilt axis coincides with the θ-axis. For the ψ-goniometer, the range of specimen orientations is not limited by the diffraction angle as is the case for an ω-goniometer. It is theoretically possible to measure lattice spacings $d_{\phi\psi}$ for $sin^2\psi$ values upto 1.0. In order to employ the ψ-tilting properly, the x-ray tube is mounted to deliver a point-focus beam. A crossed slit collimator is used to adjust the horizontal and vertical divergence of the beam, hereby determining the spot size of the beam on the specimen.

Since residual stress measurements acquire only precise Bragg-angle shifts instead of precise Bragg-angle determination, a wide receiving slit is used at the secondary optics side in order to increase diffraction yield and minimise measuring times. The generator operates at 40 kV, 50 mA and *Cu-K*α radiation is used. For both negative and positive ψ-tilts in the range $-50.7° \leq \psi \leq 50.7°$, the lattice spacings $d^{\{hkl\}}$ are determined over a range of 2θ which is large enough to perform corrections for background subtraction and *K*α*2* stripping. The reflection of interest is the *{146}* α-alumina reflection. In the conversion from derived lattice strains to residual stress values, the experimentally derived *{hkl}*-plane specific x-ray elastic constants are used.

The horizontal and vertical divergence determine, together with the θ and ψ angles, the dimensions of the irradiated spot on the specimen, for the ψ–goniometer according to

$$A = \frac{1}{\sin\theta\cos\psi} \tag{5.6}$$

In figure 5.5 the effective irradiated spot size is illustrated as a function of θ and ψ. Since the x-ray residual stress determination will yield stress values at a series of discrete points, the maximum tilt angles should be chosen in such a way that the irradiated spot should be as constant as possible, so no overlap occurs for the points of interest. For the residual stress measurements performed on the pellets, an area in θ and ψ space, as defined by the shaded rectangle in figure 5.5, is used for the experimental determination of the residual stresses at every point. It is seen from the graph that the dimension of the spot does not change significantly over the area of interest. This justifies the assumption that the effective irradiated spot size is constant over the range of tilt angles in the experiments.

Since the penetration depth of the x-ray beam is governed by the goniometer geometry and the material properties of the material under investigation, care should be taken to maintain the penetration depth for the successive scans as constant as possible. In figure 5.6 the effective penetration depth is plotted as a function of θ and ψ for the ψ-goniometer set-up, in arbitrary units depending upon the absorption coefficient of the material.

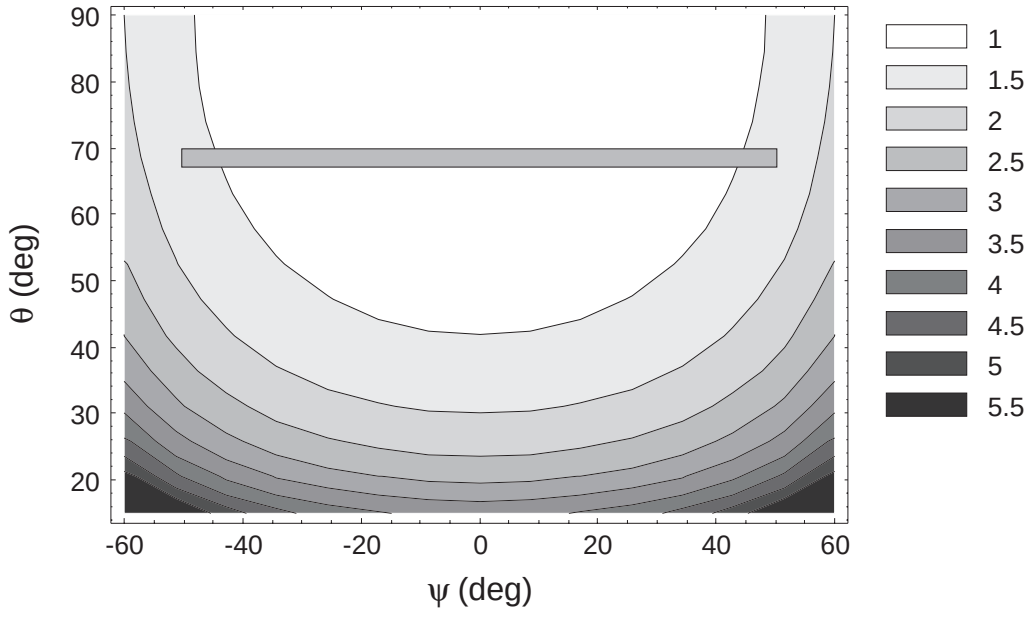

figure 5.5: *Dependence of the dimension of the spot size on diffraction angle ω and specimen tilt angle ψ.*

The penetration depth for a ψ-goniometer set-up is given by

$$\tau = \frac{\sin\theta\cos\psi}{2\mu} \tag{5.7}$$

In the contour plot 5.6 a rectangular area depicts the area over which the measurements are performed. From the figure it is seen that for the scans performed for ψ-tilts at the maximum values $\sim|50°|\psi$, the penetration depth is ~0.2 the penetration depth of scans performed at $0°\psi$. When a significant stress gradient exists over this depth interval, $d_{\phi\psi}$ versus $\sin^2\psi$ curves will exhibit a non-linear dependence. To determine if the varying penetration depth becomes a problem, these curves have to be examined.

In the determination of residual stresses, the influence of an error in height adjustment is, in contrast to the experimentally determination of the x-ray elastic constants, fairly small. In figure 5.7 the influence of a height offset on the derived residual stress values is displayed. The horizontal line represents the average stress value, as determined from the successive measurements.

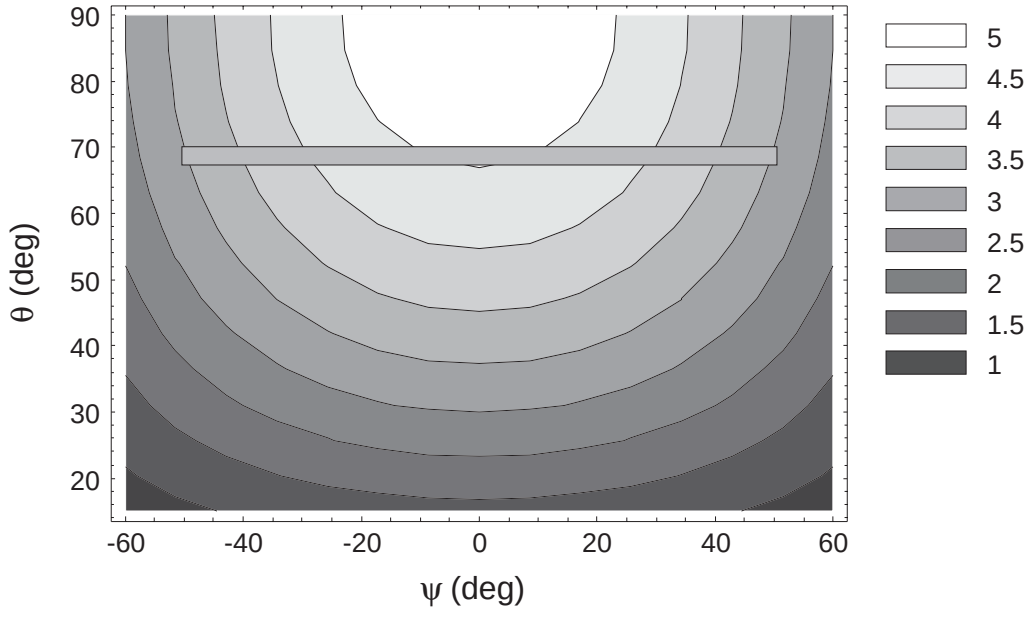

figure 5.6: *Dependence of the penetration depth, in arbritary units depending on the absorption coefficient μ, on diffraction angle ω and specimen tilt angle ψ.*

From the graph it is seen that the stresses measured, which should be equal for all height displacements, show some discrepancies. The deviations are however small and the measured stress values all fall within the error bars. Over the range of height displacement considered, it is concluded that the displacements do not influence the stresses.

Residual stress fields are measured at various locations throughout the specimen. In the measurements, only the separately processed specimen are considered. At the side of the specimen, the axial as well as the tangential component of the stress field can be determined without disturbing the stress fields. If stresses within the specimen are of interest, some sort of mechanical material removal has to be employed. The machining consists of sectioning the specimen so that the diffraction information gained is from the position of interest. After sectioning, the specimen are polished to remove a possibly plastically deformed surface layer.

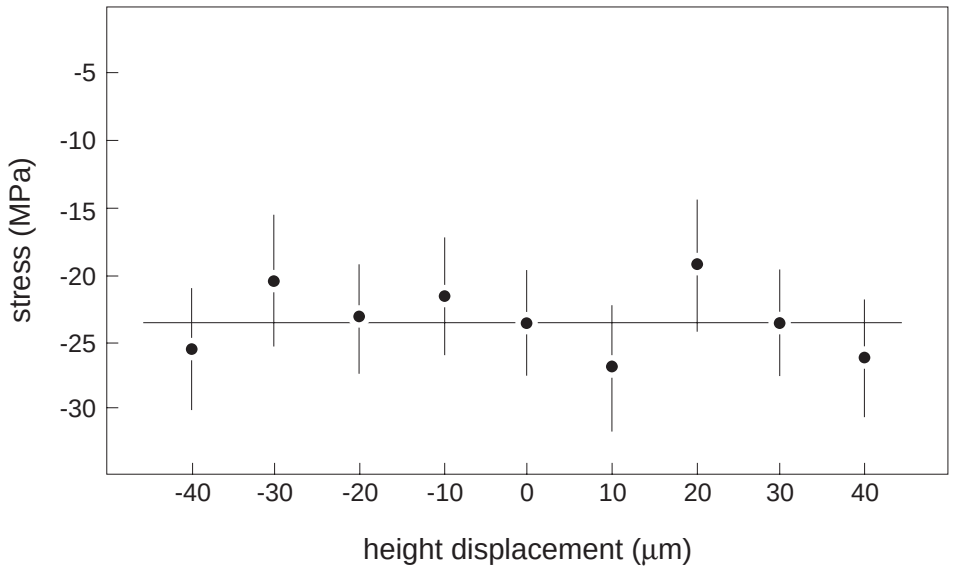

figure 5.7: *Influence of misalignment of the specimen, with respect to the optical axis of the goniometer, on the residual stresses measured.*

5.2.2 Experiments

To derive the residual stress fields in the composite ceramic pellets, several residual stress profiles are determined at various locations. In figure 5.8.*a*, the tangential residual stress profile at the side of a pellet is displayed.

In this figure also the thermal misfit stress, based on FEM calculations, is plotted as a dotted line. The experimentally derived residual stress profile, matches the calculated profile well over the interfacial region. Approaching the edge of the specimen, the experimentally determined values show discrepancies with the calculated ones. Since the specimen are pre-processed, hence pre-shrunk, it can be expected that in the pre-sinter process already residual stresses are induced, which influence the stress state in the pellets.

The influence of a pre-existing residual stress state in the separate layers, on the final residual stress state in the pellets is investigated by determining the residual stress state in the separate layers, prior to the diffusion bond process. To measure these residual stresses in the separate layers of both the homogeneous material and the two-phase material, residual stress profiles are determined using similar procedures as for the pellets. The derived residual stress profiles are depicted in figure 5.8.*b*.

The residual stress components measured are the tangential stresses along a line parallel to the axial direction at the side of the separate layers of the pellets. The derived profiles display zero stress values in the centres of both layers. Approaching the edges, the homogeneous layer displays compressive stress values, whereas the stress state in the two-phase material becomes tensile. This difference may be due to the dissimilar material properties of both materials or the difference in microstructure and densification behaviour of both powder compacts. In section 3.1.2 it was shown that the two-phase material exhibits larger shrinkage upon sintering than the homogeneous material, an effect that is also discussed in section 4.2.

To determine whether the stresses induced in the pre-sinter process alter the expected residual stresses, based on thermal misfit, the determined profiles are subtracted from the calculated residual stress profile, as depicted in figure 5.9. In this figure also the experimentally derived profile is depicted.

The dotted line in this graph diplays the calculated profile, which is corrected for pre-sinter induced stresses, the solid line is the experimentally derived profile. The experimentally determined residual stress profile exhibits

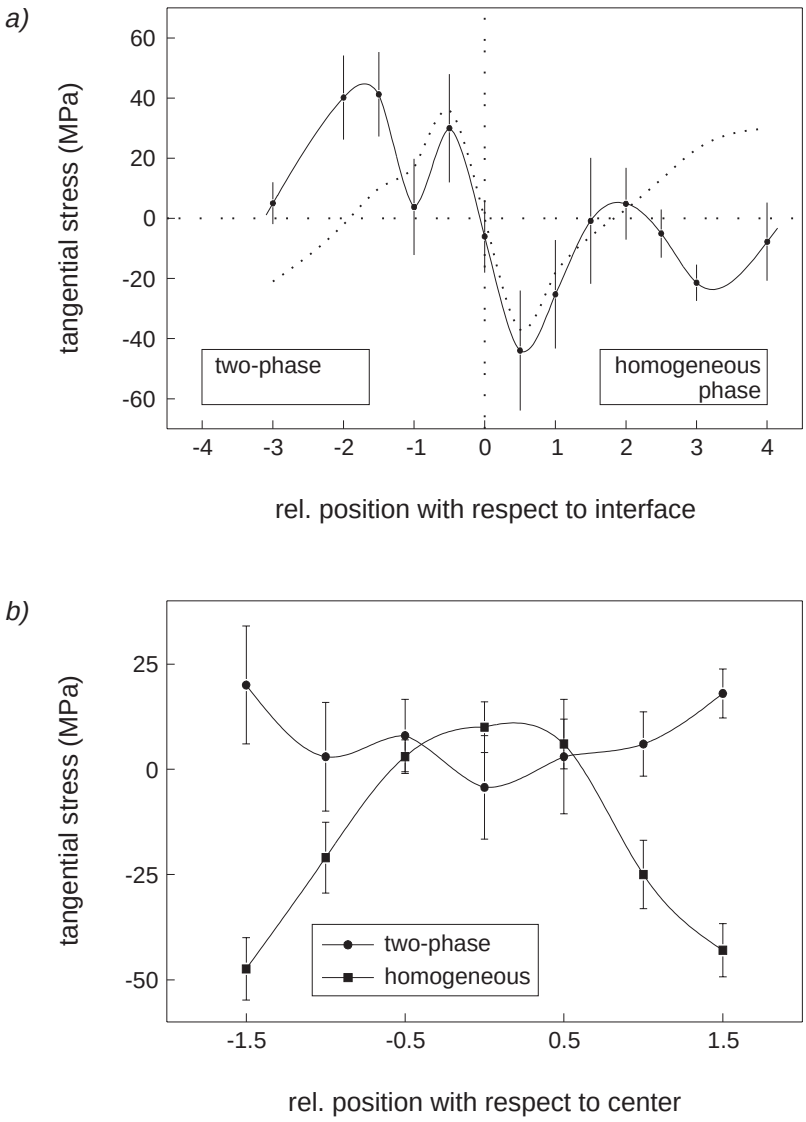

figure 5.8: *Residual stresses in pellet and separate layers*
a) Determined tangential residual stress component in the sinter-bonded pellet. The calculated stress profile, according to finite element considerations, is depicted as well.
b) Determined tangential residual stress component in separate layers.

behaviour similar to the corrected calculated profile over the interface region. For the homogeneous side of the pellet, the experimentally derived profile resembles the simulated profile significantly. Except at locations close to the interface, the measured stress values correspond to the calculated ones. The

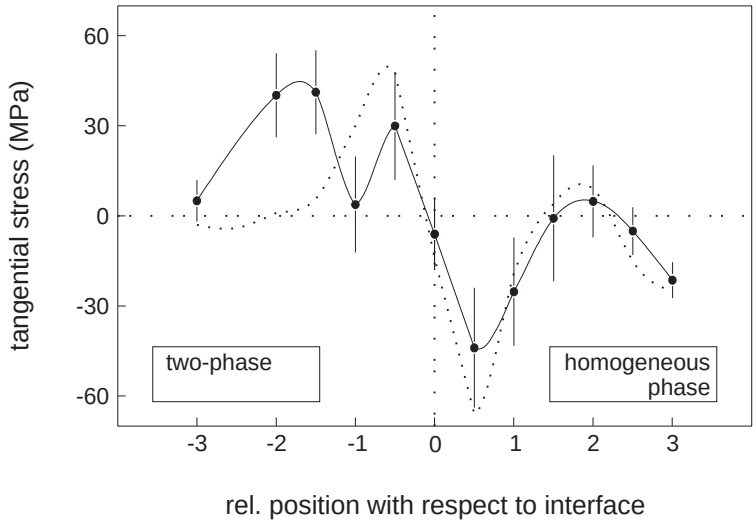

figure 5.9: *Superposition of the calculated residual stress profile and the residual stress profiles as determined in figure 5.8.b. The measured tangential stress component in the sinter bonded pellet, figure 5.8.a, exhibits for the homogeneous layer, comparable behaviour as the expected stress profile. The heterogeneous profile deviates from the expected profile for regions remote of the interface.*

values close to the interface, however, are suppressed by the averaging effect of the finite dimensions of the spot size, indicating that the true stress values are somewhat larger in the vicinity of the interface. The values determined experimentally for the two-phase material layer, display similar behaviour in the vicinity of the interface as the calculated values. In the center of the two-phase layer however, the experimental values deviate from the expected values.

As stated earlier, the calculated values are solely based on differences in thermal expansion coefficients of both materials, where the thermal expansion coefficient of the two-phase material is taken as the weighted average of both the α-alumina matrix and the added ZrO_2. The influence of the second phase itself on the shrinkage behaviour should also be considered in the simulations. For the interfacial region, the simulated stress profile compares well to the experimentally determined profile.

Consequently, the axial residual stress component at the side of a pellet is measured. The determined residual stress profile, together with the calculated profile, is depicted in figure 5.10. The experimentally determined residual stress profile exhibits behaviour similar to the calculated profile. As concluded for the tangential stress component earlier, the experimental curve is comparable to the calculated one over the interfacial region. Approaching the edges, the axial stress component as well as the tangential stress component, deviates from the expected values as is seen in both figures 5.9 and 5.10. The error margins for the axial stresses measured, increase in the vicinity of the interface.

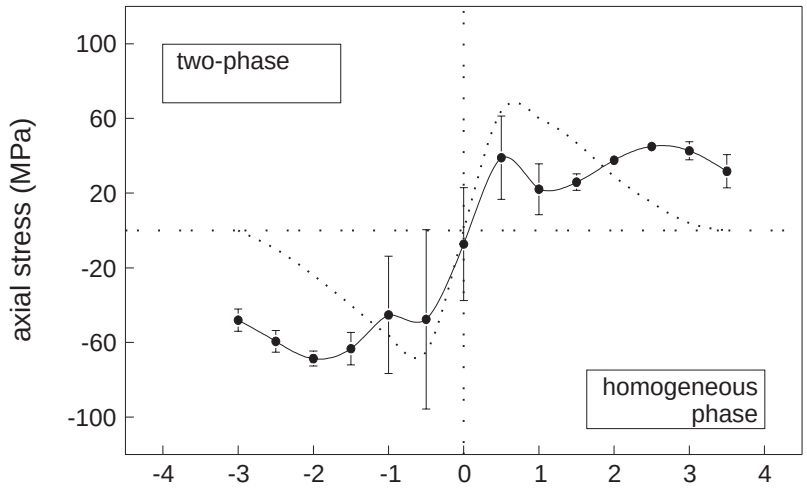

figure 5.10: *Determined axial stress component in the sinter bonded pellet. The calculated profile is indicated as the dotted profile.*

Finally a cross section is made of a pellet to determine the radial residual stress component inside the specimen. From section 3.2.3, the expected residual stress values for the tangential and the radial components are similar at positions in the specimen where side effects may be neglected. This is in agreement with elasticity theory [15], i.e. the radial and tangential components in a axisymmetrical stress distribution are equal if the material contains no holes. Sectioning the specimen will result in a redistribution of the residual stresses in the specimen. Since the stress fields are constant in the

bulk of the specimen, and sectioning is performed over the center of the specimen, only the tangential stresses will be relaxed and the radial stress are left undisturbed. If the sectioning is performed over a plane which does not contain the center of the specimen, the stresses in the plane of sectioning are still undisturbed, since a superposition of the radial and tangential stresses may be performed, leaving the eventual stresses in the plane of sectioning equal in size and magnitude to the radial stresses or the tangential stresses in the specimen.

After cutting the specimen, the sectioned surfaces are polished and etched simultaneously to remove possible plastically deformed material from the surface. Consequently, x-ray residual stress measurements are performed on the revealed surfaces. In figure 5.11 the determined residual stress profile as well as the simulated profile are displayed.

Bearing in mind that the stress state of the pellet is altered by the mechanical machining, the measured profile resembles the calculated profile. Overall however, the measured values are shifted to compressive values. An effect which may be ascribed to mechanical machining, is that the surface layer has deformed plastically and compressive stresses are induced in the specimen.

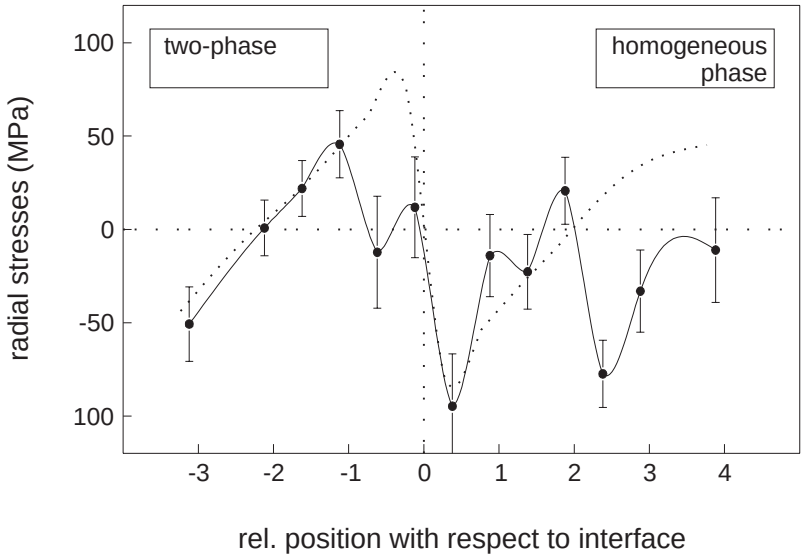

figure 5.11: *Determined radial stress component in a cross sectioned specimen. The calculated profile is indicated as the dotted profile.*

5.2.3 Discussion

X-ray residual stress profiles are determined for locations throughout the composite ceramic pellets. The profiles are compared to the finite element derived profiles, as described in section 3.2.3. Since deviating values were found experimentally, the residual stress state in separate layers of homogeneous as well as the two-phase material is investigated. After subtracting these measured residual stress fields, which evolved during curing of the separate layers, from the calculated residual stress profiles, the experimentally determined x-ray residual stress profiles are comparable to the calculated residual stress values.

The areas in the specimen where the experimental curves for all $\sigma_{i,j,k}$ resemble the calculated profiles best, are the interfacial regions. These regions are of importance for the production of the composite ceramic pellets since they are most likely to fail during the production process. If the stresses evolved during curing exceed the fracture stress of the material, the separate layers will debond over the interface. Therefore it is of particular interest that the stresses in these regions are known prior to the choice of production parameters, like curing temperatures and pre-processing conditions. Assuming that the main source of residual stresses in these processes are the thermally induced misfit stresses [16], finite elements calculations proved to deliver reliable values for the residual stress components which do correspond well for the regions of interest.

The magnitude of the stress measured ranges typically between ~60 MPa and -60 MPa. The maximum stress is found in the vicinity of the interface. As already discussed in section 3.2.3, failure of the ceramic material depends upon the magnitude of the critical stress intensity factor. This means that in the case of α-alumina, with $K_{Ic} = 4\ MPa\sqrt{m}$, for microcracks ~5 μm in size, the critical stress is found to be equal to ~1 GPa. Therefore, using the curing conditions as described here will not result in debonding of the dissimilar ceramic materials.

5.3 Hole relaxation stress determination

Introduction

In the former section x-ray residual stress analysis is employed to derive residual stress fields in the composite ceramic materials. The application of x-ray residual stress analysis, however, is limited to materials which satisfy certain requirements. If the material is for instance non-crystalline or heavily textured, x-ray stress analysis cannot be employed. For these materials several other methods may be used to derive residual stress states. Here, a method known as the hole drilling technique will be explored to provide more insight in the residual stress state in the composite ceramic materials.

5.3.1 Theoretical background

An alternative method providing insight in the residual stress state in a specimen is the so called hole drilling technique [17-20]. This technique deduces stress values from strain relaxations in the vicinity of an introduced, well defined hole in the material. The strain relaxation is measured by strain gauges attached to the surface of the material prior to the introduction of the hole. These strain gauges exist of long, folded flat resistance wires, which will elongate when subjected to an external force. The elongation of the wires causes their electrical resistance to vary. The variation of the electrical resistance may be picked up by a Wheatstone circuit. Assuming that the physical properties of the strain gauge, like its length and specific resistance, are known, the elongation may be calculated according to

$$l = \sqrt{\frac{RV}{\rho}} \tag{5.8}$$

where R is the resistance, V the wire volume and ρ the specific resistance of the strain gauge. From the elongation of the strain wire, the strain, as defined by $\varepsilon=\Delta L/L$, can be calculated using equation 5.8

$$\varepsilon = \sqrt{\left(\frac{\Delta R}{R}+1\right)} - 1 \tag{5.9}$$

The analysis of the measurements rely on the assumption that the existing stress state in the material is known and that it is of a well defined form. In

the analysis of the measurements, a biaxial stress state being constant over the depth of the hole is assumed.

To derive the strain relaxation of an introduced hole in a stress field, first a uniaxial stress field is considered. For the stress components in uniaxially stressed material, σ_r, σ_θ and τ_r, expressions can be derived as in equations 5.10, with α being defined as in figure 5.12 and σ_x the uniaxial stress state. The expressions for the stresses are given by the unprimed expressions.

$$\begin{aligned}
\sigma_r &= \frac{\sigma_x}{2}(1+\cos 2\alpha) & \sigma_r' &= \frac{\sigma_x}{2}\left(1-\frac{1}{r^2}\right)+\frac{\sigma_x}{2}\left(1+\frac{3}{r^4}-\frac{4}{r^2}\right)\cos 2\alpha \\
\sigma_\theta &= \frac{\sigma_x}{2}(1-\cos 2\alpha) & \sigma_\theta' &= \frac{\sigma_x}{2}\left(1+\frac{1}{r^2}\right)-\frac{\sigma_x}{2}\left(1+\frac{3}{r^4}\right)\cos 2\alpha \qquad (5.10) \\
\tau_r &= \frac{-\sigma_x}{2}\sin 2\alpha & \tau_r' &= \frac{-\sigma_x}{2}\left(1-\frac{3}{r^4}+\frac{4}{r^2}\right)\sin 2\alpha
\end{aligned}$$

When a hole is introduced in the material the stress components transform into the primed expressions given in the second part of equations 5.10 [21]. The stress relaxation upon introducing a hole in the material is found by subtracting the initial stresses from the stresses after the introduction of a hole in the material. Using Hooke's law, and assuming that the material is

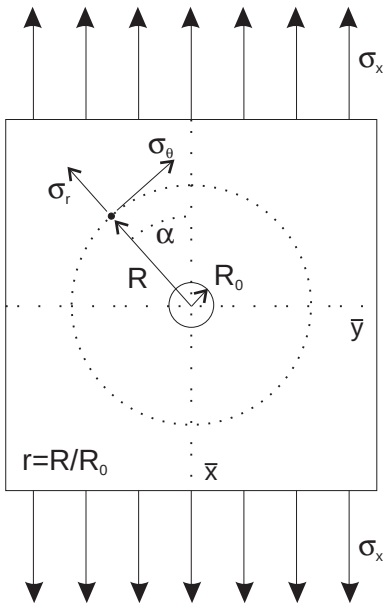

figure 5.12: *Definition of directions in the hole relaxation measurements.*

isotropic in its mechanical properties and exhibits linear elastic behaviour, expressions for the radial and tangential strains may be derived, as in equations 5.11.

$$\begin{aligned}\varepsilon_r &= \sigma_x(A + B\cos 2\alpha)\\ \varepsilon_\theta &= \sigma_x(-A + C\cos 2\alpha)\end{aligned} \tag{5.11}$$

where A, B and C are determined by the materials constants and the distance of measurement relevant to the radius of the introduced hole, being defined as

$$\begin{aligned}A &= \frac{-(1+\nu)}{2E}\frac{1}{r^2}\\ B &= \frac{-(1+\nu)}{2E}\left(\frac{4}{1+\nu}\frac{1}{r^2} - \frac{3}{r^4}\right)\\ C &= \frac{-(1+\nu)}{2E}\left(\frac{-4\nu}{1+\nu} + \frac{3}{r^4}\right)\end{aligned} \tag{5.12}$$

For a biaxial stress field, similar equations can be used as for the uniaxial stress field. Converting the uniaxial solution to the biaxial solution is done using the superposition principle. The expressions for the strain, equations 5.11, will not differ if the applied stress in figure 5.12 is rotated over 90 degrees, that is, if the uniaxial applied stress is in the y-direction. The relieved strain upon introducing a hole in a biaxially stressed material, is now given through the superposition of the relaxation strains due to the x and y applied uniaxial strains. This may be expressed as

$$\begin{aligned}\varepsilon_r &= A(\sigma_x + \sigma_y) + B(\sigma_x - \sigma_y)\cos 2\alpha\\ \varepsilon_\theta &= -A(\sigma_x + \sigma_y) + C(\sigma_x - \sigma_y)\cos 2\alpha\end{aligned} \tag{5.13}$$

These strains are plotted in figure 5.13 as a function of r and α. In the measurements only radial strain relaxations are determined. This leaves only ε_r in equations 5.13. Since there are three unknown entries in equation 5.13, three independent measurements of radial strain relaxations are to be performed. This is done by locating the hole in the centre of a circle, where at the radius of the circle three strain gauges are positioned, at 0, 90 and 225 degrees, as is schematically depicted in figure 5.14. The strain measured, as

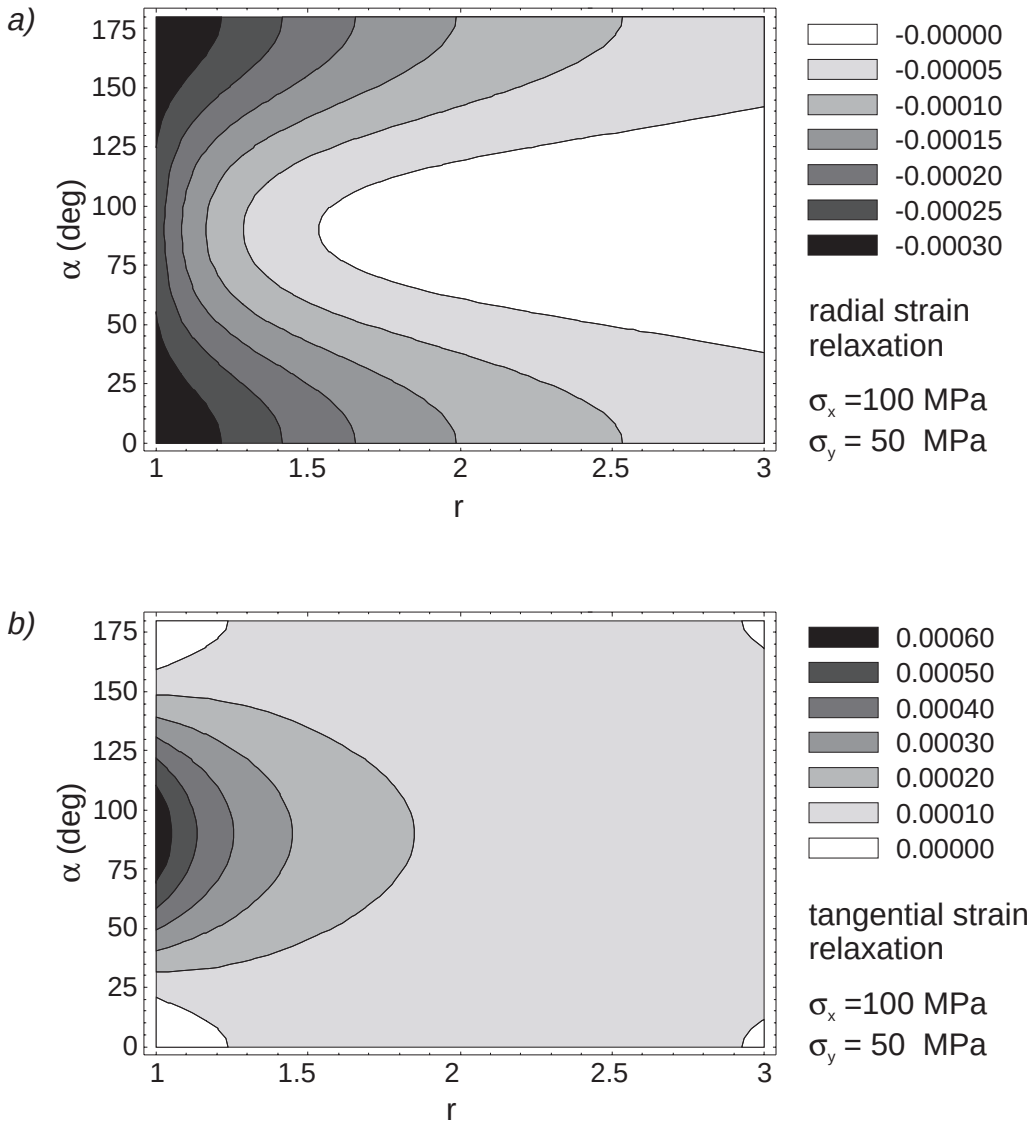

figure 5.13: *Calculated strain relaxations in the hole relaxation measurements. The strain relaxations are plotted as a function of radial distance r and angular direction α.*
a) radial strain relaxation
b) tangential strain relaxation

an example, by strain gauge 2, located at 90 degrees, can be described by equation 5.13 if the term $cos(2\alpha)$ is replaced by $cos(2(\alpha+90°))=-cos(2\alpha)$. Finally, three independent expressions containing σ_x, σ_y and α are derived from which the unknowns may be determined. They are given by the following set

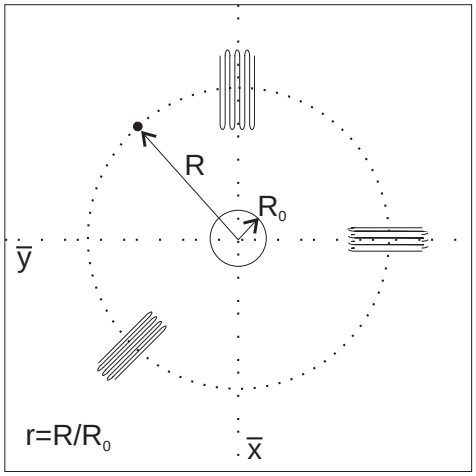

figure 5.14: *Schematic picture of the strain rosettes used.*

of equations, in which the entries ε_1, ε_2 and ε_3 represent the measured strain relaxations by the subsequent strain gauges.

$$\sigma_{max} = \frac{\varepsilon_1 + \varepsilon_3}{4A} - \frac{\left((\varepsilon_3 - \varepsilon_1)^2 + (\varepsilon_3 + \varepsilon_1 - 2\varepsilon_2)^2\right)^{\frac{1}{2}}}{4B}$$

$$\sigma_{max} = \frac{\varepsilon_1 + \varepsilon_3}{4A} + \frac{\left((\varepsilon_3 - \varepsilon_1)^2 + (\varepsilon_3 + \varepsilon_1 - 2\varepsilon_2)^2\right)^{\frac{1}{2}}}{4B} \qquad (5.14)$$

$$\tan 2\alpha = \frac{\varepsilon_1 - 2\varepsilon_2 + \varepsilon_3}{\varepsilon_3 - \varepsilon_1}$$

where α is by definition the angle between strain gauge 1 and the direction of the nearest principal axis.

5.3.2 Experiments

The hole relaxation method is used as an alternative stress analysis method in addition to the x-ray diffraction stress measurements. Stresses are determined at the top surface of the specimen using a strain rosette as depicted in figure 5.14. At the centre of the rosette a hole is introduced which causes existing stress fields to relax, according to equations 5.10. Since the aforementioned derivation of strain relaxations due to the introduction of a hole are based on a hole through the material, they have to be tailored for the

case a blind hole is introduced. Introducing a blind hole into a stress field, however, produces a complex local stress state. In literature it is demonstrated that the stress redistribution for the blind hole case is closely related to the stress redistribution in the case of a through-hole, although the coefficients A and B need to be modified [22].

The coefficients are for the blind-hole case not only a function of r, α and the material properties, but they also depend upon the depth of the hole Z. Since the modified coefficients $\bar{A}$ and $\bar{B}$ can not be derived analytically, they are determined experimentally for every geometry of strain rosettes. This is justified since $\bar{A}$ and $\bar{B}$ are geometric functions and therefore similar for geometrically equivalent cases. The specific material dependence of both functions may be tackled by introducing two new coefficients:

$$\bar{a} = -\frac{2E\bar{A}}{1+\nu} \quad \text{and} \quad \bar{b} = -2E\bar{B} \tag{5.15}$$

Experimental calibration of the rosettes exists of measuring the rosette strain as a function of applied load, before and after drilling. For every rosette geometry, material independent coefficients $\bar{a}$ and $\bar{b}$ are supplied which are to be used in the experimental determination of residual stress fields using the hole relaxation method.

Introduction of holes in the material is a critical step in the hole relaxation method. The theory on which the conversion from measured strains to existing stress fields is based, assumes the holes introduced in the material to be of cylindrical shape. The walls of the hole need to be straight and the floor flat. Furthermore, the introduction of a hole is assumed not to introduce stresses itself. This latter assumption is the most critical one, especially when determining residual stress fields in materials in which holes are hard to introduce, e.g. hard metals or ceramics.

Several techniques for the introduction of holes in materials are evaluated in literature, ranging from simple high speed drilling, spark erosion to air abrasive techniques. This last technique employs abrasive particles being blasted on the material using high speed air nozzles, to remove material locally and with stresses induced as little as possible. Spark erosion delivers well defined holes in the material, exhibiting flat walls and floors, but is only applicable to conducting materials.

For the introduction of holes in the ceramic pellets, use is made of a high speed drill with a diamond bit. In order not to induce thermal stresses and to lubricate the drill hole, the drill is cooled using drilling oil. The diameter of the drill is $1.9 \cdot 10^{-3}$m and the hole is drilled to a depth of $1.0 \cdot 10^{-3}$m. The strain rosette is carefully attached at the homogeneous side of the pellet to the surface of the material. The bonding between surface and strain rosette need to be rigid because upon relaxation of the material the strain gauges have to relax in a similar way.

Before drilling the hole the read-out of the strain gauges is balanced to zero. After drilling the hole the strains are read out. The three different strains, measured by the 0°, 90° and 225° strain gauges, respectively, are listed in table 5.4

table 5.4: strain measurements

ε_1 (10^{-6})	ε_2 (10^{-6})	ε_3 (10^{-6})
-8	-22	-14

The strains are converted to stresses, assuming a biaxial stress field using equations 5.14 and the reduced constants $\bar{a}$ and $\bar{b}$ as defined by equation 5.15. The corrections, for drilling a blind hole, are performed according to calibration graphs supplied with the strain rosettes for the geometry used. Furthermore, the materials constants for the ceramic material are taken as E=350 GPa and ν=0.21. The derived values for the residual stress in the pellet are listed in table 5.5

table 5.5: residual stresses

σ_{max} (MPa)	σ_{min} (MPa)	α (°)
28.8	9.4	-37

5.3.3 Discussion

The values for the residual stresses in the homogeneous phase of the pellet material derived with the hole relaxation measurements do correspond to values obtained with finite element calculations and x-ray diffraction data. With finite element calculations, residual stress fields are determined as described in section 3.2.3. The residual stress components determined are listed in table 5.6.

table 5.6: FEM residual stress values

σ_{axial} (MPa)	$\sigma_{tangential}$ (MPa)	σ_{radial} (MPa)
0.0	36	36

It is seen from the table that the derived residual stress values using the hole drilling method technique show deviations compared to the finite element calculations, based on the difference in thermal expansion coefficients. This effect may be an indication that the difference in thermal expansion is not the only contribution to the residual stress fields in the pellets and that differential densification in the pellets do influence the residual stress fields.

The residual stress values obtained using x-ray diffraction residual stress analysis at similar locations in the specimen as for the hole relaxation method, are listed in table 5.7. In this table several values are given measured at positions along a radial line, with every point measured spaced 1 mm from the former measurement.

table 5.7: x-ray residual stress values

$\sigma_{tangential}$ (MPa)	σ_{radial} (MPa)
16±4	21±5
20±4	18±4
30±5	26±4
29±5	26±5
37±4	22±4

The x-ray residual stresses in the pellets exhibit similar behaviour as the hole relaxation method. The maximum stress measured using the hole drilling method corresponds to the average x-ray diffraction derived stress value. The minimum stress measured using the hole drilling method does however deviate from the x-ray derived stress values. From the finite element calculations, the radial and tangential stress components are expected to be of similar magnitude, which is also to be expected from the fact that the pellets are stressed biaxially. From linear elasticity, for a plate without a hole at the origin, only one case of stress distribution symmetrical with respect to the axis may exist, namely that when $\sigma_r=\sigma_\theta$=constant and the plate is in a condition of uniform tension or uniform compression in all directions in its plane.

It is thus shown that the hole relaxation method as well as x-ray diffraction stress measurements deliver comparable results for the existing residual stress state in the surface layers of the specimen and are consistent with the finite elements calculations.

5.4 Residual stress fields in thin ceramic layers

Introduction

In the formation of sol-gel ceramic layers, stresses may build up in the spinning stage, the drying stage and the consolidation stage. As already elaborated in section 4.3, the stresses depend heavily on the morphology of the layers in the various stages and the processing conditions. The processing of the layers, however, may have other impacts on the final structure and morphology of the layers. X-ray analysis is used as a tool to study crystallisation, grain growth, phase transformation and the evolution of residual stress fields in the thin ceramic layers.

5.4.1 Experimental procedures

The sol-gel derived thin ceramic layers as described in section 4.3 have experienced different curing treatments. Not only the method which is used to supply the energy for densification, e.g. laser or furnace curing, is a parameter in the curing process, but also other parameters governing the densification process are varied. For the furnace cured specimen the parameters dictating the densification process are curing temperature and time. The laser curing process is governed by the laser intensity and the interaction time. To investigate the impact which the several parameters have on the final properties of the layer, furnace as well as laser cured specimen are studied using x-ray diffraction. Especially, residual stress analysis and phase analysis is performed on a set of differently processed sol-gel derived thin TiO_2 layers.

X-ray diffractograms are made from the TiO_2 specimen using the θ–2θ goniometer set-up. Since the diffraction yield of the thin layers is low, no reflections are found for large values 2θ. To study crystallisation processes and phase transformations in the nano-crystalline material, diffractograms are recorded over a 2θ range in which the main reflections for crystalline TiO_2 are expected. The diffractograms are recorded from 2θ=21.0° to 2θ=29.0°.

X-ray residual stress measurements are performed on the TiO_2 layers. There are some basic requirements which a material has to satisfy in order to allow for x-ray residual stress measurements to be performed. The material has to be crystalline and, in order to be able to perform stress analysis using linear elasticity theory, polycrystalline. If the material is monocrystalline, there will only be one orientation ψ for which the Bragg law is satisfied and x-ray residual stress analysis is not possible. If the material exhibits preferred orientation, i.e. the material is textured, x-ray residual stress measurements also may become a problem. When a material is textured to a large extent, Bragg reflections will decrease upon tilting the specimen from its preferred orientation, as for the case of monocrystalline materials. Additionally, texture in a polycrystalline material may cause the material to become anisotropic in its linear properties. Especially for materials which exhibit larger anisotropy in Young's modulus, this may give rise to problems. For a polycrystalline material, which is considered to be isotropic in its macroscopic elastic behaviour, it is not a problem, provided that in the analysis use is made of the *{hkl}* plane specific x-ray elastic constants. For highly textured materials, it may become questionable, since Hooke's law can not be applied any longer.

To check whether the material is textured, the diffraction yield is measured for all orientation ϕ, ψ of crystallites in the specimen. This is done by locating the detector at the 2θ reflection of interest. Subsequently, the specimen is tilted over an angle ψ, as defined by the coordinate system in figure 2.12. Next, for the specific angle ψ, the diffraction yield is measured for all angles of rotation ϕ, as defined in figure 2.12. After measuring the diffraction yield as described for a specific tilt angle ψ, all angles ϕ are measured. Since tilting of a specimen will cause defocus errors in the measured intensity, the measurements are corrected according to calculated defocus patterns. The result of these measurements can be plotted in a contour plot with axes ϕ and ψ. If any preferred orientation is present in the specimen, it will show as poles in the contour plots.

Residual stress measurements are performed using positive as well as negative ψ-tilting for different orientations ϕ of the specimen. The aim of this extensive set of orientations is to check whether the residual stress state in the material is triaxial. If no triaxial stress state is present, it would suffice to measure only positive or negative ψ angles for only one orientation ϕ of the specimen and analyse the measurements using the $sin^2\psi$ method, as

described in section 2.4.4. Otherwise, analysis of the stress state using triaxial stress analysis is required.

5.4.2 Crystallisation and phase analysis

X-ray diffractograms are recorded for furnace as well as laser cured specimens. The experiments are performed using a Philips PW1820 goniometer. A divergence slit of 1/6° and soller slits are present at the primary optics side, at the secondary optics side a receiving slit of 0.2 mm, an anti-scatter slit of ½°, soller slits and a monochromator are installed. In figure 5.15 the recorded diffractograms for the furnace cured specimen are displayed.

From the recorded diffractograms, several properties of the layers may be observed. The diffractogram of the 300°C cured specimen does not show any Bragg reflections. This indicates that the material does not contain crystallites which are in a suitable position for diffraction, e.g. they do not satisfy the Bragg law for diffraction. This may lead to two explanations. Either the layer is highly textured and the reflections can not be measured using the θ–2θ set-up, or the layer is amorphous. To draw accurate conclusions concerning

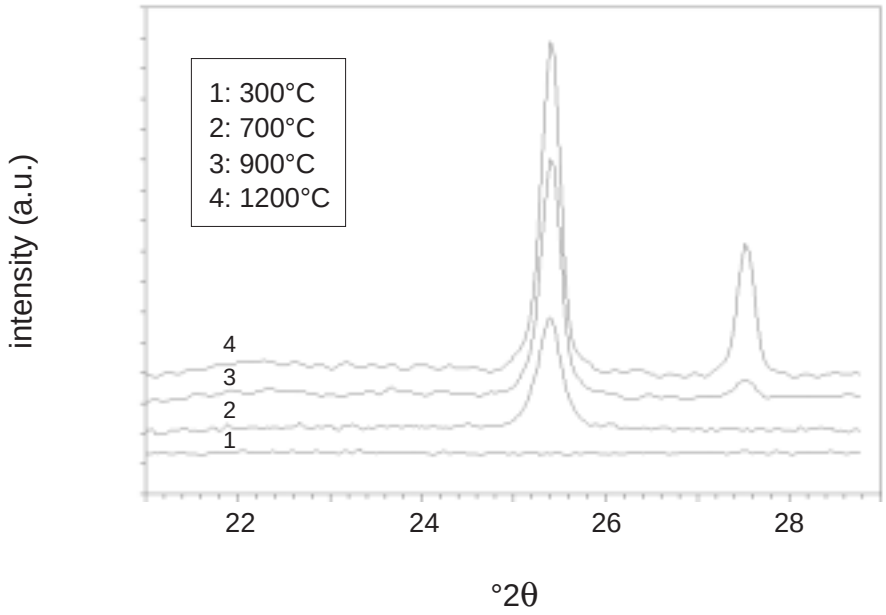

figure 5.15: *Determined x-ray diffractograms for the furnace cured thin TiO_2 layers. From the displayed diffractograms information on crystallisation, grain growth and phase transformation may be obtained.*

the morphology of the layer, the remaining specimen will be examined first. If the curing temperature is increased, a reflection is emerging as may be observed for the 700°C cured specimen. This emerging reflection indicates that, in contrast to the 300°C cured specimen, there are crystallites in a preferred orientation for diffraction. The 2θ value of this reflection, 25.28°, can be transformed using equation 2.5 to a lattice spacing of $d=3.52\cdot10^{-1}$nm, which corresponds to the lattice distance of the *{101}* planes of anatase, the low temperature tetragonal phase of TiO_2 [23,24].

Upon further increasing the curing temperature to 900°C, the anatase reflection at 25.28° 2θ becomes more pronounced, indicating that the layer becomes more crystalline. As an additional effect of the increased curing temperature, a second reflection is observed at 27.44° 2θ. This reflection is due to a lattice set with spacing $d=3.247\cdot10^{-1}$nm and corresponds to the *{110}* planes of the rutile phase of TiO_2. This means that the layer is partly transformed from the low temperature phase, anatase to the high temperature rutile phase. For bulk materials this transition is expected around 750°C [25,26].

Finally, a diffractogram of a specimen cured at 1200°C is displayed. The anatase reflection has increased even further. The rutile reflection has become also very distinct. Together, it can be concluded that the layer has become even more crystalline and that more crystallites are transformed from the anatase phase to the rutile phase.

The recorded diffractograms do not only provide information concerning the phase of the material. From the width of the determined line profiles more information may be gained. For a lattice set *{hkl}* with specific lattice spacing d the exact value θ_b can be calculated which satisfies Bragg's law for diffraction. At the angle $2\theta_b$, rays diffracted by top planes in a crystallite are completely in phase with rays diffracted at the bottom planes in a crystallite. If the angle θ is such that the difference in path length for rays scattered by the first plane and second plane is a quarter of a wavelength, destructive interference will not occur. However, the path difference between rays scattered by the first and the third plane is half a wavelength and, as a consequence, destructive interference will occur. Similarly, rays scattered by the second and fourth planes are completely out of phase. This means that for an infinitely large crystal, for every angle $\theta\neq\theta_b$ scattered rays will interfere destructively. If small crystals are considered, the plane, scattering a ray exactly out of phase with the ray from the first plane may not exist, due to

the small crystal size. Very small grains will thus cause line profiles to broaden. The measured profile is a superposition of all the profiles scattered by the crystallites, where their position is governed by the local strain, and their shape by the size of the crystallites. From the measured line profiles, the average crystallite size can be determined using the Scherrer equation [27]

$$D = \frac{K\lambda}{B\cos\theta_B} \tag{5.16}$$

where K is a factor ~0.9-1.0, λ the wavelength of the radiation used and B the broadening of the profile. The broadening B has to be corrected for instrumental broadening due to slit sizes and x-ray source characteristics. To measure the instrumental broadening, a reference diffractogram is recorded from a standard specimen. This specimen is not allowed to broaden the line profiles, therefore, the crystallite size should be larger than ~1.0 μm and the grains should not be strained.

As a standard specimen, silicon powder is used with grain sizes of ~5.0 μm. Using similar experimental settings as for the recorded diffractograms of the TiO_2 layers, the *{111}* reflection of silicon at 28.442°*2θ* is recorded. From this line profile, the determined instrumental line broadening is B=0.09°*2θ*. Using this value for the instrumental line broadening and the broadening as determined from the profiles in figure 5.18, an estimate for the average crystal size in the layers is given in table 5.8.

table 5.8: average crystallite sizes furnace cured TiO_2 specimen

temperature (°C)	broadening (°2θ)	average grain size (nm)
300	-	-
700	0.241	53.9
900	0.172	99.3
1200	0.137	173.3

The values listed in the table correspond to the values derived in section 4.3, which are derived using the line intercept method on micrographs obtained using scanning electron microscopy.

To investigate the crystalline properties and the phase of the laser cured specimen, diffractograms are recorded using similar settings which were

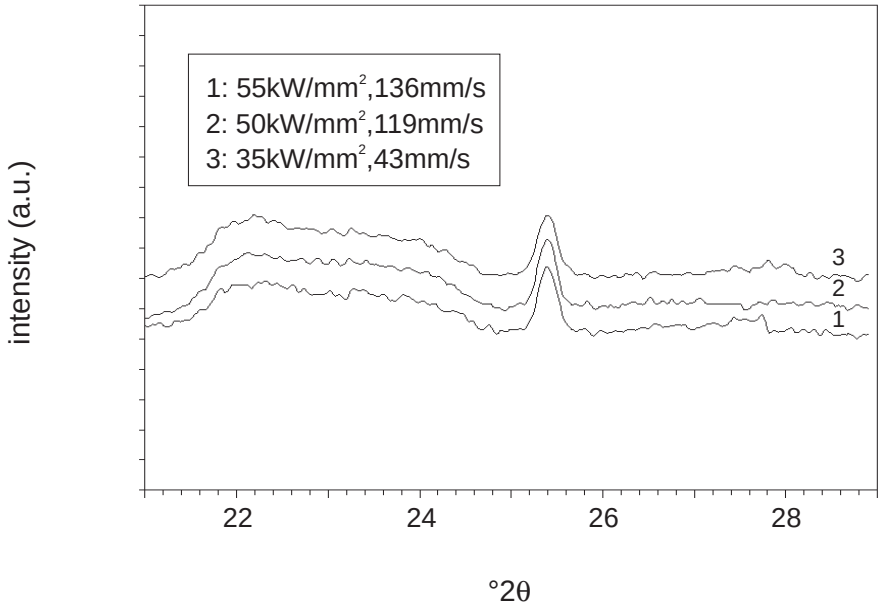

figure 5.16: *Determined x-ray diffractograms for the laser cured thin TiO_2 layers. The various laser experiments have had similar impact on the TiO_2 layers.*

used for the furnace cured specimen. In figure 5.16 three diffractograms are depicted for laser cured specimen with different curing parameters.

The three diffractograms exhibit similar behaviour, indicating that the phase and structure of the layers are comparable. In contrast to the furnace cured specimen, there is no evolution in crystallisation and the transformation from anatase to rutile is, only faintly observable for the specimen which is cured using laser parameters 55 kW/mm^2, 136 mm/s, not observed. Overall, the diffraction yield is small, compared to the furnace cured specimen. To perform x-ray residual stress measurements accurately, the intensity of the reflection under investigation has to be ~10 times the background. The intensity drops heavily upon tilting of the specimen, which makes it not possible to perform residual stress measurements on these layers.

To get some insight in the morphology of the laser cured layers, the width of the profiles is determined. From this width, average crystallite sizes in the laser cured layers are determined according to equation 5.16. The derived values are listed in table 5.9.

table 5.9: average crystallite sizes laser cured specimen

laser (kW/mm^2, mm/s)	broadening (°2θ)	average grain size (nm)
35, 43	0.185	85.7
50, 119	0.215	65.1
55, 136	0.190	81.4

The average crystallite sizes does not deviate to a large extent, indicating that grain growth is not affected by the laser settings used in these experiments. The determined average crystallite sizes are again in good agreement with the determined crystallite sizes in section 4.3.1 using scanning electron microscopy.

5.4.3 Texture measurements

As discussed before, to perform x-ray residual stress measurements on a polycrystalline material, it is necessary to know what the structure of the material is. To investigate whether preferred crystal orientations exist in the thin ceramic layers, the diffraction yield as a function of all crystallite orientations is determined.

The measurements are performed on the Philips X'Pert MRD system, operating in a texture analysis mode. The x-ray source is mounted to deliver a point focus beam. At the primary optics side a cross slit collimator is installed, at the secondary optics side a wide receiving slit, 0.2 mm, is installed. No soller slits and no filters are used.

For the 1200°C specimen, a contour plot is measured for the *{101}* anatase reflection at 2θ=25.28°. The tilt angle ψ is varied from 0° to 45° and ϕ ranged from 0° to 360°. At every crystal orientation, the diffraction yield is measured during 5 seconds. Afterwards, corrections are made for defocusing effects. The determined contour plot is displayed in figure 5.17.*a.* The measurements indicate that there is not a distinct preferred orientation present. For ψ tilts ranging from ~10°-30°, the intensity measured is constant, with some areas with increased diffraction yield. For specific ϕ orientations, 0°, 90°, 180°, 270°, a slight increase in intensity can be observed, indicating that more crystals are oriented in this orientation.

For the 900°C specimen a contour plot is measured using a similar procedure as for the 1200°C specimen. The result is displayed in figure 5.17.*b*. The

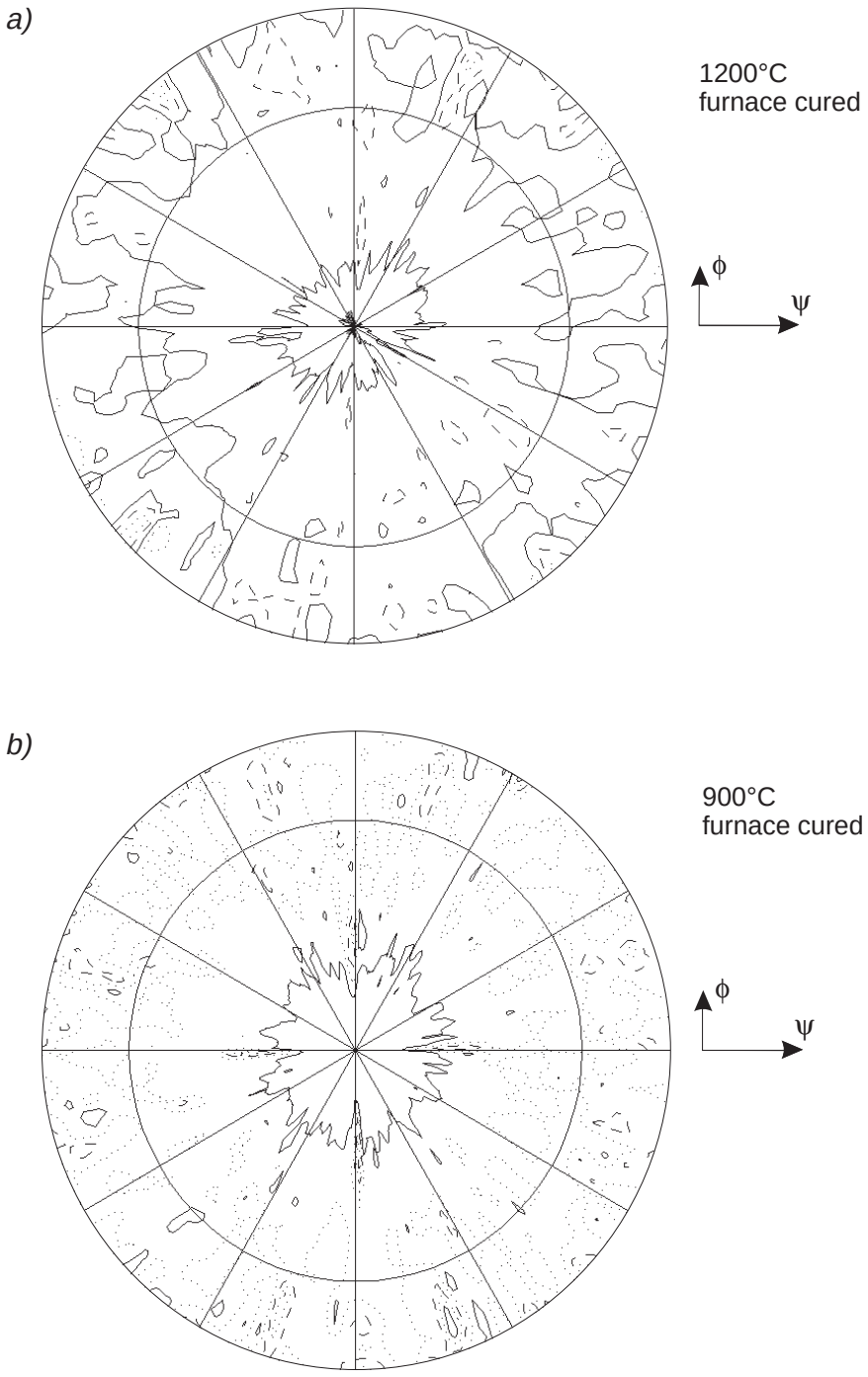

figure 5.17: *Pole figures for the 1200°C and 900°C specimen. The measured intensity of the 2θ=25.28° reflection is measured as a function of tilt angle ψ, plotted radially, and azimuthal angle ϕ.*

contour plot exhibits comparable features as the contour plot determined for the 1200°C specimen. The determined intensity as a function of ψ is constant over a large range of ψ values. An increase in diffraction yield is again observed, as for the 1200°C specimen, for specific crystallite orientations ϕ=0°, 90°, 180°, 270°. The magnitude of these poles in the contour plots is for the 900°C specimen slightly larger than for the 1200°C specimen. The 900°C specimen has experienced the curing temperature twice as long, 60 minutes versus 30 minutes for the 1200°C specimen, which may be an explanation for the more pronounced preferred orientation in this specimen.

From the contour plots it is concluded that x-ray diffraction can be used to measure residual stress fields in these specimen. The layers contain crystallites randomly oriented, a first requirement for application of x-ray residual stress analysis.

5.4.4 X-ray residual stress measurements

X-ray residual stress measurements are performed on the furnace cured TiO_2 specimen. From the phase analysis experiments and the texture measurements these layers appear adequate to perform x-ray residual stress measurements accurately.

First the 1200°C specimen is studied. The anatase reflection at 25.28° 2θ proved in the phase analysis experiments to exhibit an intensity versus background ratio which is large enough for x-ray residual stress analysis to be performed. For the stress measurements, the tube is mounted to deliver a point focus beam, at the primary optics side a crossed slit collimator is used to adjust the spot size on the specimen. At the secondary optics side a wide receiving slit, 0.2mm, is installed to maximise diffraction yield. The position of the Bragg reflection at 25.28° 2θ is determined as a function of crystallite orientations ϕ, ψ. For three azimuthal angles, ϕ=0°, 45° and 90°, the tilt angle ψ is varied from -45° to 45° in steps $\Delta sin^2\psi$=0.12. The results of the measurements are displayed in figure 5.18. For the different azimuthal angles ϕ, an offset is added to the measured values for clarity. From the measurements it is seen that the dependence of the lattice spacing upon the crystallite orientation is linear, which is expected for linear elastic isotropic media. For the larger ψ values however, the lattice spacings measured for positive and negative ψ values do show some deviations. This may be due to the existence of shear components in the strain tensor. From equation 2.13 it is seen that if ε_{13} and ε_{23} are non-zero, an extra contribution to the measured

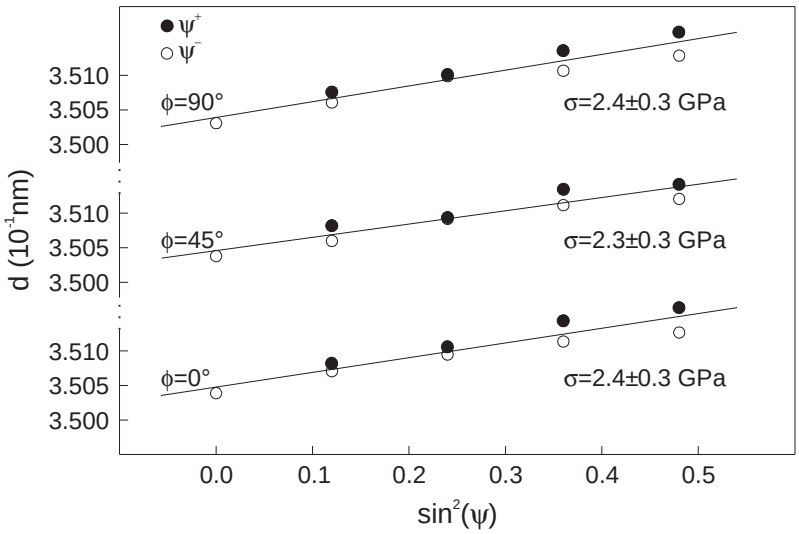

figure 5.18: *Determined lattice spacings for the 1200°C furnace cured specimen as a function of specimen tilt ψ in azimuthal orientations ϕ=0,45 and 90°.*

strain is expected, which differs for positive and negative values of ψ due to the term *sin(2*ψ*)*. To investigate whether the stress state in the layer is triaxial, a procedure is followed which enables the separation of the contributions from the several strain components on the measured lattice strains [28].

If for an orientation ϕ the average lattice strain ε_{avg} is calculated from the measured values d^+ and d^-, the following expression may be derived

$$\begin{aligned}\varepsilon_{avg} &= \frac{d_{\phi\psi^+} + d_{\phi\psi^-}}{2d_0} - 1 = \frac{1}{2}\left\{\frac{d_{\phi\psi^+} - d_0}{d_0} + \frac{d_{\phi\psi^-} - d_0}{d_0}\right\} \\ &= \left\{\varepsilon_{11}\cos^2\phi + \varepsilon_{12}\sin 2\phi + \varepsilon_{22}\sin^2\phi - \varepsilon_{33}\right\}\sin^2\psi + \varepsilon_{33}\end{aligned} \tag{5.17}$$

From 5.17 it is seen that plotting ε_{avg} as a function of $sin^2\psi$ delivers a straight line. Measuring ε_{avg} for azimuthal angles ϕ=0°, 45°, 90° yields a set of equations from which the strain components ε_{11}, ε_{12}, ε_{22}, ε_{33} may be determined. A similar procedure may be followed to determine the shear strains ε_{13} and ε_{23}. By taking the difference between the measured lattice strains for positive and negative ψ values, an expression may be derived which correlates the shear strains to the crystallite orientation ϕ.

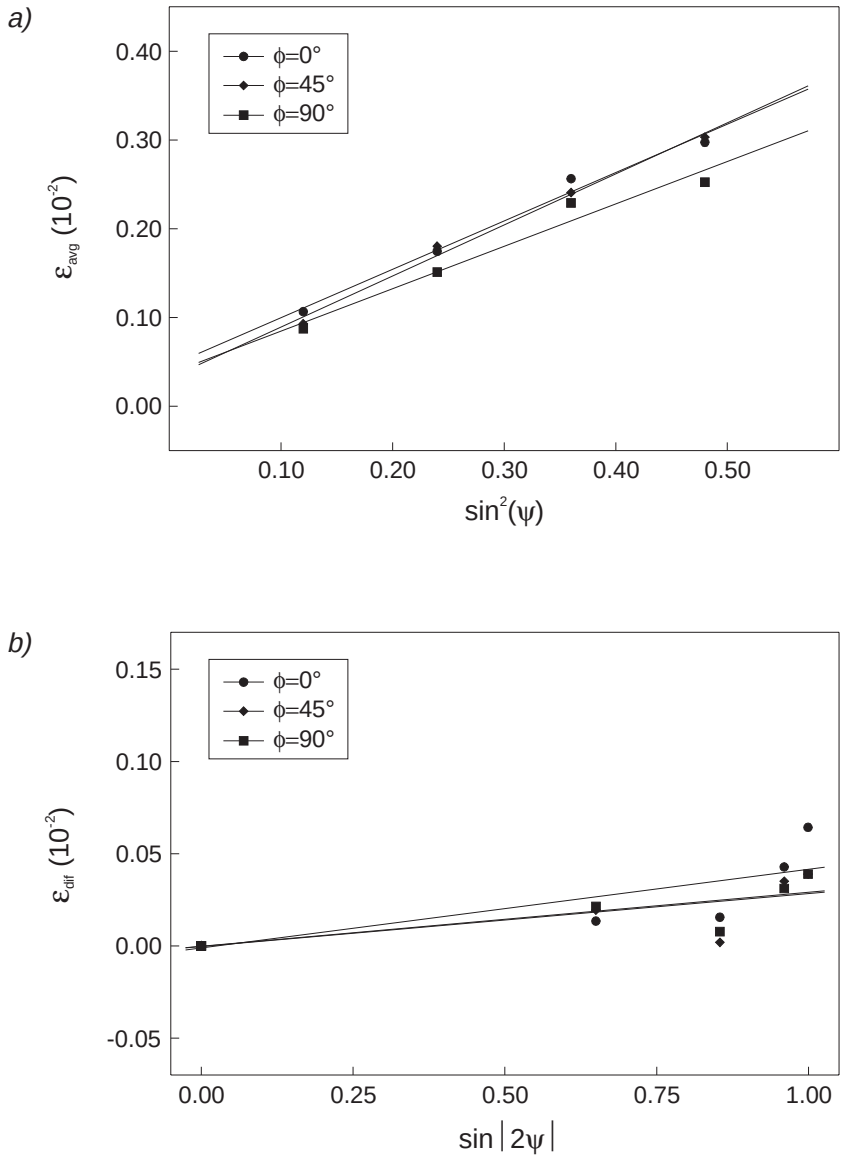

figure 5.19: *Determination of triaxial strain.*
a) Evaluation of the average lattice spacing, as defined by equation 5.17, as a function of specimen tilt ψ.
b) Evaluation of the differential lattice spacing, as defined by equation 5.18, as a function of specimen tilt ψ.

$$\varepsilon_{dif} = \frac{d_{\phi\psi^+} - d_{\phi\psi^-}}{2d_0} = \{\varepsilon_{13}\cos\phi + \varepsilon_{23}\sin\phi\}\sin|2\psi| \qquad (5.18)$$

Plotting ε_{dif} against $sin|2\psi|$ for azimuthal angles ϕ=0°, 90° delivers the shear strains ε_{13} and ε_{23} from the gradient of the derived line. In figure 5.19 the

dependence of ε_{avg} on $sin^2\psi$ and the dependence of ε_{dif} on $sin|2\psi|$ are plotted, respectively, for the three different azimuthal orientations used.

From figure 5.19.*a* it is seen that ε_{avg} is linear with $sin^2\psi$. As an example, for the azimuthal direction ϕ=90°, the gradient of the line delivers a value, according to equation 5.17, for $(\varepsilon_{22}-\varepsilon_{33})$, the intercept with the $sin^2\psi$=0 axis delivers an expression for ε_{33}. The gradient of ε_{dif} versus $sin|2\psi|$ in figure 5.19.*b* readily delivers a value for the shear strain ε_{23}. Calculating the slopes and intercepts for the remaining two azimuthal angles 0° and 45° finally delivers a set of equations from which the strain tensor can be derived. The results of the measurements are listed in the following matrix:

$$\text{measured strains}: \quad \begin{pmatrix} 5.8 & -0.8 & 0.08 \\ - & 6.1 & 0.6 \\ - & - & 0.3 \end{pmatrix} \bullet 10^{-3}$$

The derived values for the strain components indicates that a biaxial strain field exists in the layer. The values for ε_{11} and ε_{22} are overall ~10 times larger than the other strain components, where the measured shear strain components ε_{13} and ε_{23} are small compared to the principal strains ε_{11} and ε_{22}. Assuming that the material is isotropic in its linear properties, the presence of a biaxial strain state indicates that the stress state is also biaxial. Therefore, application of the $sin^2\psi$ method, as discussed in section 2.4.4 is justified to measure residual stresses in these layers.

Application of the $sin^2\psi$ method to determine the residual stresses in the 1200°C specimen delivers the values listed in table 5.10. In the analysis, the material properties of TiO_2 are used according to E=410 GPa, ν=0.19.

table 5.10: measured stress 1200° specimen

ϕ (°)	σ_ϕ (GPa)
0	2.4±0.3
45	2.3±0.3
90	2.4±0.3

The values determined for the orientations ϕ are comparable within the error margins, indicating that the stress state is biaxial and, from equation 2.15, it

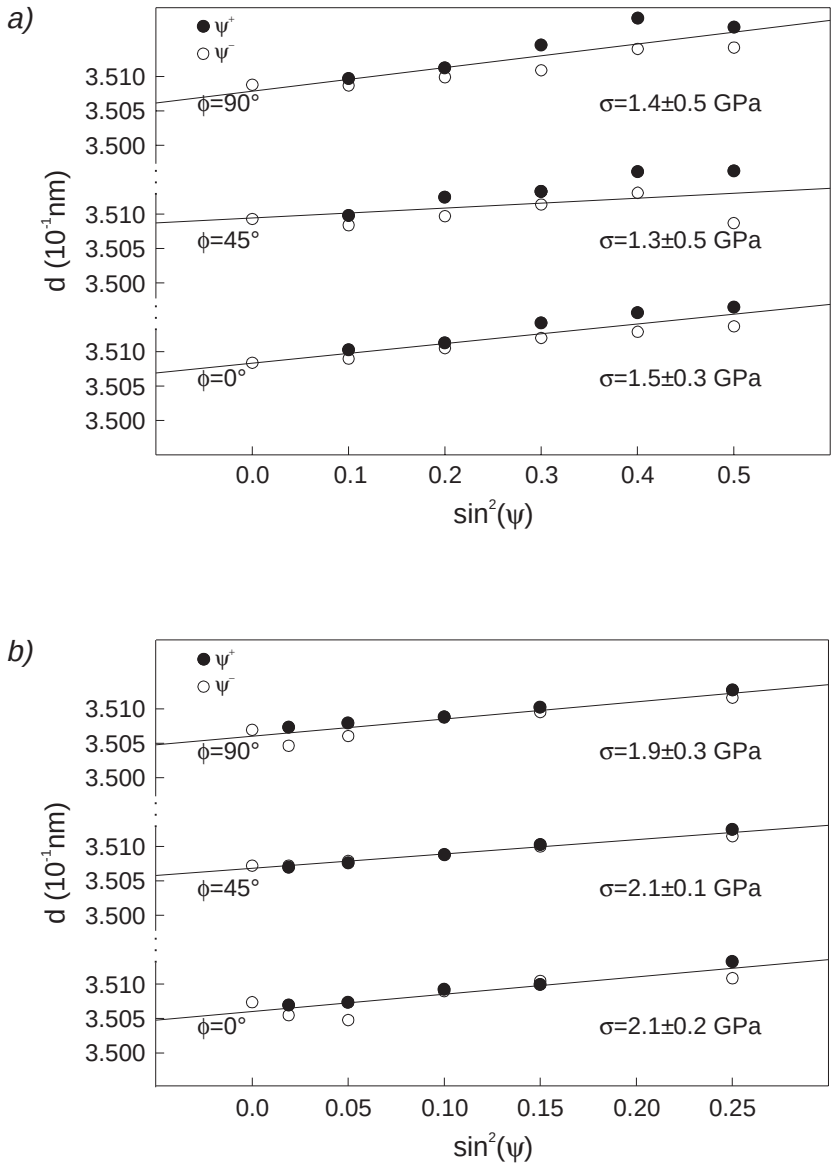

figure 5.20: *Stress measurements 700°C and 900°C furnace cured specimen.*
a) Determined lattice spacings for the 700°C furnace cured specimen as a function of specimen tilt ψ in azimuthal orientations ϕ=0,45 and 90°.
b) Determined lattice spacings for the 900°C furnace cured specimen.

also follows that $\sigma_{11}=\sigma_{22}$, determining the value σ_{ϕ}. Consequently, an averaged residual stress value is derived for the 1200°C specimen, σ_{res}=2.4±0.2 GPa. The sign of the derived stress is positive, the stresses in the layer are thus of tensile character.

Similar experiments are conducted for the 700°C and the 900°C specimen. The results of these measurements are plotted in graphs 5.20. From the graphs, similar behaviour as for the 1200°C can be observed for both the 700°C and the 900°C specimen. With use of the $sin^2\psi$ method, the residual stresses in the layers are analysed. For the material properties, the values used for the 1200°C specimen are substituted. The measurements are again averaged, since no discrepancies are found between the measured stresses as a function of azimuthal orientation ϕ. The eventually determined residual stress states in the layers are listed in table 5.11.

table 5.11: experimentally derived stresses in layers

curing temperature (°C)	σ_{res} (GPa)
700	1.4±0.2
900	2.0±0.1
1200	2.4±0.2

5.4.5 Discussion

The thin TiO_2 layers proved to exhibit large differences in morphology, structure and residual stress state between dissimilar curing processes. For the various curing temperatures an evolution in phase is observed. The 300°C specimen is still amorphous after the curing process. Since this specimen does not exhibit any Bragg reflection, due to the amorphous state of the layer, an average crystallite size can not be determined from line broadening experiments. For the same reason, x-ray residual stress analysis can not be performed on this specimen and the determination of the residual stress state is therefore not possible.

Curing the layer at 700°C results in crystallisation of the TiO_2 layer in the anatase form. This crystallisation typically results in an large compressive stress. The formation of grains in the layer is accompanied by a reduction of stress in the layer due to a volume decrease associated with the grain formation. X-ray line broadening analysis delivers an average grain size in the layer of ~53.9 nm.

Increasing the curing temperature to 900°C and 1200°C results in a phase transformation. The anatase phase is transformed to the rutile phase upon increasing the curing temperature. The resulting film is a mixture of anatase and rutile [29]. This effect is seen from the diffractograms in figure 5.15, for both the 900°C and 1200°C cured specimen a rutile reflection is observed.

X-ray line broadening analysis delivers for the 900°C and 1200°C specimen average grain sizes of ~99.3 nm and ~173.3 nm, respectively. The determined average grain sizes correspond to the derived values using scanning electron microscopy. In the derivation of the average grain sizes from x-ray line broadening, the contribution of second and third order stresses to the broadening is neglected. Since the determined grain sizes correspond well to the scanning electron microscope values, the second and third order stresses are assumed to be small enough to not influence the line profiles.

The measured residual stresses in the layers increase with the curing temperature. Together with the fact that the stresses measured are tensile, this may be an indication that the residual stress state is evolved upon cooling during the curing process. The linear thermal expansion coefficient of the layers and the substrate are ~$(8.0\pm0.5)10^{-6}$ K^{-1} and ~$(0.5\pm0.1)10^{-6}$ K^{-1}, respectively [30,31].

From the difference in thermal expansion coefficients and the temperature difference upon cooling from curing temperature to room temperature, a thermally induced stress may be calculated according to [32]

$$\sigma_{thermal} = \frac{E_l}{1-\nu_l}\int_{T_R}^{T_C} \Delta\alpha dT \qquad (19)$$

In this equation, $\Delta\alpha$ is the difference in thermal expansion coefficients, ΔT is the temperature difference, E_l is Young's modulus of the layer and ν_l its Poisson's ratio. In this equation, the substrate is assumed to be infinitely stiff. Using this expression, the thermally induced stress in the layers may be estimated. The calculated thermal stress values are listed in table 5.12.

table 5.12: thermally induced stress

curing temperature (°C)	σ_{th} (GPa)
700	1.3±0.4
900	1.6±0.5
1200	2.1±0.6

In figure 5.21 the measured residual stress values as well as the calculated thermal misfit induced stresses are plotted versus the curing temperature of the specimen. From the graph it can be seen that the measured residual stress

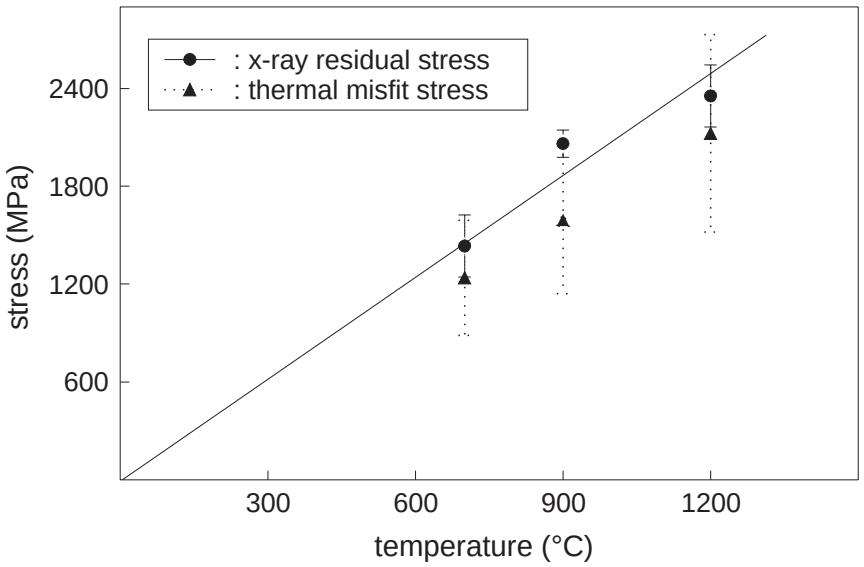

figure 5.21: *Determined residual stresses in the various furnace cured TiO_2 specimen. In the graph, the calculated thermal stress is also depicted.*

values lie within the expected range for thermal misfit induced stresses in the layer. If the stresses however, are not solely due to thermal misfit, then a line may be fitted through the data which is not forced to go through the origin of the graph, the fitted line then intersects the vertical axis at ~300 MPa. This effect may be an indication that the densification stress upon curing of the specimen is ~300 MPa. The main assumption made in this conclusion is that the densification in the three different layers cured at 700°C, 900°C and 1200°C is comparable. If the densification differs for the various curing temperatures, then the densification shrinkage will cause different densification stresses in the various cured layers. The offset in the residual stress versus temperature line will then be non-equal for different curing temperatures, hence fitting a straight line through the points, indicating that the differences in stresses is solely due to thermal misfit, is no longer justified.

Overall it is seen that large stresses may evolve in the curing process, which may be ascribed to the differences in thermal expansion coefficients rather than differences in densification processes.

References

1 P. van Houtte and L. de Buyser, Acta Metall. Mater, **41**, 323, 1993.

2 B.D. Cullity, Elements of x-ray diffraction, Addison-Wesley, Massachusetts, (1978), 447.

3 I.C. Noyan and J.B. Cohen, Residual Stress, measurements by diffraction and interpretation, Springer-Verlag, New-York, (1987).

4 B. Eigenmann and E. Macherauch, Mat.-wiss. u. Werkstofftech., **26,** (1995), 148.

5 B. Eigenmann and E. Macherauch, Mat.-wiss. u. Werkstofftech., **26,** (1995), 199.

6 W. Voigt, Lehrbuchder Kristallphysik, Teubner-Verlag, Berlin, 1928.

7 A. Reuss, Z. für angew. Math. and Mech., **9**, (1929), 49.

8 E. Brinksmeier and H. Siemer, Intern. conf. on residual stresses 2, Elsevier, London, (1989), 335.

9 K. Tanaka, Y. Yamamoto and K. Suzuki, Intern. conf. on residual stresses 2, Elsevier, London, (1989), 328.

10 M. Kurita, Nondestr. Test. Eval., **8-9**, (1992), 681.

11 J.A. Sue, Surf. and Coat. Techn., **54-55**, (1992),154.

12 D. Amos, B. Eigenmann and E. Macherauch, Z. Metallkd., **85**, (1994), 5.

13 Anon., Engineered materials handbook, vol. 4 Ceramics and Glasses, ASM international, (1991), 585.

14 W.G. Sloof, B.J. Kooi, R. Delhez, Th.H. de Keijser and E.J. Mittemeijer, J. Mater. Res., **11**, 1440-57 (1996).

15 S. Timoshenko and J.N. Goodier, Theory of elasticity, McGraw-Hill, New York, (1951), 58.

16 P.Z. Cai, D.J. Green and G.L. Messing, J. Am. Ceram. Soc., **80**, (1997),1929.

17 E.M. Beaney and E. Procter, Strain, **10**, (1974), 7.

18 E.M. Beaney and E. Procter, Strain, **12**, (1976), 99.

19 J-Y Wang, Experimental Mechanics, **28**, (1988), 355.

20 E.E. Gdoutos, I.M. Daniel and H.M. Hsiao, J. of the Mech. Beh. of Mat., **6**, (1995), 21.

21 S. Timoshenko and J.N. Goodier, Theory of elasticity, McGraw-Hill, New York, (1951), 78.

22 N.J. Rendler and I. Vigness, Proc. SESA XXIII, **2**, (1966), 577.

23 I.A. Montoya, T. Viveros, J.M Dominguez, L.A. Canales and I. Schifter, Cat. Lett., **15**, (1992), 207.

24 Y. Takahashi and Y. Matsuoka, J. Mater. Sc., **23**, (1988), 2259.

25 D. Bersani, R. Capelletti, P.P. Lottici, G. Gnappi and A. Montenero, Mat. Sc. Forum, **239**, (1997), 87

26 I. Manzini, G. Antonioli, D. Bersani, P.P. Lottici, G. Gnappi and A. Montenero, J. Non-Cryst. Solids, **192**, (1995), 519.

27 B.E. Warren, X-ray diffraction, Addison-Wesley, Massachusetts, (1969), 253.

28 I.C. Noyan and J.B. Cohen, Residual Stress, measurements by diffraction and interpretation, Springer-Verlag, New-York, (1987), 119.

29 N.J. Hess and G.J. Exarhos, Mat. Res. Soc. Symp. Proc., **356**, 597.

30 Anon., Engineered materials handbook, vol. 4 Ceramics and Glasses, ASM international, (1991), 755.

31 M.F. Ashby, Cambridge Materials Selector, (1993).

32 G. Dreier and S. Schmauder, Scripta Metall. Mater., **28**, (1993), 103.

6 FRACTURE OF THIN CERAMIC LAYERS

Introduction

It is known that during the production of sol-gel layers severe problems may be encountered concerning the final quality of the layers. Especially the formation of cracks in the layers and delamination of the layers are mechanisms by which the layers may fail. In the preceding sections various aspects of the sol-gel derived thin ceramic layers were studied. X-ray residual stress measurements provided insight in the stress state of the ceramic layers, whereas scanning electron microscopy yielded more insight in the morphologies of the layers. Features of the thin layers are governed by, amongst others, the thickness of the films and the stress states present in the films. Whether the films will fracture or delaminate may depend on the film thickness. A film with a larger thickness will delaminate whereas a film with smaller thickness will exhibit crack patterns perpendicular to the interface. Here a model is proposed which describes the crack pattern expected in a layer as a function of its thickness that depends on the porosity as well.

Laser curing of the sol-gel spun layers will result in homogeneous dense layers, provided that an appropriate curing process is selected. Inaccurate laser parameters may result in severe delamination of the layers, as seen in section 4.3. This poor mechanical behaviour of the layers may have its origin in the stress state of the layers. If the stresses in the layer are compressive, the layer may fail in a buckling process, provided that the evolving stresses are large enough. A second cause of the formation of blisters in the layer may be the presence of entrapped liquid in the green layers. Upon heating of the layers, this entrapped liquid expands and cause the layer to blister.

6.1 Fracture of brittle materials

Fracture of materials may be described, from an energy point of view, by the creation of free surfaces from bulk material [1]. For brittle materials, without stress concentrators or plastic deformation, this can be seen by equating the release of strain energy to the energy required for creating a unit area of free surface. The mode of fracture is relevant for the evaluation of the strain energy release rate accompanied by the propagation of a crack. Three modes

of fracture may be identified namely opening mode, sliding mode and tearing mode, as depicted in figure 6.1.

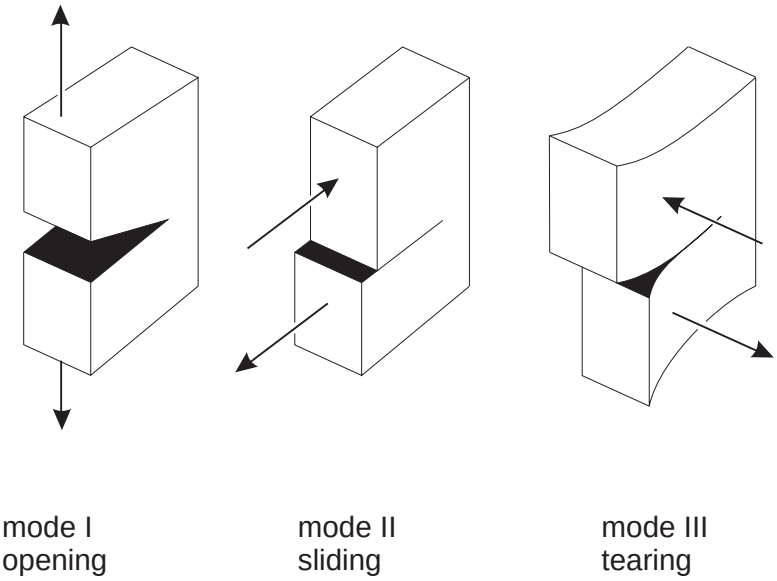

figure 6.1: *Three different fracture modes.*

The stress present at the crack tip, σ_f, depends on the loading mode. In the following, only mode I fracture, opening mode, will be considered. The force two atoms exert on each other corresponds to the negative gradient of the potential, which can be simplified in a pairwise approximation as predicted in figure 6.2. Over the area of interest, this curve is approximated by the relation

$$f = f_0 \sin\left[\frac{2\pi(x - x_0)}{\lambda}\right] \tag{6.1}$$

Here x_0 is the equilibrium position of the atom, f_0 is the maximum restoring force and λ reflects the atomic periodicity being of the order of a_0. The work of adhesion per unit area is then

$$G = \int_{x_0}^{\infty} f dx = \frac{\lambda f_0}{\pi} \tag{6.2}$$

The initial stress versus displacement curve, as approximated in figure 6.2 exhibits linear elastic, Hookean, behaviour. This justifies the derivation of f_0 for the linear case.

$$f = E\left(\frac{x - x_0}{x_0}\right) \tag{6.3}$$

Here E is Young's modulus and x_o represents the interatomic spacing. Equating the derivatives of expressions 6.1 and 6.3 with respect to x delivers a value for f_0.

$$f_0 \cong \frac{E\lambda}{2\pi x_0} \tag{6.4}$$

An expression for the strain energy release rate G may be derived from equations 6.2 and 6.4. Taking x_0 of the order of the interatomic distance λ, G becomes:

$$G = \frac{E\,\lambda}{2\pi^2} \tag{6.5}$$

The strain energy release rate is linearly proportional to the Young's modulus and the interatomic distance. This expression of the strain energy release is only valid for isotropic linear elastic media, which do not contain stress

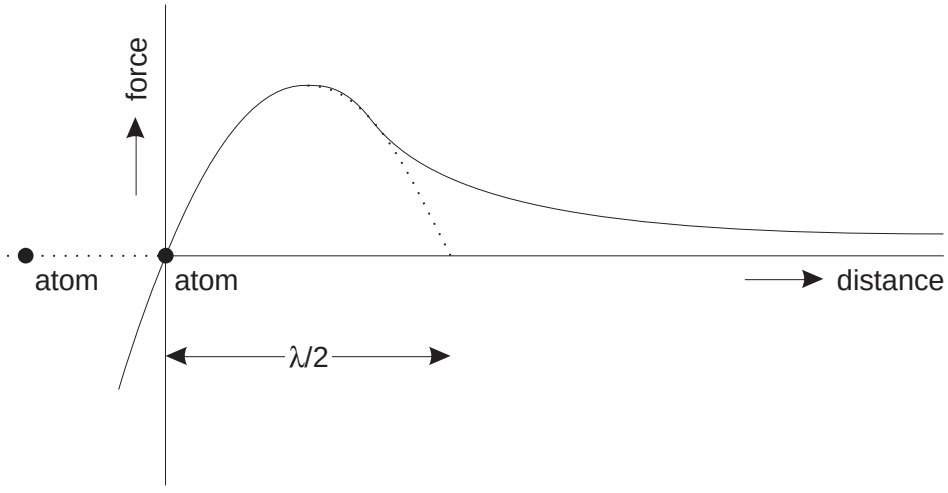

figure 6.2: *Force between two atoms.*

concentrators and if no plastic deformation takes place around the crack tip. Typical values of G for selected ceramic materials are listed in table 6.1 using the values for E and λ taken from The Oxide Handbook [2].

table 6.1: Strain energy release rate

material	Young's modulus (GPa)	λ (nm)	G (J/m^2)
α-Al_2O_3	350	0.4758	~9
TiO_2 anatase	410	0.3783	~8
SiO_2	70	0.4913	~2

The values listed are solely based on the formation of two free surfaces from bulk material. More accurate values for the strain energy release rate are obtained from the critical stress intensity factor of the materials. The critical stress intensity factor correlates the fracture stress of a material to the flaw size in the material and is defined as

$$K_{Ic} = \sigma_c \sqrt{\pi a} \tag{6.6}$$

where σ_c is the critical stress for a flaw to propagate and a is the radius of the flaw. For a flaw of size $2a$ in an infinite medium uniaxially stressed to a stress σ, the condition for crack growth is given by

$$G = \frac{dU}{da} = \frac{d}{da}\left(\frac{\sigma^2 \pi a^2}{E}\right) \geq \frac{dW}{da} = R \tag{6.7}$$

Here U is the elastic energy, W is the energy required for crack growth and R is called the crack resistance. This factor is assumed to be constant, since the energy required to produce a crack is the same for each increment da. For the strain energy release rate of solid bulk materials hold for plane strain conditions:

$$G = \frac{K_I^2}{E}(1 - \nu^2) \tag{6.8}$$

6.2 Crack propagation through porous ceramic media

The strain energy release rate as derived in section 6.1, is a measure for the amount of energy required to propagate a brittle crack through monocrystalline non-ductile material. In our studies of sol-gel processed thin ceramic layers, the conditions of the model are not fulfilled. Due to the porous nature of the layers, an effective strain energy release rate will govern crack initiation and propagation in these materials. Using the values found for the energy release rate of dense ceramic materials as listed in table 6.1, an effective energy release rate will be derived in this section.

The thin films may be described as layers of perfectly spherical particles which are placed in contact with each other. Assuming that the particles are monosized with a particle radius of the order of ~10 nm, and that the effective particle surface fraction for bonding is around 0.1, yields an effective surface for bonding of $\sim 1.25 \cdot 10^{-16} m^2$. This corresponds to $\sim 8 \cdot 10^{15}$ atoms per m^{-2} involved in bonding. For solid bulk materials these number are governed merely by the cross sectional area of an atom and are equal to $\sim 2.25 \cdot 10^{-19} m^2$ and $\sim 4.4 \cdot 10^{18}$ atoms per m^{-2} respectively. A fraction occupied with bonds may now be calculated for porous materials, with the given morphology requirements. The fraction describes the ratio of bonds between the particles in the ceramic layer, and the number of bonds between atoms in bulk material. Using this fraction and the strain energy release rate for bulk materials, as defined by equation 6.8 delivers the effective energy release rates as listed in table 6.2 for selected ceramic materials.

table 6.2: Strain energy release rate

material	G_{eff} (J/m^2)
α-Al_2O_3	~0.072
TiO_2	~0.081
SiO_2	~0.063

The values derived are of the order for Van der Waals bonding. This is argued as follows. Between interconnecting particles, bonds are formed during the drying process. Chemical bonds do not involve long range dispersive forces, and only atoms close together will interact directionally. Besides chemical bonds, here physical bonds are present in the material, of the Van der Waals/London dispersion type, with long range interactions between several particles. In the early stage of the formation of agglomerates,

the Van der Waals forces govern the elastic behaviour of the porous ceramic layer.

Applying this model to the sol-gel processed thin ceramic layers yields a value for the effective strain energy release rate of the thin films during the drying process and the onset of the curing process. The effective elastic modulus may be derived from equation 6.5 and the values determined for the effective energy release rate as listed in table 6.2. Rewriting equation 6.5 yields

$$E = \frac{2\pi^2 G}{\lambda} \tag{6.9}$$

With equation 6.9 and the values listed in table 6.2 the effective Young's modulus may be derived, as listed for selected ceramic materials in table 6.3.

table 6.3: Young's modulus

material	λ (nm)	E_{eff} (GPa)
α-Al_2O_3	0.4758	~2.9
TiO_2 anatase	0.3785	~4.2
SiO_2	0.4913	~2.5

Consequently, an expression for σ_f is derived from equations 6.1 and 6.4.

$$\sigma_F = \frac{E}{2\pi}\left(\frac{\sin\alpha}{\cos\alpha}\right) \quad \text{with} \quad \alpha = \frac{2\pi(x - x_0)}{\lambda} \tag{6.10}$$

This holds only if $cos\alpha \rightarrow 1$. To determine the fracture stress for ceramic materials, an estimate of α is required. For the α-alumina case the elastic limit is ~3-5 GPa. Together with Young's modulus of pure alumina, which is of the order of ~330-400 GPa, this yields

$$\varepsilon^* = \left(\frac{x - x_0}{\lambda}\right) \cong 7.5\ 10^{-3} \tag{6.11}$$

Using the value for ε^*, as derived in equation 6.11 for the α-alumina case, together with the values derived for the effective Young's modulus in table 6.3, the fracture stress for porous α-alumina is determined at 22 MPa.

6.3 Critical film thickness

In the following we will concentrate on the crack pattern formation as observed (figure 6.3) in the thin ceramic coatings. It is obvious that if stresses, which may be for instance thermally induced, are built up during processing eventually this may lead to delamination or spalling of the coating. Consequently, we intend to derive a relationship between crack resistance and thickness of the coating. From an isotropic linear elastic point of view the problem of elasticity of bimaterials depends essentially on two, nondimensional, elastic moduli as introduced by Dundurs [3]. In plane strain condition these boil down to

$$\alpha = \frac{\mu_1(1-\nu_2)-\mu_2(1-\nu_1)}{\mu_1(1-\nu_2)+\mu_2(1-\nu_1)}$$
$$\beta = \frac{1}{2}\frac{\mu_1(1-2\nu_2)-\mu_2(1-2\nu_1)}{\mu_1(1-\nu_2)+\mu_2(1-\nu_1)} \qquad (6.12)$$

with μ_i and ν_i the shear moduli and Poisson's ratios of both materials. It is important to realise that subscript 1 refers to the top layer. As a matter of fact, α and β both vanish if there does not exist any difference in elastic mismatch between the two layers. Further, it should be stressed that only in the case of a stiffer top layer, compared to the substrate, both α and β are positive, whereas both α and β become negative in the case of a more compliant layer. This will be discussed later.

In real materials usually the Poisson's ratio's are ~0.33 and β becomes equal to $\alpha/4$. The question that should be addressed is how the stress fields around a crack changes as a function of the distance to the interface in a dissimilar material. The stress fields near a crack tip in a homogeneous linear elastic medium are well known and they are described by

$$\sigma_{ij}^{I} = \frac{K_I}{\sqrt{2\pi r}} f_{ij}(\theta) \qquad (6.13)$$

where $f(\theta)$ contains the angular dependence relative to the crack plane.

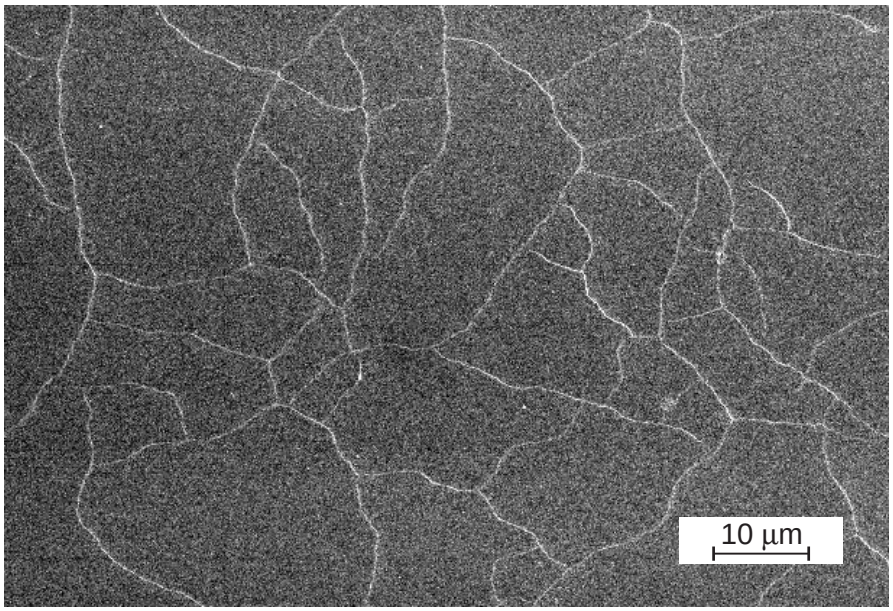

figure 6.3: *Micrograph of an Al_2O_3 layer with thickness 500nm. The cracks channelling network is visible.*

For a dissimilar material $f_{ij}(\theta)$ can be calculated according to the Muskhelisvili's stress functions Σ_{ij} [4] and they do depend on the elastic mismatch β.

$$\sigma_{ij}^{I} = Re\left\{\frac{[Kr^{i\varepsilon}]}{\sqrt{2\pi r}}\sum_{ij}^{I}(\theta,\varepsilon)\right\} + Im\left\{\frac{[Kr^{i\varepsilon}]}{\sqrt{2\pi r}}\sum_{ij}^{II}(\theta,\varepsilon)\right\} \tag{6.14}$$

where [5]

$$\varepsilon = \frac{1}{2\pi}\ln\left(\frac{1-\beta}{1+\beta}\right) \tag{6.15}$$

The $r^{i\varepsilon}$ is an oscillatory singularity that generates complications which are not present in linear fracture mechanics of a homogeneous solid. The physical reason of this oscillatory singularity has to do with the non-zero traction stress at the interface due to the elastic mismatch. Describing a mode *I/II* crack by a homogeneous distribution of dislocations, it can be seen that the stress components of the edge dislocations produce a non-zero σ_{xy} and σ_{xx} traction stress, respectively, because of the unbalanced image forces across

the interface. It is quite obvious that the strength of the crack singularity, which depends on the elastic mismatch, is less affected *far* from the interface. Consequently, at small depth the dimensionless stress intensity factor $K/\sigma\sqrt{h}$ reduces to that of a crack in a semi-infinite space, i.e. $K \rightarrow 1.121\sqrt{(\pi a)}$, with a/h approaches zero. Here a refers to the crack length and h to the thickness of the layer. For the other limiting situation equation 6.13 can be approximated by the so-called Zak-Williams singularity [6]

$$\sigma_{ij} \sim \frac{K'}{r^s} f_{ij}(\theta) \tag{6.16}$$

if a/h approaches unity. Here, K' plays the same role as the usual stress intensity factor but now it depends explicitly on s, and consequently also on the elastic mismatch. The singularity exponent s, which is in linear elasticity of a homogeneous solid equal to 0.5, is the root of

$$\frac{\alpha-\beta^2}{1-\beta^2} - 2\frac{\alpha-\beta}{1-\beta}(1-s^2) + \cos(s\pi) = 0 \tag{6.17}$$

for both α and β negative. The strength of the Zak-Williams singularity is calculated numerically as a function of positive values of α for two cases: $\beta=\alpha/4$ and $\beta=0$, the latter of which represens incompressible solids. The results are displayed in figure 6.4. It is interesting to see that the limit of the strength singularity approaches 1 if α becomes equal to 1. In other words, the singularity of the crack approaches the strength of the singularity of a single dislocation. This is consistent with the physical description of a crack as a distribution of edge/screw dislocations , the limit of which is one single dislocation possessing a long range stress singularity of a strength r^{-1}.

In the present system of interest, α-alumina/fused silica, $\alpha=0.7$ and $\beta=0.28$ and the strength of the crack singularity s is equal to 0.6. Dimensional considerations between equations 6.13 and 6.16 leads to the conclusion that the stress intensity factor K should be related to the far field K' according to

$$K \sim \frac{K'}{(h-a)^{s-\frac{1}{2}}} \tag{6.18}$$

whereas the dimensionless stress intensity factor $K/\sigma\sqrt{h}$ changes accordingly and becomes proportional to $(1-a/h)^{½-s}$ as $a \rightarrow h$.

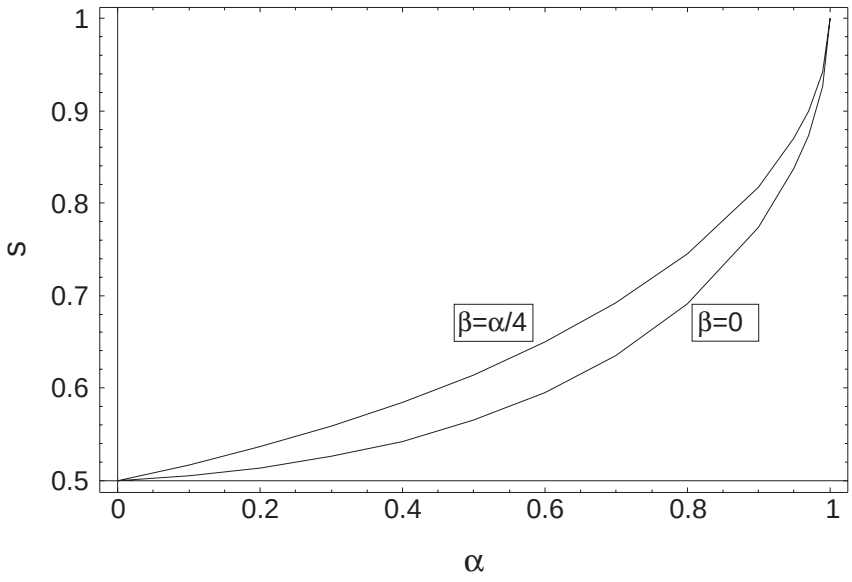

figure 6.4: *Strength of the singularity as a function of α.*

Based on these considerations a dimensionless crack resistance factor can be derived. The basic idea is that the elastic strain energy stored is simply

$$\frac{(1-\nu_1)\sigma^2 h}{E_1} \tag{6.19}$$

so that the energy release rate for a crack inside the top layer is proportional to equation 6.17 with a proportionality constant δ depending on the crack pattern. Practical relevance of δ was first documented by Evans et al. [7]. It varies between 4 in the case of surface cracks, 2 for channeling cracks and 1 for debonding. In the case of steady state crack propagation, δ is equal to 0.5. The values of δ can be verified by finite element calculations by which slightly deviating values can be found, for instance : δ=1.97 for channeling cracks. The energy release rate and the dimensionless stress intensity factor $K/\sigma\sqrt{h}$ are related to each other by

$$\frac{GE_1}{\sigma^2 h\left(1-\nu_1^2\right)} = \left(\frac{K}{\sigma\sqrt{\pi h}}\right)^2 \tag{6.20}$$

As mentioned before, the stress intensity factor should approach $1.12\sigma\sqrt{(\pi a)}$ as $a/h \to 0$ and becomes proportional to $(1-a/h)^{1/2-s}$ as $a \to h$ and therefore equation 6.20 can be rewritten as

$$\frac{GE}{\sigma^2 h\left(1-\nu_1^2\right)} = \left[1.12\sqrt{\pi}\left(1-\frac{a}{h}\right)^{\frac{1}{2}-s}\left(\frac{a}{h}\right)^{\frac{1}{2}}\right]^2 \qquad (6.21)$$

Numerical solutions are in agreement with equation 6.21 except for an additional factor $(1+\gamma a/h)$ where γ depends on α and β. However, this seems to be relevant only at large a values, close to h, whereas at intermediate values of a the deviation is only a few percent. In figure 6.5 the dimensionless crack resistance of equation 6.21 is plotted as a function of a/h for pure α-alumina/fused silica with s=0.6, the upper curve, together with the prediction based on a homogeneous elastic solid, s=0.5.

It can be concluded from this analysis that shallow cracks starting from zero energy release rates diverges to infinity for the stiffer layer near the interface, that is to say the driving force for crack propagation diverges close to the

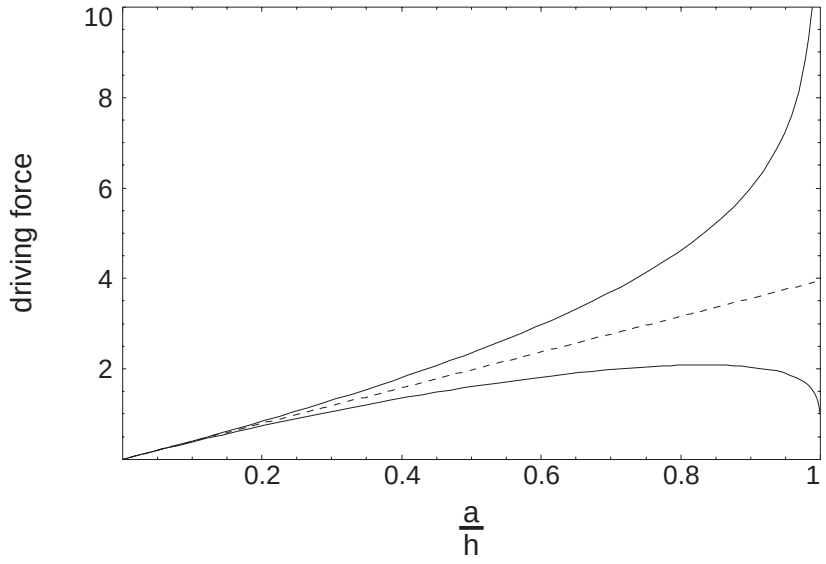

figure 6.5: *Crack driving force as a function of a/h. The upper curve depicts the driving force for pure α-alumina/fused silica, s=0.6, the dashed line is the prediction for a homogeneous solid, s=0.5. The lower curve depicts the behaviour for a compliant film on a stiff substrate, s=0.4. For the compliant film, the driving force for crack propagation attains a maximum at intermediate values of a/h*

interface. The cracks in the more brittle top layer cannot be stopped from running to the interface if the fracture resistance is considerable smaller than the driving force displayed for a particular depth. The crack resistance is related to the surface energy term Γ_1 and consequently cracks will not be activated if the crack resistance $\Gamma_1 E_1/\sigma^2(1-\nu_1^2)h$ is larger than the driving force available for a crack at a particular depth *a/h*.

Let's turn now to the situation of the porous nanostructured ceramic layer, figure 6.3. Here we derived an effective Young's modulus which is smaller than the underlying substrate, see table 6.3, and consequently the sign of α and β, equation 6.12, reverse compared to the values of bulk materials. Actually, the top layer becomes more compliant than the substrate, the situation of which is displayed in figure 6.5 as the lower curve, for values of α=-0.87, β=-0.28 and, here it is found that s<0.5, namely s=0.4. It is interesting to see that in relatively compliant layers, the driving force for crack propagation attains a maximum at intermediate values of *a/h*. The consequence is that if the crack resistance $\Gamma_1 E_1/\sigma^2(1-\nu_1^2)h$ is larger than the maximum of the crack driving term, no crack will be activated and it will not proceed to the interface leading to delamination and debonding.

The dimensionless driving force also affects the kind of crack pattern that is expected. A specific cracking pattern is inhibited if the layer is thinner than a critical thickness, given by

$$h_c = \frac{\Gamma_1 E_1}{\delta\,\sigma^2\left(1-\nu_1^2\right)} \tag{6.22}$$

Based on equations 6.10 and 6.11 this can be rewritten for the present case of porous α-alumina/fused silica as

$$h_c = \frac{2\lambda}{\delta\,\sin^2 2\pi\varepsilon^*} \tag{6.23}$$

The thickness of the layer is displayed in figure 6.6 as a function of the crack driving force. Surface cracks are predicted for a thickness between 0.2 μm and 0.1 μm, whereas channeling cracks are expected for a thickness larger than 0.2 μm and delamination for the range larger than 0.4 μm [8]. In the present case the crack resistance for a layer thickness smaller than 0.2 μm is larger than the crack driving term and no cracks will be activated.

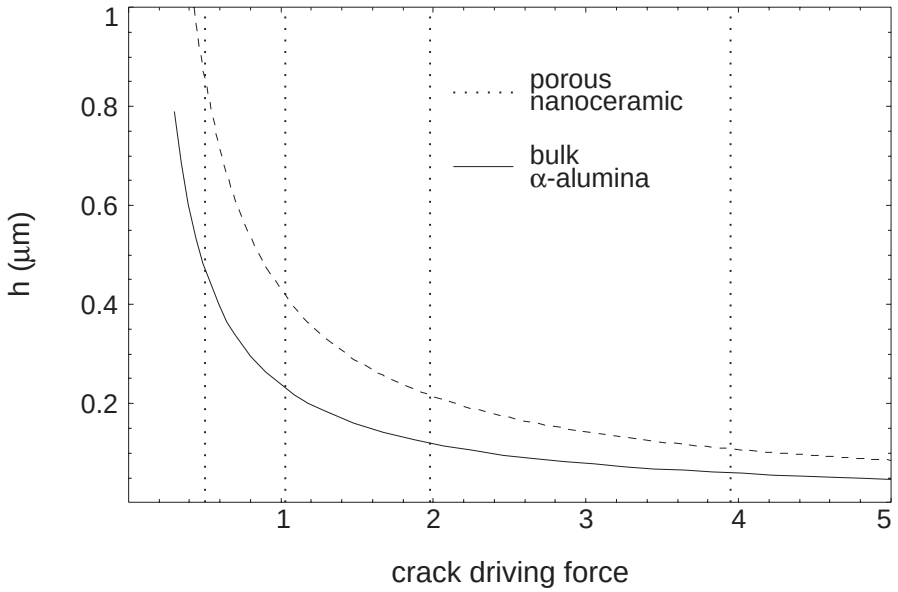

***figure 6.6**: Dependence of the crack resistance factor on the thickness of the layer. The three different cracking regimes are indicated. It is interesting to see that the critical thickness of the layer at comparable crack driving force is larger for the porous nanoceramic than for the bulk α-alumina materials*

From figure 6.6 it is clear that the more compliant porous α-alumina shifts these ranges to larger thicknesses. Further it can be concluded that cracks in thin layers, ≤0.2 μm, will not be activated, which sets a design limit for these compliant nanoceramic coatings.

6.4 Failure of thin ceramic layers during laser curing

The laser curing may have various influences on the sol-gel layers. It is desired in the laser curing process that these layers are densified and that homogeneous dense films are obtained. In section 4.3.3 several laser cured Al_2O_3 layers were studied using scanning electron microscopy. From the micrographs, differences in derived microstructure and morphologies were observed, ranging from dense homogeneous layers to severely debonded layers in which large blisters are observed. In this section the processes which may cause this debonding are studied in more detail.

As already mentioned in section 4.3.3, the blister formation is assumed to be induced by compressive stresses in the layer [9,10] or by the evaporation of entrapped liquid in the layer [11]. During and after spinning of the layers,

volatiles leave the solid network by evaporation. As a result, the network collapses, reducing pore sizes in the layer and thereby reducing the permeability of the layer. This may cause liquid in the layer being entrapped in closed pores. Upon laser curing of the layers this liquid becomes gaseous and expands drastically. Due to the low permeability of the layer, pressure will build up in the layer. If this pressure is large enough, the layer will fail, producing blisters. Assuming that the entrapped liquid is water, an estimate can be made of the evolving pressure if the water evaporates fully. As a result of the evaporation, the total volume required to accommodate the amount of water increases drastically, according to

$$V_g = \frac{V_p \rho}{m_m} V_m \tag{6.24}$$

with V_p the volume of the pore containing the liquid water, ρ the density of water, m_m the molar mass of water and V_m the molar volume. If the total amount of gas has to be accommodated in the initial pore, the pressure in the pore will increase according to

$$p_g = p_p \frac{V_g}{V_p} \tag{6.25}$$

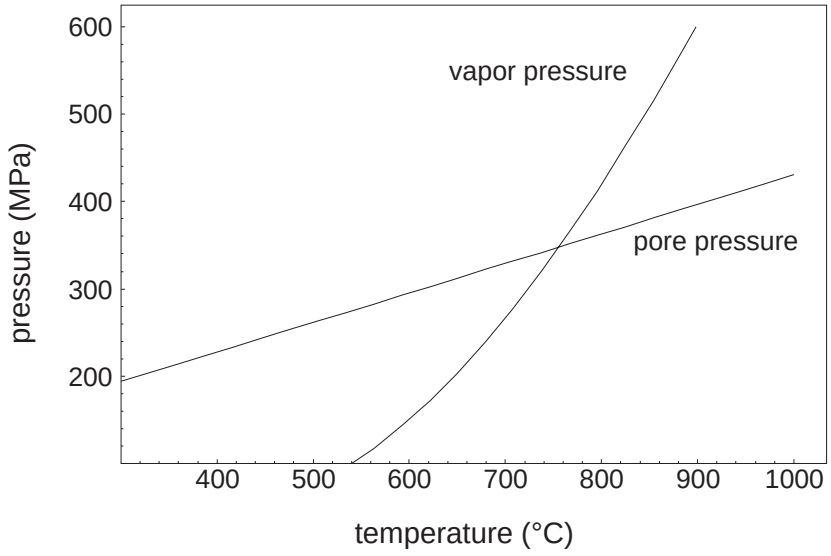

figure 6.7: *The pressure in the pores as a function of the curing temperature. The vapour pressure of H_2O is indicated.*

Upon further increasing the temperature, the pressure will increase according to

$$p_p = p_g \frac{T_c}{T_b} \tag{6.26}$$

with T_c the laser curing temperature and T_b the boiling point of water. Figure 6.7 depicts the pressure in the pore as a function of temperature. A hydrostatic pressure with magnitude of the order of ~300-400 MPa builds up in the pore. For the liquid to become gaseous it is required that the pressure in the pore is below the vapour pressure. At 100°C water has a vapour pressure of ~1 10^5 Pa. The vapour pressure increases with temperature, an empirical relation between temperature and vapour pressure is depicted in figure 6.7. At ~700-800°C the vapour pressure increases rapidly with temperature, therefore the gas will not condense at this high pressure level. The pressure evolving in the pores does not depend on the volume of the entrapped liquid in this derivation, for pores with dissimilar dimensions the pressure in the pore will be comparable. The solid network has to sustain the pressure evolving in the pores. Whenever the network can not sustain the pressures in the pores, the layer is expected to fail in a blistering process.

An alternative cause for the formation of blisters in the layer during the laser curing may be buckling of the layers as a result of large compressive stresses. Compressive stresses in the layer arise if the thermal linear expansion coefficient of the layer is larger than the expansion coefficient of the substrate. Upon heating of the system, both substrate and layer will expand. Since the layer is constraint by the substrate, compressive stresses will build up due to the thermal linear expansion misfit. If these thermally induced stresses are large enough, the layer may fail in a buckling process. The critical compressive stress for buckling of the layer is derived for a system as depicted in figure 6.8. For buckling it is necessary that at the interface between the substrate and the layer, of thickness h, flaws already are present [12]. The critical compressive edge stress for buckling is given by [13]

$$\sigma_c = \frac{kE}{12(1-\nu^2)} \frac{h^2}{a^2} \tag{6.27}$$

with k=14.68, a the flaw radius, E is the Young's modulus of the layer and ν its Poisson's ratio. For the thin films, the thickness is of the order of

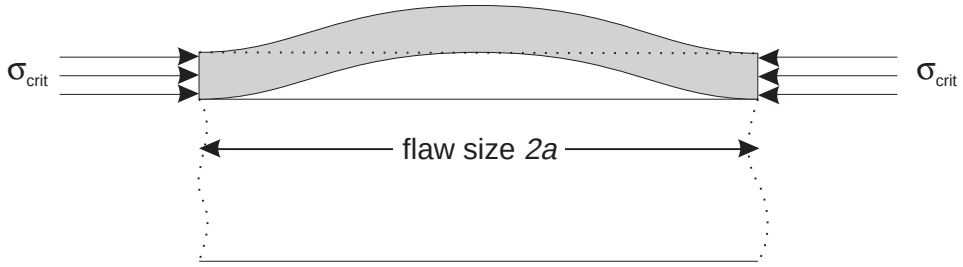

figure 6.8: *Schematic depiction of the buckling process.*

~100-500nm. From figure 4.14.*c*, in which a top view micrograph of the blisters formed is depicted, the size of the flaws is estimated, assuming that they do not expand laterally in the buckling process. The flaw size *2a* is of the order of ~1 μm. Using the value for the effective Young's modulus as derived in section 6.2, $E \cong 3\ GPa$, the critical stress for buckling is calculated. In figure 6.9 this critical stress is depicted as a function of layer thickness and initial flaw radius. Using the layer geometry and figure 6.9, it may be predicted whether initial flaws of radius *a* will fail in a buckling process when

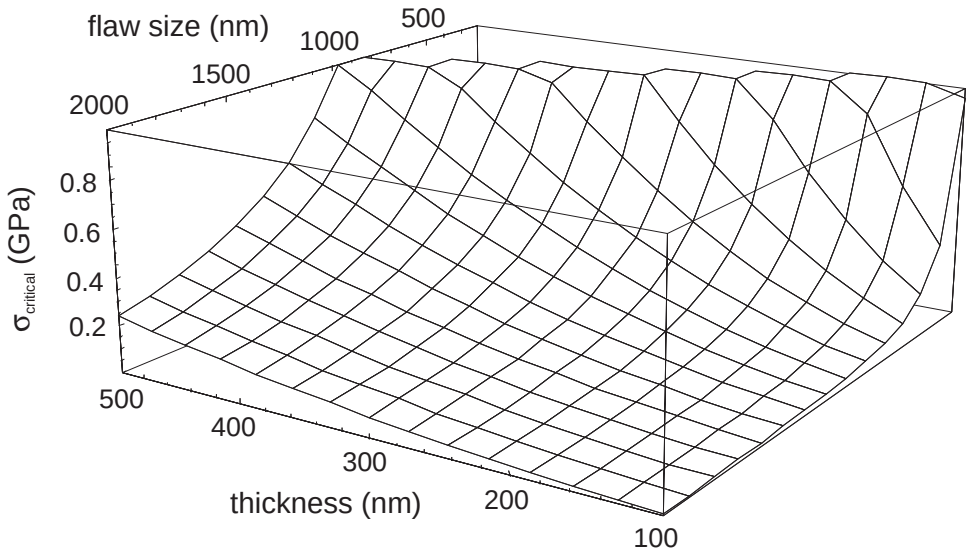

figure 6.9: *Calculation of the critical buckling stress as a function of initial flaw size and the thickness of the layer.*

compressive stresses evolve in the layer. The critical stress for a layer of ~500nm containing flaws with radius ~1 μm is ~1 GPa. This stress has to be accounted for by the thermal expansion misfit. Using equation 6.28 the expected thermal stress may be derived for the layer substrate system consisting of a fused silica substrate and a sol-gel derived Al_2O_3 layer.

$$\sigma_{th} = \frac{E_l}{1-\nu_l} \int_{T_C}^{T_R} \Delta\alpha dT \qquad (6.28)$$

In the calculation the substrate is assumed to be infinitely stiff. If the temperature during laser curing is ~1000°C then this would cause compressive stresses in the layer to build up of ~30 MPa. The expected compressive stress is calculated using values for the thermal expansion coefficients of the layer and substrate of $8.0 \cdot 10^{-6} K^{-1}$ and $0.5 \cdot 10^{-6} K^{-1}$, respectively. This compressive stress is smaller than the required stress of 1GPa for flaws of radius ~1 μm to buckle. Flaws that will buckle at this expected stress level, for a layer with thickness 500 nm, require to be of radius 5 μm. However, blisters of this size were not observed.

6.5 Discussion

The thickness of thin sol-gel derived layers is limited. Exceeding the critical film thickness will result in delamination of the layer. In the literature, empirical film thicknesses for spun or dipped layers are of the order of ~500-1000 nm [14,15]. Layers with larger thicknesses turn opaque, due to severe cracking in the layers, or delaminate. High thickness layers may be obtained by repetitive deposition of films of low thickness. Post heat treatment of the layers after each deposition increases the final thickness of crack free layers. In the sections 6.2 and 6.3 a critical film thickness is derived for the sol-gel derived thin film systems. The effective Young's modulus derived in section 6.2 is of great importance for the final behaviour of the thin films. Using an approach in which not the porosity of the material [16,17] but the effective surface for bonding governs the elastic behaviour of the material, an estimate is derived for the effective strain energy release and the effective elastic modulus for nanosized materials of high porosity. The values for the strain energy release derived for selected ceramic thin films are in agreement with the values expected for Van der Waals bonding. Using the effective elasticity modulus, a model is derived which describes the thickness

of the layer in terms of a crack resistance factor. For the Al_2O_3 layers, three regimes in layer thicknesses are indicated, for layers with thicknesses below ~0.2 μm only surface cracking is expected in the layers. Increasing the thickness will result in channelling cracks in the layers, and the critical thickness for these layers is of the order of ~0.4 μm. Exceeding this critical thickness will result in delamination of the layers.

As shown in section 4.3.3 the laser curing process influences the final properties of the sol-gel derived thin layers to a large extent. Homogeneous dense layers may be obtained if the parameters in the curing process are selected adequately. If the parameters are chosen incorrectly, severely debonded layers may be obtained. In section 4.3.3 it is seen that the pre-curing treatment plays a role in the total curing process. Pre-heating the layers resulted in less blister formation as may be seen in figure 4.14. In section 6.4, mechanisms which may cause the layers to fail are examined in more detail. Sol-gel layers containing entrapped liquids in closed pores are expected to build up high hydrostatic pressures as a result of the laser curing process, of the order of ~500 MPa. These large hydrostatic pressures has to be sustained by the solid network. Any pressure building up in the layers is hard to relax by degassing, due to the low permeability of the layers, therefore, formation of blisters is a mechanism for the pores under pressure to relax.

An alternative mechanism by which the blisters in the layers may be formed is the evolution of compressive stresses in the layers. Due to a misfit in thermal linear expansion coefficients of both substrate and layer, the substrate and layer will expand dissimilar upon temperature changes. As a result of the misfit in expansion, thermally induced stresses are expected to arise in the layer and substrate. Whenever these stresses exceed a critical stress level, the layer will fail in a buckling process. In section 6.4 this critical stress is determined for the layers of interest. The critical stress level is determined by, amongst others, the thickness of the layer and the size of flaws present initially. For the system with a layer thickness of the order of ~500 nm the size of the flaws is estimated from figure 4.14.*c*. Together with figure 6.9 a critical buckling stress of ~1 GPa is determined for this system. An evaluation of the expected thermally induced stress as a result of the laser curing process indicates that these stresses do not exceed ~100 MPa. This low stress value is attributed to the low effective Young's modulus of the layer.

For layers to buckle at this stress level, initial flaws of the order of ~5 μm are required. However, blisters of this size were not observed.

From the calculations and the observed layer morphologies as depicted in figure 4.14, it is concluded that the blisters are not likely to be introduced by compressive stresses in the layer. The stresses evolving in the layer are too small for the layer to fail in a buckling process, regarding the size of the initial flaws at the interface between layer and substrate. The reduction in blister formation as a result of the pre-curing process, prior to the laser curing, indicates that the blisters are caused rather by the evaporation of entrapped liquids in the layers.

References

1 D. Broek, Elementary Engineering Fracture Mechanics, Noordhoff Int. Publ., Leyden, (1974), 257.

2 G.V. Samsonov, The Oxide Handbook, Plenum, New York, (1973), 23.

3 J. Dundurs, J. Appl. Mech., **36**, (1969), 650.

4 N.I. Muskhelishvili, Singular Integral Equations, Noordhoff, Amsterdam, (1953).

5 J.R. Rice, J. Appl. Mech., **55**, (1988), 98.

6 A.R. Zak and M.L. Williams, J. Appl. Mech., **30**, (1963), 142.

7 A.G. Evans, M.D. Drory, M.S. Hu, J. Mater. Res., **3**, (1988), 1043.

8 I. Strawbridge and P.F. James, J. Non-Cryst. Solids, **82**, (1986), 366.

9 E. Madenci, H. Balkan and M. Quan, Int J. Solids Stuctures, **32**, (1995), 3465.

10 M. Ortiz and G. Gioia, J. Mech. Phys. Solids, **42**, (1994), 531.

11 C.J. Brinker and G.W. Scherrer, Sol-Gel Science, Academic Press, San Diego, (1990), 636.

12 A.G. Evans and J.W. Hutchinson, Int. J. Solids Structures, **20**, (1984), 455.

13 S. Timoshenko and J.M. Gere, Theory of Elastic Stability, McGraw Hill, New York, (1961)

14 I. Strawbridge and P.F. JAmes, J. Non-Cryst. Solids, **86**, (1986), 381.

15 S. Sakka, K. Kamiya, K. Makita and Y. Yamamoto, J. Non-Cryst. Solids, **63**, (1984), 223.

16 V. Krstic, U. Erb and G. Palumbo, Scripta Metall. Mater., **29**, (1993), 1501.

17 N. Ramakrishan and V.S. Arunachalam, J. Am. Ceram. Soc., **76**, (1993), 2745.

SUMMARY

In this thesis the relation between processing and residual stress states in ceramic materials is studied. Various materials are considered, bulk ceramics derived from powder compacts as well as thin ceramic layers derived using a sol-gel technique. The influence of the processing techniques on the eventual residual stress state of the material is studied.

Material properties may be altered by microstructural modifications. This holds for a large range of materials, metals as well as ceramics. In this thesis, the influence of a second phase added to a homogeneous matrix is studied. The addition of ZrO_2 to an α-alumina matrix increases the fracture toughness of the composite ceramic with 160%. The increase in toughness is achieved through the tetragonal to monoclinic phase transformation which takes place upon cooling of the specimen, or is induced by high tensile stresses ahead of a crack tip.

The addition of a second phase in a matrix also is a means for tailoring the final particle distribution of the material. Grain growth is controlled by dispersed second phase particles through the forces these particles exert on moving grain boundaries in the matrix. Addition of a second phase leads to a grain size in the matrix controlled through the radius of the second phase particles and the volume percentage added. The measured grain sizes in the specimens studied correspond well to the expected limited grain sizes in the matrix.

Diffusion bonding the two-phase ceramic layer to a layer of homogeneous α-alumina is performed using different processing routes. A method to derive these specimen is to mould and sinter the specimen in one process. The precursor powders are pressed simultaneously and consequently sintered to high relative densities. A problem using this approach is the difference in shrinkage during the sintering process, resulting in debonding of the two layers. Therefore, an alternative approach is used in which the layers are formed separately. These layers are then pre-sintered, hence pre-shrunk, and consequently placed in contact and sintered to high relative densities.

Problems encountered in this process are stresses arising in the specimen as a consequence of dissimilar shrinkage upon cooling of the specimen induced by differences in thermal linear expansion coefficients of both layers. The thermally induced stresses are calculated using analytical as well as finite elements methods. The finite elements approach provides insight in the total residual stress state of the specimen, whereas the analytical approach yields values for the maximum expected stresses across the interface. Both methods indicate that the two-phase layer, exhibiting a larger thermal linear expansion coefficient, is in tension after the curing process, and the homogeneous layer is in compression. The magnitude of the evolving stresses are typical of the order of ~50-100 MPa. In the bulk of the specimen the radial and tangential stress components are equivalent in sign and magnitude, at the free edges the radial component can not be sustained by the free surface and drops to zero. The tangential component, however, reduces in magnitude but a gradient is still present over the interface.

The determination of the residual stress state in the samples using x-ray residual stress analysis, requires for the x-ray elastic constants to be known. For typical applications, it is appropriate to use the macroscopical materials properties, Young's modulus and Poisson's ratio. Since the x-ray elastic constants for the two-phase material are unknown, they are determined experimentally using an especially designed in-situ loading device. In contrast to experimental methods commonly used, employing a tensile loading state, here a device is constructed in which the material is stressed compressively. The advantage of this loading mode is that the material under investigation is in uniaxial compression. For materials exhibiting brittle like crack behaviour, the compressive mode enables the loads to reach values higher compared to experiments performed in tension. Experimental determination of the x-ray elastic constants for ceramics may thus be performed over a range of stresses larger than when using a tensile loading mode, resulting in more accurate values. The uniaxial character of the stress state secures that no corrections to the measured lattice strains are required. The x-ray elastic constants for the α-alumina compare to the determined constants for the two-phase material.

In the determination of the residual stress fields in the composite ceramic products, the experimentally derived x-ray elastic constants are used. The residual stress fields measured throughout the samples compare well to the stress values evaluated using finite element methods. At the locations of

interest, i.e. the interface, the comparison between measured and calculated is best. Using an alternative approach for residual stress determination , the hole drilling evaluation technique, delivers similar results as the x-ray stress analysis method.

Sol-gel derived thin ceramic layers are studied using various techniques. Scanning electron microscopy is used to reveal the microstructure and morphologies of the layers. The differences in curing processes appeared to dictate the final morphologies of the layers. For the TiO_2 layers grain growth is observed for the furnace as well as the laser cured layers. The activation energy for grain growth of these layers is determined and corresponds to other studies concerning these type of sol-gel layers. Furnace curing the ceramic layers results in dense layers.

X-ray diffraction methods are used to evaluate crystallisation and stress evolution in the TiO_2 layers. For the various cured specimen it proved that the as spun layers are amorphous. They crystallise during the heat treatment, provided that the curing temperatures and times suffice for crystallisation to take place. For the furnace cured specimen, the temperature at which crystallisation is observed is 700°C. Increasing the curing temperature to 900°C and 1200°C, respectively, results in further crystallisation of the layers and a transformation from the anatase to the rutile phase takes place. Using x-ray residual stress analysis, the residual stress state is determined for specimen which experienced dissimilar heat treatments. The stress values in the specimen are compared to the expected stresses which arise as a result of thermal expansion misfit in the layers. From this comparison it is concluded that the stresses in the layers are thermally induced.

Tensile stresses evolve in the layers during the spinning and drying stage. Due to capillary forces as a result of the evaporation of liquids in the solid network, tensile stresses evolve in the layer. This results in cracks in the layers. For the highly porous layers a model is derived which describes the thickness of the layer in terms of the crack resistance factor. A crack pattern is expected for layers of various thicknesses, depending on this thickness. Thick layers, that is for Al_2O_3 layers thicknesses exceeding 500 nm, are expected to delaminate, layers with lower thicknesses will exhibit channelling crack like behaviour. For layers of low thickness, typical below 200 nm, only sub-micron sized surface cracks are expected and observed in the layers.

SAMENVATTING

Fysische eigenschappen van materialen worden door een complex patroon van verschillende factoren bepaald. Uiteindelijk dient de kwaliteit van een materiaal voor een specifieke toepassing geoptimaliseerd te worden. Dit proefschrift concentreert zich op verschillende keramische materialen, die via twee totaal verschillende processen worden verkregen: het ene proces levert bulk keramische materialen op, via het andere proces, sol-gel technieken, kunnen zeer dunne keramische lagen worden verkregen. Ofschoon de bereidingswijze van de materialen in beide processen totaal verschillend is, d.w.z. bulk materialen worden verkregen door het persen van poeders in de gewenste vorm en keramische lagen vanuit een colloidale vloeistof, bestaat er toch een overeenkomst in beide processen. Het verkregen groene product moet in een thermisch geactiveerd proces verdicht worden tot een materiaal met lage porositeit, waardoor interne mechanische spanningen kunnen ontstaan. In dit onderzoek wordt de correlatie tussen productietechnieken van keramische materialen en de restspanningen als gevolg van deze technieken beschreven. Röntgendiffractie vormt de belangrijkste experimentele methode in dit proefschrift om de spanningstoestand nauwkeurig te bepalen.

Voor de bulk materialen is de invloed van een toegevoegde tweede fase op een homogene keramische matrix bestudeerd. Toevoeging van zirconia aan een α-alumina matrix verhoogt de breuktaaiheid van het samengestelde keramiek met 160%. Deze vergroting van de breuktaaiheid wordt bewerkstelligd door een transformatie van het zirconia van de tetragonale naar de monocliene fase tijdens afkoelen van het preparaat, of door de hoge trekspanningen aanwezig bij een scheurtip. De toevoeging van een tweede fase aan een matrix is ook een methode voor het optimaliseren van de uiteindelijke deeltjesgrootte verdeling in het materiaal. Het blijkt dat de korrelgroei wordt gecontroleerd door de krachten die de tweede fase deeltjes uitoefenen op bewegende korrelgrenzen in de matrix.

Het door diffusiemechanismen aan elkaar verbinden van het twee fasen materiaal aan het homogene α-alumina materiaal is bewerkstelligd door gebruik te maken van verschillende procestechnieken. In de eerste methode worden de lagen tegelijkertijd verdicht in een één-assig drukproces en

daarna verdicht in een oven. Een probleem dat tijdens deze productie-methode optreedt is de ongelijke krimp van de beide lagen tijdens de verdichtingsstap, waardoor er mechanische spanningen over het grensvlak optreden die aanleiding kunnen zijn tot scheuren. In een tweede methode wordt dit probleem omzeild door de lagen eerst separaat te persen en te verdichten. Hierna worden de lagen in contact met elkaar gebracht en verdicht tot hoge relatieve dichtheden. Via beide productiemethoden is tussen de verschillende keramische materialen door middel van diffusie een verbinding tot stand gebracht.

De problemen die in beide processen optreden zijn de ongelijke krimp van de beide lagen tijdens het afkoelen van het uiteindelijke preparaat. Deze thermisch geïnduceerde spanningen zijn berekend aan de hand van een analytisch model en op basis van eindige elementen methoden. De eindige elementen methode geeft inzicht in de totale spanningstoestand in het preparaat, de analytische benadering geeft de maximaal verwachtte spanningen over het grensvlak. Volgens beide methoden is de twee fasen laag in een trek-toestand, t.g.v de grotere thermische uitzettingscoefficient, en de laag van α-alumina in een spanningstoestand met een compressief karakter. De grootte van de spanningen zijn van de orde ~50-100 MPa. In de bulk van de preparaten zijn de radiële en de tangentiële spannings-componenten gelijk aan elkaar, zowel in grootte als in teken.

De restspanningstoestand is experimenteel bepaald met behulp van röntgen spanningsanalyse. Voor het nauwkeurig bepalen van de spanningen zijn de röntgen elastische constanten nodig. Deze constanten zijn voor het α-alumina en het twee fasen materiaal experimenteel bepaald door middel van een in huis ontwikkeld in-situ druk apparaat. In tegenstelling tot andere methoden in de literatuur, die gebruik maken van een opgelegde trekspanning, is hier gekozen om een één-assige druk-toestand te gebruiken. Het voordeel van deze spanningstoestand is dat voor keramische materialen, die een bros breukgedrag bezitten, de spanningen die aangelegd kunnen worden veel hoger mogen zijn in druk dan in trek. Het is derhalve mogelijk om over een groter gebied van opgelegde spanningen de elasticiteitsconstanten te bepalen, wat resulteert in nauwkeurigere waarden voor deze constanten. Verder zorgt het één-assige karakter van de spanningstoestand ervoor dat er geen correcties op de bepaalde rooster-rekken nodig zijn. Voor het bepalen van de restspanningen in de samengestelde keramische producten zijn de experimenteel bepaalde constanten gebruikt. De gemeten restspanningen in

de preparaten komen goed overeen met de waarden die bepaald zijn met behulp van de eindige elementen methode. Vooral op die plaatsen in het preparaat waar de spanningen belangrijk zijn, in de buurt van het grensvlak, komen de gemeten en uitgerekende waarden goed overeen. Ook een alternatieve methode om de spanningen te bepalen in de preparaten, de zogenaamde gaten relaxatie methode, levert vergelijkbare resultaten op voor de spanningen in het materiaal. Bij deze techniek wordt de relaxatie van het materiaal rond een aangebracht gat gemeten, waarna de spanningstoestand in het materiaal uitgerekend kan worden.

Behalve bulk keramische materialen zijn tevens dunne keramische lagen bestudeerd. Deze zijn via een sol-gel spinning techniek opgebracht. In het bijzonder zijn TiO_2 lagen bestudeerd. Kristallisatie en restspanningen in de TiO_2 lagen zijn onderzocht met behulp van röntgendiffractie. De lagen bleken amorf te zijn na het spin proces en als gevolg van de warmtebehandeling te kristalliseren. De behandelingstemperatuur waarbij kristallisatie voor het eerst werd waargenomen is 700°C. Verhogen van de behandelings-temperatuur tot 900°C en 1200°C resulteert in verdergaande kristallisatie van de lagen. Ook wordt er voor deze hogere temperaturen een fasetransformatie waargenomen van de anatase naar de rutiel fase. De restspanningstoestand voor lagen die verschillende ovenbehandelingen hebben ondergaan, is bepaald met behulp van röntgen spanningsanalyse. De spanningen in de preparaten zijn vergeleken met de theoretische spanningen die geïnduceerd worden in de lagen als gevolg van de warmtebehandeling. Uit deze vergelijking blijkt dat de aanwezige spanningen thermisch geïnduceerd zijn.

Trekspanningen evolueren in de lagen tijdens het spinnen en het drogen van de lagen als gevolg van de capillaire krachten die ontstaan door het verdampen van vloeistoffen in de poriën van het deeltjes-netwerk. Deze spanningen veroorzaken scheuren in de lagen. Een model is afgeleid wat de dikte van de laag beschrijft in termen van een scheurweerstandsfactor. Volgens dit model is voor een bepaalde dikte van de laag een specifiek scheurpatroon te verwachten. Voor lagen met een grote dikte, dat is voor Al_2O_3 lagen een dikte groter dan ~500 nm, worden scheuren tussen laag en substraat verwacht, resulterend in delaminatie. Lagen met een geringere dikte zullen een scheuren-netwerk vertonen, en lagen met een dikte kleiner dan ~200 nm bezitten oppervlaktescheuren van sub-micron grootte. Deze voorspelde scheurpatronen zijn, als functie van de laagdikte voor de Al_2O_3 lagen, experimenteel bevestigd.

DANKWOORD

Daar nu het eind gekomen is aan vier lange, soms ook korte jaren, is dit de tijd en de plek alle personen te bedanken die bijgedragen hebben aan de totstandkoming van dit proefschrift. Omdat promotieonderzoek niet iets is wat normaliter door een enkel persoon alleen uitgevoerd kan worden, is de lijst van te bedanken personen omvangrijk.

Als eerste op de lijst staat mijn promotor Jeff de Hosson. Ruim voordat mijn promotieonderzoek van start ging, was ik reeds bekend met zijn vermogen om mensen te stimuleren en te sturen op het wetenschappelijke pad. Zonder zijn stimulerende begeleiding en zijn wetenschappelijke bijdragen aan dit proefschrift, zou het er niet zijn geweest. Het ontrafelen van de fysica achter de observaties, was een strijd die ik met plezier samen met hem voerde.

Voor de discussies en wetenschappelijke alswel experimentele inbreng die ik van het Research Laboratorium, Koninklijke Hoogovens, ontving, wil ik de volgende personen bedanken: Sido Sinnema, Winfried Kranendonk, J. de Boer, Leo Woning voor de vele discussies, en Steve Verdier voor het aanleveren van de, vaak moeilijk te produceren, preparaten die ik altijd zo graag wilde ontvangen.

Het (top-)instituut Materiaalkunde aan de R*u*G zou niet kunnen bestaan zonder de uitstekende infrastructuur zoals deze aanwezig is: Geert Boom, Paul Bronsveld, Bart Kooi en Irene de Hosson, die uitstekend zorgde voor de administratie en het uitwerken van allerlei rapporten en papers, Henk Bron, Jan Harkema, James Kuiper, Uco Nieborg, Klaas Post, Oomke Schutter stonden altijd klaar met raad en daad voor de problemen waar ik mee aan kwam zetten. Frans van de Horst was altijd bereid problemen met de röntgenapparatuur, en -metingen, uit de wereld te helpen.

In de loop der jaren is de groep Materiaalkunde dankzij de inspanningen van Jeff de Hosson gestaag groter geworden. Groter in physisch opzicht, er kwamen steeds meer onderzoeksfaciliteiten voor de promovendi, maar ook groter in physiek opzicht, om met al deze apparaten physica te bedrijven, steeg het aantal promovendi. Bij mijn kennismaking met de groep waren reeds aanwezig: Peter-Henk Amesz, Jan-jaap Aué, Benno van Brussel, Menno van den Burg, Jim-Wah Chung, Durandus Dijken, Jacob Kerssemakers,

Lodewijk de Mol van Otterloo, Joeke Noordhuis, Willem-Pier Vellinga, Marc Verwerft en Xiao Bo Zhou. Sinds die tijd zijn er bij gekomen: Dimitri van Achterveld, Nuno Carvalho, Patricia Carvalho, Bas Groen, Hans Hegeman, Jaap Hooijmans, Arjen Kloosterman, Ferry van Looyengoed, Arjen Roos, Tiedo Tinga, Arjen Vreeling, Yanguo Wang, Liwen Zhang en Edzo Zoestbergen. Met al deze AIO's, OIO's, Doc's was en is het altijd goed samenwerken op het lab.

Van de bovenstaande personen wil ik met name Ferry van Looyengoed bedanken voor het produceren van de nano-ceramische lagen tijdens zijn ontwerpersopleiding op het CFT, Philips.

Ook vele studenten hebben op hun eigen manier een bijdrage geleverd aan dit proefschrift, waarvoor dank verschuldigd is: Arnout van der Borden, Bjorn Cordia, Henk Haarsma, Marc-Jan de Haas, Jan Kinds, Gerbrand Krol Anke Sinnema, Tiedo Tinga en Raymond Willems.

De hoogleraren Boerma, Hibma en van Veen wil ik bedanken voor het doornemen van het concept proefschrift.

Maar ook wil ik natuurlijk mijn familie en vrienden bedanken voor hun steun tijdens en hun belangstelling voor mijn promotieonderzoek. Speciaal mijn ouders, wiens stimulering en ondersteuning op mijn lange studiepad onontbeerlijk is gebleken. En, lieve Tsjally, zonder jou waren de afgelopen jaren toch moeilijk voor mij geweest. Ik wil je bedanken voor alle steun en motivering die jij voor mij kan opbrengen. Dat nieuwe perioden in mijn leven meer tijd voor een ieder van jullie moge brengen!